Vehicle Dynamic Modelling and Parameter Identification for an Autonomous Vehicle

by

Matthew Van Gennip

A thesis

presented to the University of Waterloo

in fulfillment of the

thesis requirement for the degree of

Master of Applied Science

In

Systems Design Engineering

Waterloo, ON, Canada, 2018

Author’s Declaration

I hereby declare that I am the sole author of this thesis. This is a true copy of the thesis, including any required final revisions, as accepted by my examiners.

I understand that my thesis may be made electronically available to the public.

Abstract

For autonomous vehicles to be feasible, a fast and accurate model of the vehicle dynamics is required due to the complexity of the task. There are many different aspects to a driverless vehicle, including path planning, image processing, data analysis, and the low level control of the vehicle. All these processes are important; they need to work in tandem for the vehicle to be able to drive itself. Regardless of how good all the components are, the vehicle itself must be able to follow the desired trajectory. This is accomplished through the low level control of the vehicle, by using an accurate vehicle dynamic model to assess the safety and feasibility of a given trajectory. This thesis develops a 14 degree of freedom full car model of a 2015 Lincoln MKZ hybrid vehicle. A vehicle measurement system is attached to the vehicle in order to measure the suspension displacement along with the tire orientation, velocities, forces, and moments. In addition, a GPS and an inertial measurement unit is used to measure the position, acceleration, and angular velocities of the chassis. The vehicle is then tested on a dedicated test track in order to identify the vehicle parameters. The center of mass, wheel and vehicle inertias, coefficient of drag, and suspension parameters are identified. In addition, combined slip Pacejka tire models are developed. These parameters are identified using a two-step process. Parameters are first identified using simple physics based models. The second step uses the full vehicle dynamic model to further optimize the parameters, accounting for the numerous simplifications assumed in the simple physics based models. The vehicle dynamic model is implemented and validated in MapleSim 2017.3. The model is intended to be used for controller development and autonomous vehicle testing in a simulation environment.

Acknowledgements

The author would like to thank Maplesoft, the Natural Sciences and Engineering Research Council of Canada, the Canada Research Chairs Program, and the Ontario Centres of Excellence for funding this research.

Table of Contents

List of Figures

List of Tables

List of Abbreviations

ABS ----------Antilock Brake System

CAN----------Controller Area Network

CM----------Center of Mass

DEK ----------Double Equivalent Kinematic

ESC----------Electronic Stability Control

GPS ----------Global Positioning System

IMU----------Inertia Measurement Unit

LGS ----------Laser Ground Sensor

LIDAR----------Light Detection and Ranging

Moose ----------Nickname for the test vehicle, a 2015 Hybrid Electric Lincoln MKZ

MPC ----------Model Predictive Control

SAE ----------Society of Automotive Engineers

SEK----------Single Equivalent Kinematic

TCS----------Traction Control System

VMS ----------Vehicle Measurement Sensor

WFS ----------Wheel Force Sensor

WPS ----------Wheel Position Sensor

List of Symbols

g----------Gravity

m----------Mass

$\vec{v}$----------Velocity

$\vec{a}$----------Acceleration

I----------Inertia

M----------Moment

$\vec{F}$ ----------Force

$\vec{\tau}$----------Torque

$\vec{\omega}$----------Angular speed

$\dot{\vec{\omega}}$----------Angular acceleration

μ_R ----------Coefficient of rolling resistance

P----------Density of air

C_d----------Coefficient of drag

A_f----------Frontal area

l0----------Un-sprung length of suspension

k----------Spring constant

c----------Damping coefficient

R_{Tire} ----------Tire radius

s----------Longitudinal slip

α----------Wheel sideslip

C_x----------Longitudinal stiffness of the wheel

C_Y----------Cornering stiffness of the wheel

B, C, D, E---------Pacejka tire model parameters

μ_x----------Coefficient of friction in the longitudinal direction

μ_y----------Coefficient of friction in the lateral direction

Q_1, Q_2, Q_3--------Overturning moment parameters

γ----------Camber angle

$X_{WheelBase}$ ---------Distance from the front axle to the rear axle

$X_{WheelTrack}$---------Distance from the center of the left wheel to the center of the right wheel

X_{CM} ----------Distance from the front axle to the center of mass

Y_{CM} ----------Distance from the centerline of the left wheel to the center of mass

H_{CM} ----------Distance from the ground to the center of mass

W_{Rear}----------Weight measured by the WFS on the two rear wheels

W_{Front} ----------Weight measured by the WFS on the two front wheels

W_{Right} ----------Weight measured by the WFS on the two right wheels

W_{Left} ----------Weight measured by the WFS on the two left wheels

W_{CM}----------Weight measured by the WFS on all four wheels

1. Introduction and Literature Review

1.1. Introduction

Autonomous vehicles are getting much attention these days.[1, 2, 3, 4] There are many different parts of a driverless vehicle, including path planning [1], image processing [2-4], data analysis, and the low level control of the vehicle [5]. All these processes are important; they need to work in tandem for the vehicle to be able to drive itself. Regardless of how good all the components are, the vehicle itself must be able to follow the desired trajectory. This can be accomplished by using an accurate vehicle dynamic model to assess the safety and feasibility of a given trajectory [6].

An accurate vehicle dynamic model has many different benefits when developing an autonomous vehicle [7-8]. One benefit, as stated above, is that it could be used to determine whether a trajectory is feasible or not. Another benefit is that it can be reduced and used as a control oriented model. Yet another benefit is the ability to incorporate the full model into a simulation environment in order to accurately test how the vehicle will react under many different circumstances. This is easier and much safer than having to test the vehicle on real roads.

There is an ongoing project at the University of Waterloo that is working to convert a 2015 Hybrid Electric Lincoln MKZ (nicknamed the Autonomoose, or Moose for short) into a fully autonomous vehicle. One subsection of this project is dedicated to creating a high-fidelity model of the Moose that can be used for testing in a simulation environment. This thesis covers the vehicle dynamic modeling and parameter identification necessary for this project.

---

[1] Metro Magazine, ”NAVYA, Keolis to operate autonomous shuttle on public roads”. August 13, 2018. http://www.metro-magazine.com/technology/news/730846/navya-keolis-to-operate-autonomous-shuttle-on-public-roads

[2] Hetzner, Christiaan, “Germany seeks to create self-driving infrastructure”. August 10, 2018. http://www.autonews.com/article/20180810/COPY01/308109968/germany-seeks-to-create-self-driving-infrastructure

[3] Banerjee, A., Lienert, P., Shepardson, D., “Ford follows GM’s Cruise move with self-driving spinoff”. July 24, 2018. https://www.reuters.com/article/us-ford-motor-autonomous/ford-follows-gms-cruise-move-with-self-driving-spinoff-idUSKBN1KE24P

[4] Aptiv PLC, “Aptiv Launches Fleet of Autonomous Vehicles on the Lyft Network”. May 02, 2018. https://www.prnewswire.com/news-releases/aptiv-launches-fleet-of-autonomous-vehicles-on-the-lyft-network-300640756.html

1.2. Thesis Organization

This thesis details the testing, modelling, and parameter identification of a full 14 degree of freedom vehicle dynamic model for use in simulation, testing, and controller development. The first chapter consists of an overview and literature review of the parameter identification methods and current state of the art. The second chapter details the measurement devices used for data collection along with a detailed description of the different tests that were performed. The third chapter describes the structure of the model and the parameter identification performed. The fourth chapter presents the validation results for the full model under longitudinal, lateral, and combined scenarios. Lastly, the thesis concludes with several observations and suggestions for future work.

1.3. Literature Review

1.3.1. Parameter Identification

To create a realistic vehicle dynamic model, many important vehicle parameters must be identified. The accuracy of these parameters affects the accuracy of the model. Based on the intended fidelity of the model, many parameters can be ignored. For instance, a single-track model ignores all pitching and rolling effects, including all suspension parameters, corresponding inertia parameters, and the center of gravity locations associated with these effects. This simplifies the complexity of the model greatly; however it also limits the uses of the model due to the simplicity.

For the 14 degree of freedom model developed in this thesis, there are many parameters to identify. There is the center of mass location, the inertia of the vehicle and the tires, the coefficient of drag, all the suspension parameters, and all necessary tire parameters. Due to the complexity of the tire model parameters, these will be discussed in Section 1.3.2.

To estimate parameters for a high fidelity model, it is often easier to investigate how the parameters would be identified for lower fidelity models. For instance, when looking at the inertial parameters of the vehicle, if a high fidelity model is used then any error in other identified parameters can lead to errors in the inertial parameters. Consequentially, many parameters are derived from first principles or simplified models that isolate the desired parameters. By using this method, many simplifications can be assumed. This leads to parameters that are slightly erroneous due to the simplifications. To account for this inaccuracy, after all parameters are identified they are implemented in the full vehicle dynamic model where further optimization can occur. This optimization will tweak the parameters, correcting the earlier simplifications.

The center of mass (CM) is a point representing the mean position of matter in the vehicle. The CM of a vehicle can be found in many ways [9-11]. Generally the CM is found statically on a fixed test platform. This method is simple and reliable, using first principles, namely moment balance equations, to determine the horizontal CM location by recording the weight on each wheel. The height of the CM can be found using the same principles; however in order to do this the vehicle must be tilted or rolled so that the vehicle is no longer horizontal. Generally this value is found by using a dynamic test platform which can rotate the vehicle slowly. It can also be found during a dynamic maneuver involving vehicle pitching

maneuvers. Lacking the equipment to perform this test, the vehicle can be statically placed in a non-horizontal orientation in order to determine the CM, although this method is less accurate due to limited experimental data – only having one data point as opposed to an array of data points that would be obtained using a dynamic test platform.

The inertia parameters represent the resistance of the vehicle to any change in velocity. These parameters can be found in many different ways [12]. One of the more accurate methods to determining the inertia of a vehicle is by using a dynamic test platform to perform a series of maneuvers that excite isolated rolling, pitching, and yawing motions of the vehicle [13-14]. By isolating the desired motion, a simple moment balance equation can be used. This sort of testing can accurately determine the principal moments of inertia. Additional testing can be completed in a similar manner to determine the products of inertia; however, due to the near symmetry of the vehicle these values are usually small and generally ignored [15].

Another method to determine the inertia of a vehicle is by performing dynamic maneuvers and measuring the angular velocities and accelerations along with the forces on the vehicle. This method is not as accurate due to the difficulty in isolating pitching, rolling, and yawing motions. In addition, the forces experienced by the vehicle are generally difficult to measure accurately. If the forces are measured accurately then a full set of moment balance equations can be used to identify the inertial parameters. Even though the measurement accuracy is reduced, by optimizing all parameters simultaneously a more accurate result may be achieved.

The drag force on a vehicle is a force that acts opposite to the relative motion between the air and the vehicle. It is common for automotive manufactures to design a streamlined vehicle that minimizes the drag force by minimizing the coefficient of drag for the vehicle. The coefficient of drag is easiest to identify in a wind tunnel due to the level of control available [16]. In a wind tunnel, the wind speed and direction is defined and controlled as an input. On a test track, the wind speed and direction are difficult to determine accurately. By measuring the forces experienced on the vehicle while measuring the speed of the wind relative to the chassis, the drag coefficient can be identified. This can also be done through on-road testing [18]; however as mentioned before, the relative speed between the wind and the chassis can be difficult to measure experimentally. Measuring the relative speed is normally accomplished by measuring the wind speed and heading using a weather way station, assuming there are no changes throughout the duration of the test, and then measuring the vehicle speed and heading. While this

method is simple to perform, there is a significant amount of error introduced by assuming the wind conditions remain constant throughout the entire maneuver.

Most suspension systems on vehicles consist of both a spring and a damper for each wheel. Normally the left and right wheels of a vehicle are identical, whereas the front and rear wheels are generally different. The Moose has a simple Macpherson strut on the front wheels and an independent multi-link design on the rear wheels. The Moose also has a semi-active suspension system, meaning that the damping coefficient changes as the vehicle moves.

The spring constant for the front and rear suspension systems must be identified. In addition, the damping control law must be found. One reliable method for identifying suspension parameters is through 4-post testing. This testing method involves placing the vehicle on four independent vertical posts that can be individually activated. Since all the four posts are individually actuated, they can be arrayed in specific configurations in order to perform different tests. For instance, a heave test involves all four posts being actuated at the same time. A roll test involves the two left posts and two right posts to be actuated with a phase shift of π. This causes the left posts to reach the positive amplitude at the same time that the right posts reach the negative amplitude which will cause the vehicle to exhibit a rolling behaviour. Likewise, a pitch test involves the two front posts and the two rear posts to be set out of phase. Throughout these tests the suspension parameters can be identified [17]. This can also be accomplished through normal road testing since the vehicle will encounter rolling, pitching, and heaving motions; however it is more difficult to identify the parameters this way due to the lack of control. Since the Moose has a semi-active suspension, road testing is required to determine the damping control law since the semi-active system is not active during 4-post testing.

1.3.2. Tire Modelling

Accurate tire-force models are vital components in vehicle modeling in order to analyze and simulate a vehicle trajectory [19]. These models dictate how much longitudinal and lateral force are available for each tire. Based on this information, the vehicle controller can determine what inputs are needed in order for the vehicle to follow a reference trajectory [20]. An important aspect of tire modeling is the effect of tire forces in both the longitudinal and lateral directions simultaneously. This is vital information since generally both forces will be required to follow the given trajectory, or to determine if the reference trajectory is even possible.

Tires are one of the most difficult parts of a vehicle to model accurately. Over the years, many different models have been developed that provide varying accuracy. These include linear tire models [21], physics-based models such as the Brush model [22], the flexible model [23], and the Dugoff model [24-25], black-box models [26-27], finite element based models [28-30], and data-driven empirical models [31]. For many situations the simplicity and ease of linear tire models is sufficient for the task; however, other tasks may require a more accurate model. For a complicated task, such as controlling the trajectory of an autonomous vehicle, more accurate models are vital to ensure the vehicle controller does the best possible job [32]. Normally these models are developed in dedicated test facilities that can run controlled tests on the vehicle tires. Unfortunately, these tests are expensive and time consuming while resulting in models that may not be accurate enough under real road conditions. One of the main limitations of testing in test rigs is that any data outside the measurement range can only be extrapolated as approximations. Another major limitation is that the rolling belts or drums may not be representative of real roads. As such, on-road measurements may lead to better practical results even though there is less control available during testing.

There are some downsides and limitations to developing tire models using on-road data alone. The main limitation is the ability to control the conditions of the tests. When performing tire tests on a rig, all the parameters and conditions of the test can be set and accurately reproduced. Unlike rig testing, road testing results will vary depending on many uncontrollable parameters such as pavement conditions, tire temperature, and wind conditions. Due to this, the repeatability of the tests can sometimes be an issue; however, this can be mitigated by measuring certain external variables such as the temperature, tire pressure, wind speed, and friction coefficient of the road. By measuring these values, their variability can be accounted for during data analysis. Details regarding test repeatability are discussed in Section 2.2.5.

Another limitation of on-road testing is the ability to measure specific data points. For instance, it is difficult to measure data with both a large positive longitudinal slip value along with a large sideslip value. In cases like this, it may be that the vehicle is unable to achieve these values due to mechanical limitations. In these situations it is acceptable to not have data since the vehicle will rarely encounter such a scenario. In other cases it may be difficult to cause the vehicle to perform the necessary maneuver in order to collect the desired data. These cases have been taken into consideration when developing the testing to be performed on the vehicle.

Tire modeling is primarily used for determining the longitudinal (tractive) and lateral forces exerted by a tire, specifically when the vehicle is in motion. The tractive force is mainly dependent on longitudinal slip. Longitudinal slip is defined as follows [33]:

$$s = \frac{(R_{Tire}\omega - v)}{v} \tag{1.1}$$

where s is the longitudinal slip, v is the velocity of the center of the tire, R_{Tire} is the effective tire radius, and ω is the angular spin of the wheel. The longitudinal slip is generally very small; however, even slight differences in longitudinal slip can have drastic effects on the tractive force.

It is also worth noting that as the normal load on the tire changes, the radius of the wheel will also change. This change is measured and accounted for using the Vehicle Measurement System. Specific details regarding the information available through the Vehicle Measurement System are outlined in Section 2.1.1.

The lateral force is mainly dependent on the sideslip angle of the tire. Sideslip is defined as the angle between the wheel heading and the tire velocity [33], shown in Figure 1.1. Just like longitudinal slip, this value is generally very small, normally less than four degrees; however, these small changes have drastic effects on the lateral force.

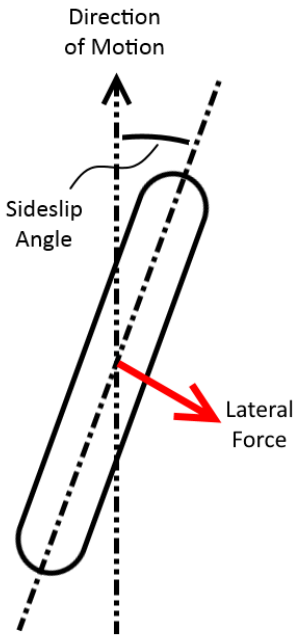

Figure 1.1: Sideslip angle definition

Both the longitudinal force and lateral force are also dependent on the normal load of the tire, which itself is dependent on many variables such as the static weight of the test test vehicle, the grade

of the road, the location of the center of gravity, along with any acceleration, pitch, and roll encountered by the vehicle. During an on-road maneuver, the normal load on each tire will vary. This constitutes one main benefit for testing on a dedicated test rig, since the normal load on the tire can be provided as an input. To account for the changing normal load during on-road testing, the longitudinal and lateral forces must be normalized. Details about this procedure can be found in the Section 3.2.5.

Both the longitudinal and lateral forces on the tire are developed through a generalized simplification of the tire patch dynamics. As the camber angle (the angle between the vertical axis of the tire and the axis orthogonal to the road surface) of the tire increases, the contact patch will deform, causing changes in the observed forces. The increase in camber angle will cause a camber thrust force [34], which generally adds to the observed lateral forces. Camber thrust can be taken to be directly proportional to the camber angle [35]. Details regarding how camber thrust is accounted for can be seen in Section 3.2.5.

There are other additional factors that affect the observed forces on the tire, such as the friction coefficient of the road, the tire temperature, and the tread wear. The tire tread will degrade over extended and extreme use. As the tread degrades, the available forces will decrease. This effect is not considered in this thesis since the application is for normal driving scenarios with tires in good condition. The temperature of the tire also impacts the longitudinal and lateral forces. Since the vehicle will be used for normal driving scenarios, the change in temperature is neglected since the corresponding change in forces is insignificant [36].

Lastly, the friction coefficient of the road determines how much force is available for the tires. This is due to the full Pacejka tire model being dependent upon the friction coefficient of the road as seen in Equations 1.4-1.5. Driving on dry pavement as opposed to ice is extremely different due to the difference in the friction coefficient. In this thesis, the friction coefficient is assumed to be constant. For simulation purposes this is acceptable since the friction coefficient is provided as an input; however, if these models are used on a vehicle controller, there will need to be an estimator in order to identify the friction coefficient. The parameter identification process outlined in Section 3.2.5 can be repeated with different road conditions in order to identify the change due to the friction coefficient.

A number of tire models have been developed for use with on-road measurement data as opposed to data gathered from a test rig. One of these models is the Thermal and Mechanical tire model [37-39]. This model is an accurate representation of a vehicle tire, potentially even more accurate than the Pacejka

tire model due to the inclusion of thermal properties. Consequentially, this model is useful for extreme driving situations, such as racing, whereas it is less important during normal driving scenarios, where the thermal properties of the tire do not vary greatly. Since the intended application is to be used for normal everyday driving, this model is not used since the added complexity of this model is not required.

A much simpler tire model is a linear tire model [21]. As the name suggests, this model varies linearly with longitudinal slip and sideslip angle. The formulas for this model are outlined in Equations 1.2 through 1.3.

$$F_x(s) = C_x s \tag{1.2}$$

$$F_y(\alpha) = C_y \alpha \tag{1.3}$$

where α is the sideslip of the wheel, C_x is a constant representing the longitudinal stiffness of the tire, and C_y is a constant representing the cornering stiffness of the tire. This model is useful since it is easy to implement due to the simplicity of the equations; however, it is only accurate for very low longitudinal slip and sideslip angle values. Normal driving situations may exceed these limits, causing the model to become inaccurate. As such, this model is not used in this thesis.

The Pacejka tire model is a more accurate representation of the tire forces. There are many different versions of the Pacejka model, the most recent version being in 2012 – PAC 2012 [31]. Each revision of the model adds more accuracy and complexity, adding properties to include combined slip conditions, advanced tire-transient behaviors, and other factors. To increase accuracy beyond the simple linear tire model, while also not increasing the complexity too much, the 1989 Pacejka tire model is used in this thesis. The formulas for the 1989 version of are outlined below in Equations 1.4 through 1.5. This model depends on both the longitudinal slip/sideslip angle and the normal force on the tire.

$$F_x(s, F_z) = D \sin\left(C \tan^{-1}\left(Bs - E(Bs - \tan^{-1}(Bs))\right)\right) F_z \, \mu_x \tag{1.4}$$

$$F_y(\alpha, F_z) = D \sin\left(C \tan^{-1}\left(B\alpha - E(B\alpha - \tan^{-1}(B\alpha))\right)\right) F_z \, \mu_y \tag{1.5}$$

where B, C, D, and E are all constants. These formulas are still a simple model compared with more recent versions of the Pacejka tire model. It is worth noting that these models work only under pure slip conditions, that is, when either a longitudinal force is being applied or a lateral force is being applied, not when both are applied simultaneously. To account for this condition, called combined slip, an updated Pacejka model, such as PAC 2012, could be used. This solution is not used in this thesis due to the large number of parameters involved, which detracts from the objective of creating a simple, accurate tire model. Instead, a piecewise combined slip model is used. This model captures the tire forces and moments

under combined slip scenarios, resulting in improved accuracy over the pure slip models while maintaining the relative simplicity of the 1989 Pacejka tire model. This method is described in Section 3.2.5.

Aside from the longitudinal and lateral forces there are also three moments acting on the tire. The tire axis used in this thesis is the Society of Automotive Engineers (SAE) tire axis system [33] shown in Figure 1.2. The moment about the X-axis is the overturning moment. The moment about the Y-axis is comprised of the applied wheel torque and the rolling resistance moment. The moment about the Z-axis is the self-aligning moment.

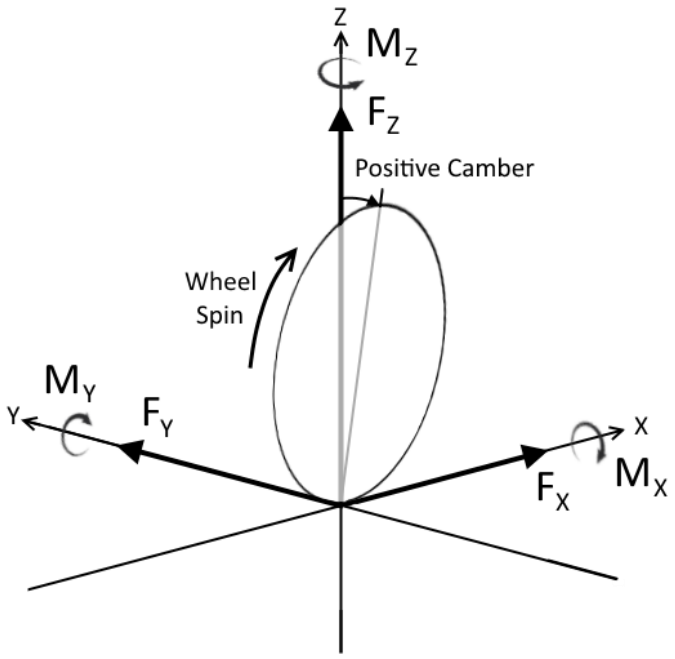

Figure 1.2: Society of Automotive Engineers (SAE) tire axis definition [33]

The overturning moment is dependent upon the lateral force and camber angle of the tire. As the camber angle increases, the tire's contact with the ground deviates from the centerline of the tire. This deviation, combined with the normal force on the tire, causes the overturning moment to occur. Similarly, lateral forces act upon the tire at the contact patch, causing an overturning moment at the center of the tire. An estimate of the overturning moment is outlined in Equation 1.6.

$$M_X = R_{Tire} F_Z \left(Q_1 - Q_2 \gamma + Q_3 \frac{F_Y}{F_Z} \right) \tag{1.6}$$

where Q_1, Q_2, and Q_3 are parameters to be identified and γ is the camber angle.

The moment about the Y-axis is primarily comprised of the torque delivered by the engine or motor through the powertrain. This value is an input to the system; however, in addition to the input torque there is also a resistive moment caused by the deformation of the tire. This deformation causes the distribution of the normal load through the contact patch to change, shifting the lumped normal force a distance of δx from the centerline of the tire. The rolling resistance moment is generally calculated by multiplying the lumped normal force by δx.

The self-aligning moment is found in a similar manner as the lateral force since it is mainly dependent upon the tire sideslip. When the tires are turned, the self-aligning moment acts to align the tire X-axis with the direction of motion. This moment is felt by the driver of the vehicle through the steering wheel; however autonomous vehicle systems will always define a specific steering angle. Since this angle is defined as an input to the system, the self-aligning moment will have very little effect on the dynamics of the vehicle, just applying another load on the steering motor, and can be ignored.

2. Data Collection and Experimental Testing

2.1. Data Acquisition System

2.1.1. Vehicle Measurement System

The Vehicle Measurement System, hereafter referred to as the VMS, is a system designed by A&D Technology [40] that attaches to a vehicle to measure a variety of signals while the vehicle is in motion. It is designed to capture data through on-road testing. The system is too large and expensive to be used constantly during normal driving. Instead the system is attached to the vehicle only during specific testing periods when the vehicle is taken to a dedicated test track or airport runway in order to perform the desired test maneuvers. The system consists of three main sensor arrays. The test vehicle with the VMS attached is shown in Figure 2.1.

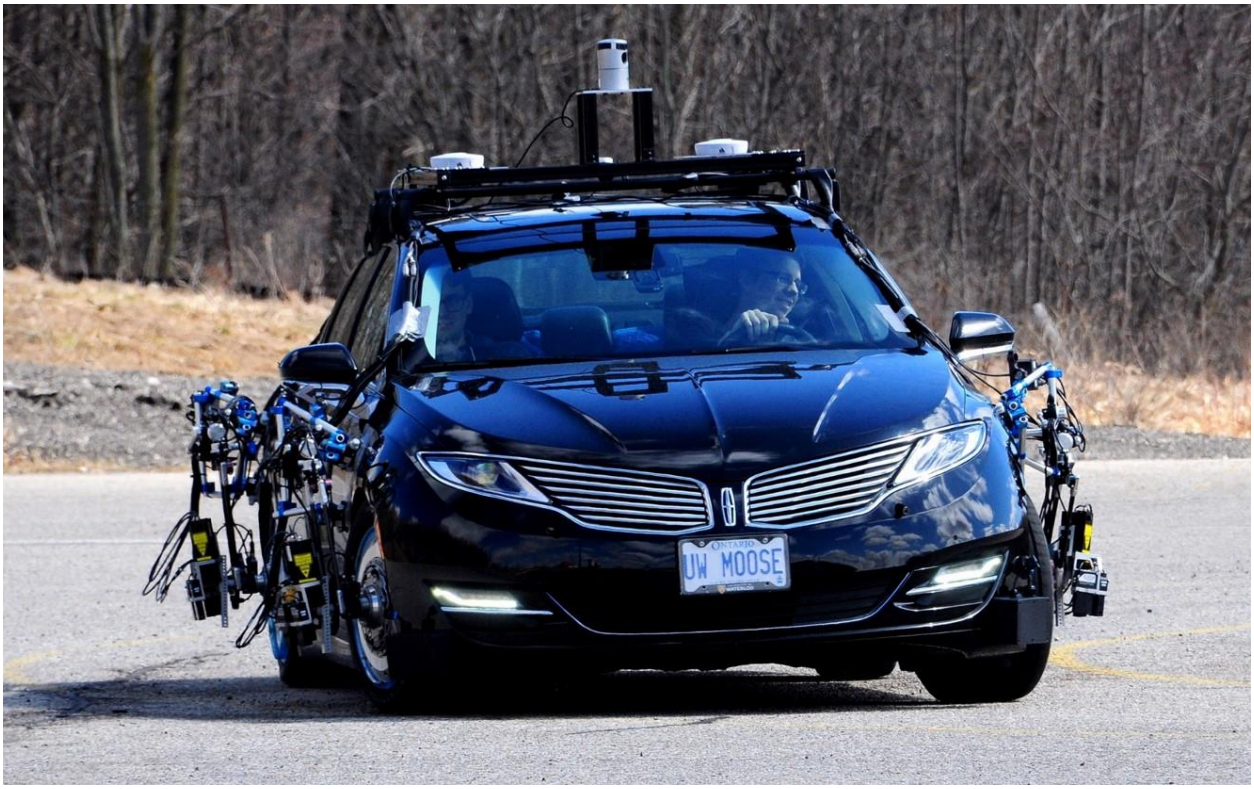

Figure 2.1: The Moose at the Waterloo Test Track with the VMS

The first sensor is the Wheel Force Sensor (WFS) shown in Figure 2.2. The WFS is a custom wheel hub that consists of an array of strain gauges that measure the forces and moments on the wheel. The data signals gathered from the WFS are:

- Longitudinal force
- Lateral force
- Vertical forces
- Moment about the longitudinal axis (as defined by SAE tire axis seen in Figure 1.2)
- Moment about the lateral axis (as defined by SAE tire axis)
- Moment about the vertical axis (as defined by SAE tire axis)
- Angular velocity of the wheel

Figure 2.2: Wheel Force Sensor (WFS) attached to custom wheel rim

The second sensor is the Wheel Position Sensor (WPS) shown in Figure 2.3. The WPS is a truss structure with five degrees of freedom that measures the position of the wheel relative to the chassis through the use of five separate encoders. One section of the truss system is attached to the center of the wheel hub. The other section is attached to an array of high quality suction cups that are attached to the vehicle chassis above the wheel. The data signals gathered from the WPS are:

- Longitudinal displacement of the wheel relative to the chassis
- Lateral displacement of the wheel relative to the chassis
- Vertical displacement of the wheel relative to the chassis
- Camber angle of the wheel
- Toe angle of the wheel

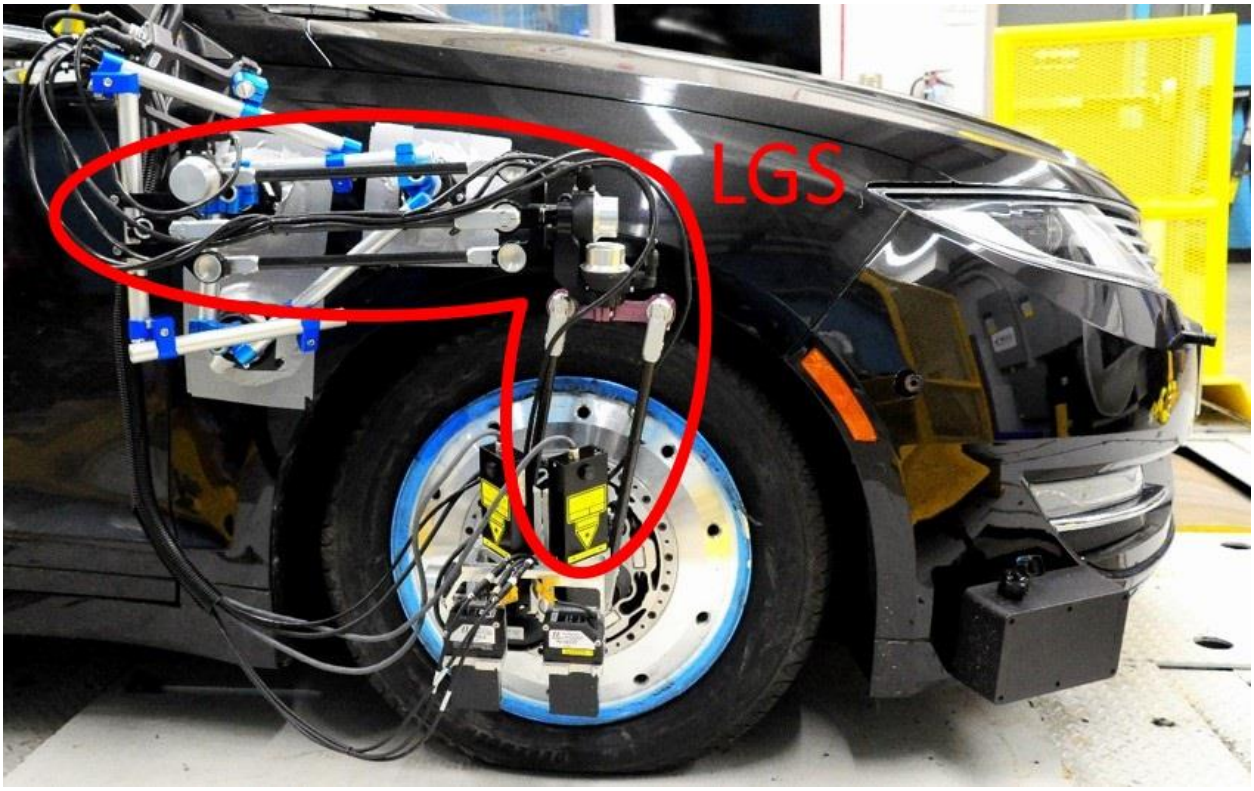

Figure 2.3: Wheel Position Sensor (WPS)

The last major sensor is the Laser Ground Senor (LGS) shown in Figure 2.4. This sensor array consists of five laser sensors. Three of these sensors measure the distance from the center of the wheel hub to the ground. These sensors are also used to account for any changes in tire orientation. This can include any orientation offset due to installation error. The other two sensors measure the longitudinal and lateral speed of the vehicle. The data signals gathered from the LGS are:

- Longitudinal speed of the vehicle at the tire
- Lateral speed of the vehicle at the tire
- Effective wheel radius
- Sideslip angle of the tire

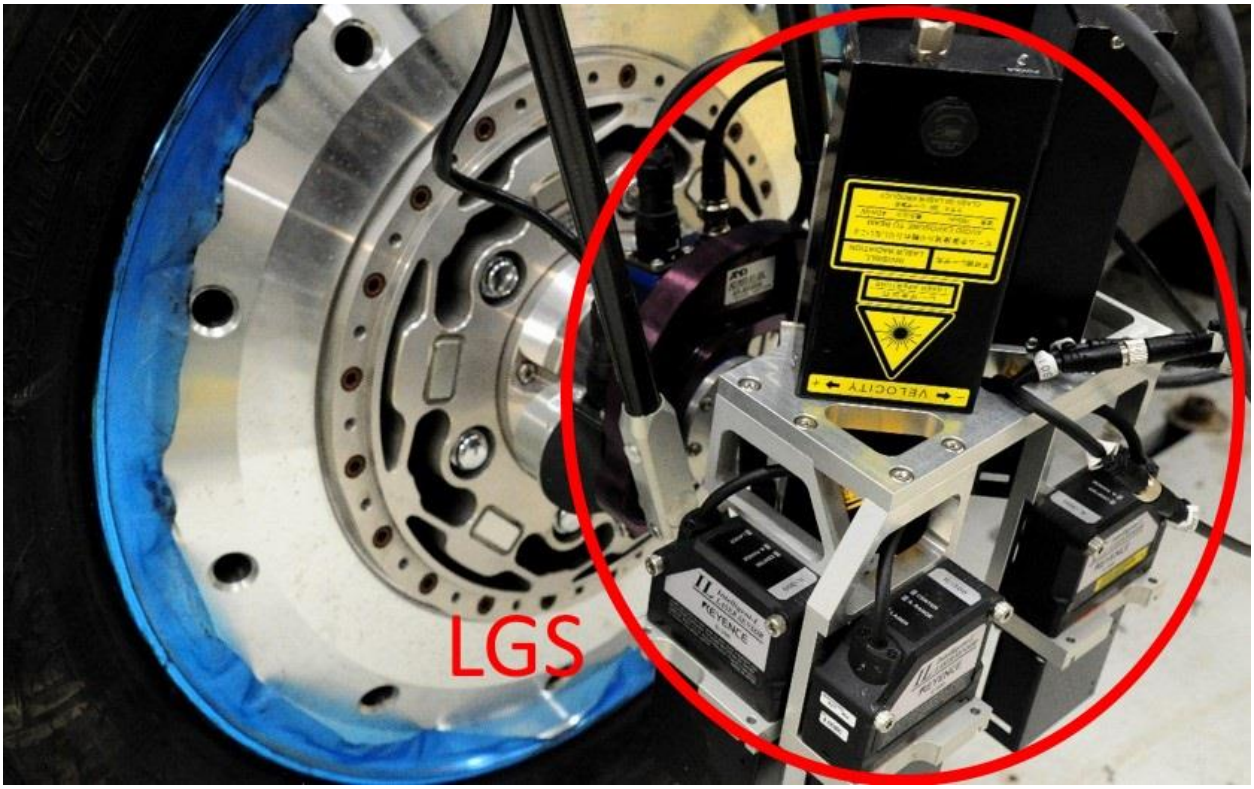

Figure 2.4: Laser Ground Sensor (LGS)

2.1.2. VBOX 3i

The VBOX 3i by Racelogic [41] is an Inertia Measurement Unit (IMU) coupled with a Global Positioning System (GPS). The unit is attached to the roof of the vehicle in a known position. The IMU captures the longitudinal, lateral, and vertical accelerations of the vehicle along with the roll rate, pitch rate, and yaw rate of the chassis. The GPS captures the location and heading of the vehicle. Coordinate transformations are necessary to transfer measured values from the sensor location to the center of mass of the vehicle.

2.1.3. Vehicle CAN and Vehicle Control Module

Many of the internal vehicle signals are communicated through the vehicle Controller Area Network (CAN). Most of these signals are not important for vehicle dynamic modeling and parameter identification; however, among these signals are the three main inputs to an autonomous vehicle: the steer angle, the accelerator pedal position, and the brake pedal position. These values were recorded during each maneuver in order to provide them as the input to the full vehicle dynamic model described in Chapter 3.

2.2. Experimental Testing

Many different tests need to be performed in order to get a comprehensive data set for parameter identification. A few parameters can be developed using longitudinal tests alone, but others require lateral motion as well. This section provides an overview of the different tests that were designed and performed to gather a comprehensive data set for each parameter identified in Chapter 3.

2.2.1. Center of Mass Tests

Two different tests can be done to determine the center of mass of the vehicle. The longitudinal and lateral center of mass locations can be easily identified while the vehicle is static. The height of the center of mass can be found using either of the two following tests.

The first test is a static test; no vehicle motion is necessary. To perform this test, the vehicle needs to be placed on a flat surface, and the front wheels need to be lifted off the ground. The front wheels should be placed on a post with a surface that is parallel to the ground. This causes the vehicle to be inclined at a set angle. This is an easy test to perform; however, it can take a long time to set up properly unless a specific test rig is used. In addition, the results may not be accurate if the vehicle angle (θ) is too small. To get accurate data, the vehicle angle should be around 45 degrees; however, this is generally not possible since it will likely cause the rear end of the vehicle to hit the ground. A picture of the test setup is shown in Figure 2.5.

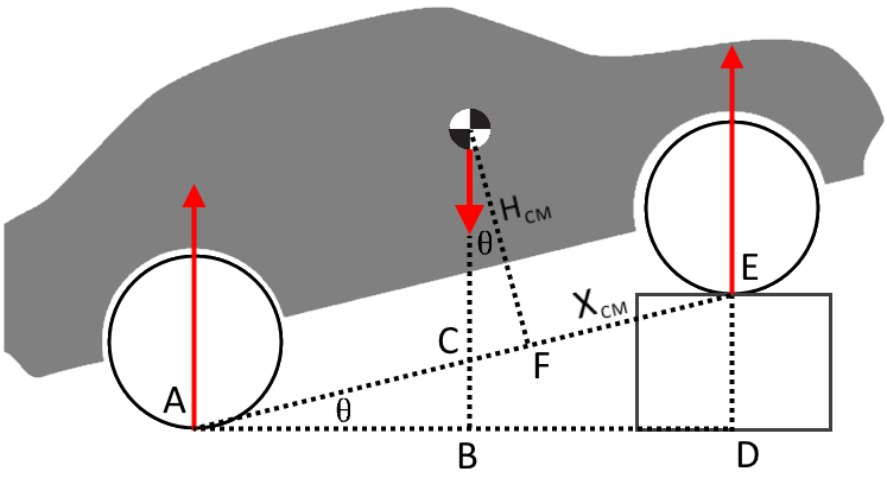

Figure 2.5: Experimental setup for static test to determine the height of the center of mass

Point A is at the contact point between the ground and the rear tire. Likewise, point E is the contact point between the front tire and the raised section of ground. The distance AE is the wheelbase of the vehicle and the distance DE is the known height that the vehicle was raised above the ground. The weight at the center of mass is the total weight of the vehicle, calculated by adding all the WFS measurements together.

The second test that can be completed is a dynamic maneuver. Any maneuver can be used for this test, so a simple longitudinal test is chosen. A rapid acceleration and braking maneuver is suitable to determine this parameter. Many different tests were performed with varying degrees of acceleration and deceleration. In the end it was found that minimizing the rate of change of acceleration provided the best test data. This is accomplished by performing a test with a single long acceleration event followed by a large braking event. The vehicle is brought from rest up to a speed of around 100km/h. Once this speed is reached, the brakes are applied so as to bring the vehicle back to rest. During the deceleration portion of the test the brake pedal should be kept at a constant position in order to minimize the change in acceleration of the vehicle. The height of the center of mass is found by solving the moment balance equation. The forces on each tire are measured using the WFS, and the angular speed of the chassis is measured using the IMU. The braking region will provide the best test data to use for the parameter identification due to the relatively constant longitudinal force. Figure 2.6 shows the velocity profile of this maneuver.

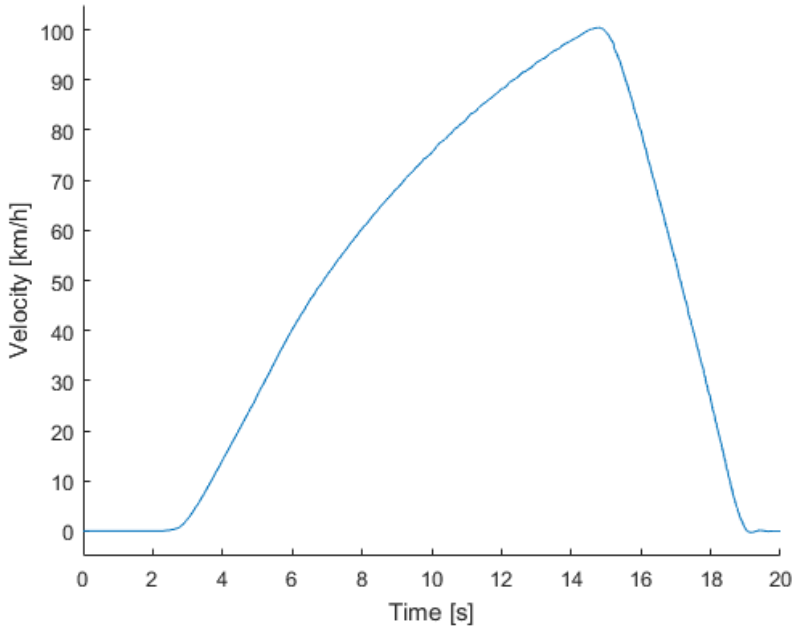

Figure 2.6: Velocity versus time for the center of mass dynamic maneuver

2.2.2. Inertia Tests

2.2.2.1. Wheel Inertia Tests

One test is needed to identify the wheel inertia. The vehicle's driven wheels, the front two wheels, were lifted off the ground so that they were allowed to roll freely. Once the driven wheels are able to rotate freely, the vehicle is turned on and an applied driving torque is sent to the wheels, which causes them to spin. The wheel inertia is found by solving the moment balance equation, requiring torque and angular acceleration. Both the torque and the angular speed of the wheel are recorded using the WFS. Shown in Figure 2.7 is the experimentally recorded wheel speed and wheel torque data versus time for a vehicle driven test.

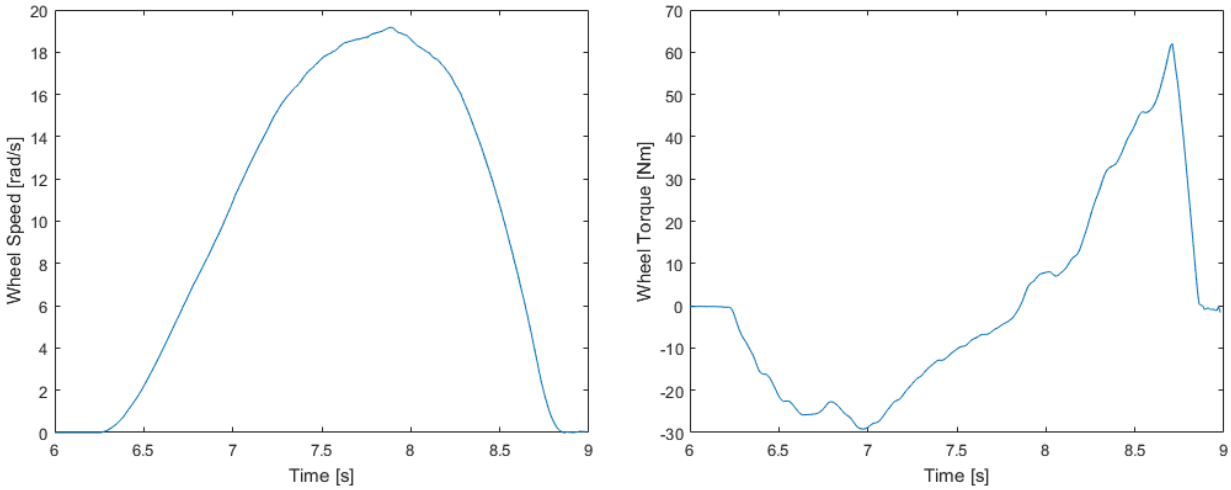

Figure 2.7: Wheel speed/torque versus time

2.2.2.2. Vehicle Inertia Tests

There are four main tests that were performed in order to identify the principal moments of inertia for the vehicle. One maneuver is a simple longitudinal maneuver. The other three are lateral maneuvers. The tests have been designed to solve the moment balance equation of the vehicle. Each test was designed to isolate pitch, roll, and yaw. Due to motion coupling this is not entirely possible; however, it is possible to minimize the non-desirable angular velocities while maximizing the desired angular velocity. This produces test data that is biased towards the associated inertial parameter. By combining the data from all these maneuvers, the principal moments of inertia can be identified more accurately.

The longitudinal maneuver is used to identify the pitch inertia. This maneuver is actually not required since the pitch inertia can also be identified during the lateral maneuvers; however, this test leads to better results for the pitch inertia. Similar to the dynamic maneuver seen in Figure 2.6, this maneuver is an acceleration and braking maneuver. Good results are observed when the pitch rate of the vehicle is large, which occurs during large acceleration values. Consequentially, the best way to perform the maneuver is to have a single large acceleration and braking event that causes the vehicle to pitch rapidly.

The roll and yaw inertias both affect the vehicle's lateral motion and therefore a lateral maneuver is required. Three different lateral maneuvers were developed in order to identify the yaw and roll inertia of the vehicle.

The first maneuver is a high-speed cornering test through a small angle. This maneuver is designed to cause a relatively low change in yaw angle while simultaneously causing a relatively high change in roll angle. This allows priority to be placed on roll inertia identification since the yaw and pitch effects are minimal. The second maneuver is a low-speed cornering test through a large angle. This maneuver causes a relatively low change in roll angle and a relatively high change in yaw angle. Speeds and steering angles for the above tests may vary. Multiple runs of this test were completed in order to minimize and maximize the desired rotational velocities, although this is not strictly necessary in order to identify the principal moments of inertia. The last maneuver is a basic sinusoidal steering maneuver where the steering wheel angle follows a sinusoidal curve that results in the vehicle swerving back and forth. In this test, the vehicle is put on cruise control in order to minimize the pitch of the vehicle. Large variations in yaw angle and roll angle are encountered in this maneuver, which can then be used to validate any results obtained from the previous two tests.

2.2.3. Coefficient of Drag and Rolling Resistance Tests

One test is needed to determine the coefficient of drag and the rolling resistance of the wheels; however, multiple runs of the test are required. The test is purely longitudinal and requires a large straight flat runway to allow the vehicle to coast down without introducing any lateral motion. As such it was performed at the Waterloo International Airport, seen in Figure 2.8.

Figure 2.8: Lincoln MKZ at Waterloo International Airport for drag testing

The vehicle is brought up to a speed of 130 km/h and then switched into neutral mode and allowed to coast down to a speed of 10 km/h. The vehicle is switched into neutral to avoid any regenerative braking effect, along with other potential resistive effects beyond the resistive forces caused by drag and rolling resistance, such as any powertrain inertial effects. Note that associated friction forces of the drive line up to the gearbox are lumped with the rolling resistance of the tires since it is not possible to isolate the wheels further without using a dedicated test rig.

Data was only used while the vehicle was in the neutral gear. Speeds higher than 120 km/h proved to provide more erroneous data points due to many of the simplifying assumptions that are described in Section 3.2.3. This test was performed both up and down the runway in order to minimize any effect of road slope, which would add an additional gravitational resistive force on the vehicle. The wind speed and direction were recorded using the weather station in the airport's control tower. Due to the sensitive nature of this test, especially with many rapidly changing variables such as wind speed and heading, multiple runs are needed in order to acquire a sufficiently rich data set.

2.2.4. Suspension Tests

Initially a 4-post test was performed to determine the vehicle parameters. As described in Section 1.3.1, 4-post testing involves placing the test vehicle on four individually actuated posts as seen in Figure 2.9. The vehicle should be in park to ensure that the vehicle will not roll off the posts during testing. Two accelerometers are placed above each post on both the sprung and unsprung mass (chassis and tires). The testing consists of a sinusoidal frequency sweep with a constant maximum velocity through all the frequencies. The test lasts for 30 seconds, starting at 1Hz, increasing to 10Hz at 15 seconds. Higher frequency data is ignored when identifying suspension parameters in order to minimize the effects of high frequency noise and other behaviours that are difficult to characterize. In addition, the natural frequency of a well-tuned vehicle suspension is generally under 10Hz [42].

Figure 2.9: Lincoln MKZ on 4-post test rig

As mentioned earlier, the Moose has a semi-active suspension system, meaning that the damping coefficient is not a constant value, but actually changes based on the motion of the vehicle. Since the semi-active suspension system is not active when the vehicle is at rest, a set of tests had to be devised in order to get similar data while the vehicle was in motion. Consequentially the following set of tests can be used in lieu of a 4-post-test rig. Note that the control logic for the semi-active system is not known, and as such many additional tests were performed in order to determine what parameters influenced the damping coefficient to change. Many of these tests turned out to be unnecessary due to the simplicity of

the control logic described in Section 3.2.4. Since they are not necessary they are not described in this thesis.

The first on-road test performed for determining suspension parameters was a simple longitudinal acceleration and braking maneuver. Unlike other acceleration and braking maneuvers that consist of a single acceleration and braking event, this maneuver consists of multiple smaller acceleration and braking events. These events should vary in length and magnitude. The goal is to cause the vehicle to pitch at different rates to determine if pitch rate has any effect on the semi-active control system.

The second on-road test performed for determining suspension parameters was a rapid swerving maneuver. Like the above test, the goal of this test is to cause the vehicle to roll. This test is similar to the final test performed in Section 2.2.2.2. The vehicle is brought up to a speed of 60, 80, and 100km/h and put on cruise control in order to minimize any longitudinal acceleration and pitch motion. The vehicle is then rapidly swerved from side to side. For each speed, two different tests are performed. One test involves quickly turning the steering wheel 30, 20, and 10 degrees (respectively for 60, 80, and 100km/h speeds) to either side. The other test involves turning the steering wheel 90, 60, and 30 degrees to either side at a much slower rate. The rates of change may need to be adjusted for different vehicles in order to get suitable amounts of roll and suspension travel.

Suspension travel is measured using the WPS. It is worth noting that most suspension systems do not travel in a straight vertical direction but at some angle. As the suspension compresses and decompresses there is also some change in camber angle, along with potential changes in longitudinal and lateral positions. To account for these additional changes in suspension travel, another test is needed.

The last test is a static test that is used for identifying the specific trajectory followed by the wheel center as the suspension system is compressed and decompressed. This is done by using the WPS to record the position of the wheel relative to the chassis while compressing and decompressing the suspension system in a controlled environment. This can be done through use of a simple car jack although better results are achieved when using a full vehicle lift. If using a vehicle lift, once the vehicle is fully raised off the ground, each individual wheel can be raised and lowered using a separate jack in order to measure the specific trajectory that the wheel travels when the suspension is compressed or decompressed. By following this procedure all dynamic effects are ignored and the kinematic motion of the center of the wheel is identified.

2.2.5. Tire Tests

Three different sets of maneuvers were developed for determining the Pacejka parameters for the vehicle's tires. One set of tests focuses on the pure longitudinal slip model. The next set focuses on the pure lateral slip model. The last set focuses on the combined slip model. For more details on the specifics of these models refer to Section 3.2.5. All testing was completed on dry pavement during warm summer months.

To get data for the pure longitudinal slip model, a rapid acceleration and braking test is performed. The vehicle is accelerated quickly from rest to a speed of around 100km/h, after which the brakes are applied, returning to rest as quickly as possible. A lower top speed can be used if necessary. The most important part of this test is the quick transients that will excite large longitudinal slip, filling in most of the nonlinear data regions. This single test is able to provide sufficient data for the pure longitudinal slip Pacejka model.

As opposed to the single test needed for the longitudinal model, three different tests are performed to obtain a sufficiently rich dataset for the pure lateral slip model. First, a steady state cornering test is performed. This test involves driving in a circle with a constant radius at a constant speed. This test is performed according to ISO standards [43] with a radius of 15m, 20m, and 25m. The second test is a double lane change maneuver. In this test, the vehicle travels at a constant speed through a typical double lane change motion. This test is also performed according to ISO standards [44-45] at speeds of 60km/h, 80km/h, and 100km/h. The last test is a step steer test. This test involves traveling in a straight line at a constant speed and then suddenly applying a large steer input. This is also done according to ISO standards [46] at speeds of 50km/h, 60km/h, and 70km/h with an approximate 120deg, 90deg, and 60deg steer angle input respectively.

It can be difficult to obtain data for pure longitudinal or pure lateral slip models using on-road data. This is simply because of the lack of control available during the road tests. For the above tests, the gathered data contains both pure slip and combined slip data points. For the pure longitudinal slip test it is relatively easy to ensure a small sideslip angle by keeping the steering wheel straight. Throughout this test there is a small constant sideslip angle caused from the toe angle, necessary for vehicle controllability; however any data points with larger sideslip values are ignored for the pure slip analysis. Likewise, for the pure lateral slip tests, any data points with large longitudinal slip are disregarded during the analysis.

Maintaining small longitudinal slip values throughout the lateral tests is more difficult, but with the large variety of tests performed, a comprehensive data set is gathered.

For the combined slip Pacejka model, two tests are used to obtain the necessary data. First, a modified step steer test is performed. The only difference from the above test procedure is that after the steering angle is applied, a large braking force is also applied. This results in data that has both a large longitudinal slip and a large side-slip angle. This test is only able to gather data for the negative longitudinal slip (braking) region since it is difficult to achieve large positive longitudinal slip during this maneuver unless the vehicle has a powerful engine.

The second test that is performed is the grand sweep maneuver. In this test, the steering wheel angle changes at a constant rate in either the clockwise or counter-clockwise direction according to the following criteria. The speed of the vehicle is not to exceed 70km/h and not to fall below 30km/h. While increasing the steer angle in either direction past the neutral straight wheel state (a steering angle of zero degrees) the brakes are to be applied. The braking should be applied so as to slow down the vehicle from the approximate speeds of 70km/h to 30km/h by the time the steering wheel angle rotates a full 360 degrees. After the vehicle slows down, the steer angle is moved back to the neutral straight wheel state at the same rate of change used previously. During this time the accelerator pedal should be applied. The acceleration should be applied so as to speed up the vehicle from the approximate speeds of 30km/h to 70km/h by the time the steering wheel angle returns to zero degrees – the neutral straight wheel state. Once the steering angle is back to zero degrees the wheel should continue to rotate in the same direction – so as to turn the vehicle in the other direction – with the above criteria in mind. This process is repeated a total of ten times. Ultimately this maneuver results in the vehicle traveling in a rough figure eight pattern as seen in Figure 2.10. Similar to the previous test, it is more difficult to excite large positive longitudinal slip than it is to excite large negative longitudinal slip; a powerful engine would be needed in order to excite this region.

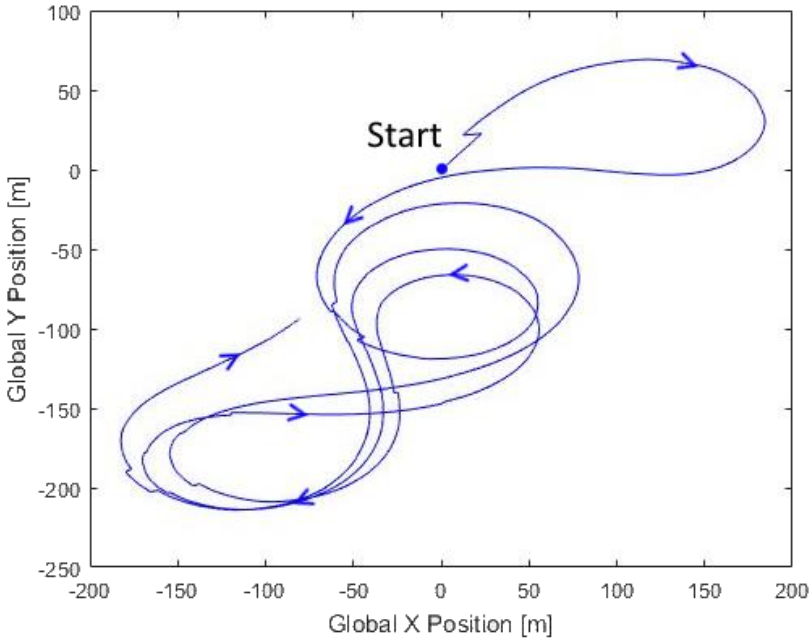

Figure 2.10: Sample vehicle trajectory of the grand sweep maneuver

Many different tests had to be altered and repeated to improve data quality and repeatability. All the tests detailed above are the final versions, easily repeatable with the exception of the grand sweep maneuver. All the pure lateral slip tests are according to ISO standards and the desired trajectories were outlined with low profile traffic pylons to ensure the tests adhered to the standards. The pure longitudinal test is simple and repeatable. The only test that is not easily repeatable is the grand sweep maneuver; however, since the test involves multiple runs it is easy enough to duplicate the gathered data even though the runs may be slightly different.

3. Vehicle Dynamic Modeling and Parameter Identification

3.1. Modelling

The vehicle that is modelled in this thesis is the Moose, a 2015 Hybrid Electric Lincoln MKZ. The vehicle has been turned into a drive-by-wire vehicle by AutonomouStuff [48]. This means that the steering wheel angle, accelerator pedal position, and brake pedal position can be changed through an electrical signal. Through this process the Antilock Brake System (ABS), Traction Control System (TCS), and Electronic Stability Control (ESC) were disabled. Throughout all the testing detailed in Section 2.2 these systems were never encountered. As such they are not considered when modelling the vehicle. There has been previous work using the VMS for vehicle parameter identification and modelling; however, it has been limited to longitudinal dynamics [49-50].

The vehicle is modelled using MapleSim 2017.3, a software developed by Maplesoft [51] for dynamic modeling and simulation. One advantage of this software is the use of symbolics and acausal modelling, which leads to faster computation times than conventional numeric software such as Matlab. The vehicle is modelled as a 14-degree of freedom rigid body model. The chassis is considered to be one rigid body with a full 6 degrees of freedom. Each tire has one degree of freedom allowing the wheel to spin. The front two wheels are also allowed to rotate about the vertical axis in order to model the steering of the vehicle; however these values are specified as an input steer value and therefore are not additional degrees of freedom. The last four degrees of freedom are modelled in the suspension system of the vehicle, allowing the suspension to compress and decompress.

The model has five inputs and forty-three outputs. A summary of the inputs and outputs is shown in Table 3.1. The outputs are the states of the vehicle and tires. Fifteen of these outputs are the states of the chassis. There are three outputs for each of the position, velocity, acceleration, orientation, rate of change of orientation of the chassis. There are seven outputs for the states of each wheel. There are three outputs for the position and orientation of each wheel, and another output for the rotational speed of each wheel. Since there are four wheels, there are a total of twenty-eight outputs for all wheels together.

It is worth noting that many of the outputs are not unique. Some of these values are simply outputted for convenience when using the model in a simulation environment. Many of the other values represent sensor readings that are captured for validation. These values can also be used in the simulation environment to mimic the values that would be captured from real life sensors.

The inputs to the model are the steering wheel angle and each of the four wheel torques. Another model has been developed by Bryce Hosking [52], which consists of the vehicle's powertrain and braking model. The powertrain model has two inputs and four outputs. The two inputs are the accelerator and brake pedal positions, and the four outputs are the four wheel torques. That model is designed to be used as a precursor to the model developed in this thesis, reducing the inputs to the steering wheel angle, accelerator pedal position, and brake pedal position. These are the inputs needed for an autonomous vehicle. For the development and validation of the vehicle dynamic model presented in this thesis, the powertrain model is not considered.

	Name	Description
Output (3)	Chassis Position	Global position of chassis (P_X, P_Y, P_Z)
Output (3)	Chassis Velocity	Local velocity of chassis (V_{LONG}, V_{LAT}, V_Z)
Output (3)	Chassis Acceleration	Local acceleration of chassis (A_{LONG}, A_{LAT}, A_Z)
Output (3)	Chassis Orientation	Global orientation of chassis ($Pitch, Roll, Yaw$)
Output (3)	Chassis Angular Velocity	Local angular velocity of chassis ($\dot{Pitch}, \dot{Roll}, \dot{Yaw}$)
Output (12)	Wheel Position	Local position of each wheel (P_{X_FL}, P_{Y_FL}, P_{Z_FL}, P_{X_FR}, P_{Y_FR}, P_{Z_FR}, P_{X_RL}, P_{Y_RL}, P_{Z_RL}, P_{X_RR}, P_{Y_RR}, P_{Z_RR})
Output (12)	Wheel Orientation	Local orientation of each wheel (θ_{FL}, ϕ_{FL}, β_{FL}, θ_{FR}, ϕ_{FR}, β_{FR}, θ_{RL}, ϕ_{RL}, β_{RL}, θ_{RR}, ϕ_{RR}, β_{RR})
Output (4)	Wheel Spin Rate	Spin rate of each wheel (ω_{FL}, ω_{FR}, ω_{RL}, ω_{RR})
Input (1)	Steering Wheel Angle	Angle of the steering wheel (δ)
Input (4)	Wheel Torque	Torque at each wheel (T_{FL}, T_{FR}, T_{RL}, T_{RR})

Table 3.1: Summary of the model inputs and outputs

3.2. Parameter Identification Using Simple Models

All parameters in this section are identified using simple models. This reduces the complexity of the system and allows the parameters to be identified easier; however, it also reduces the accuracy of the determined parameters. Once the rough approximation of all the parameters are identified, they are refined using the high-fidelity model as described in Section 3.3.

3.2.1. Center of Mass

The first parameter to identify for the model is the center of mass (CM) of the vehicle. The X location of the CM is defined as the distance from the front axle to the CM location. The Y location of the CM is defined as the distance from the centerline of the front left wheel of the car to the CM location. The height of the CM is defined as the distance from the ground to the CM. This can be seen below in Figure 3.1.

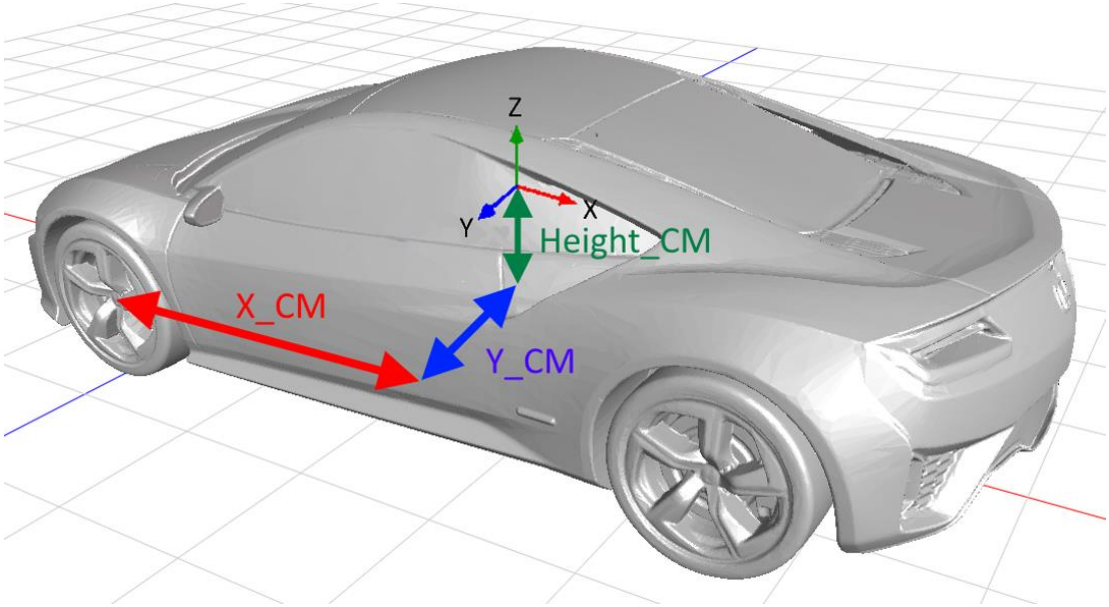

Figure 3.1: Defined location of the vehicle center of mass

Ensuring that the vehicle is at rest on flat ground, the static vertical forces through the WFS are captured. The vertical forces on the front two wheels are lumped into W_{Front}. Likewise, the rear wheels are lumped into W_{Rear}, the left wheels are lumped into W_{Left}, and the right wheels are lumped into W_{Right}. These forces are then used in moment balance equations to determine the values of the X and Y locations of the CM according to Equations 3.1-3.2.

$$\sum M_Y = 0 \tag{3.1}$$

$$-W_{Front}X_{from\ CM\ to\ front\ axle} + W_{Rear}X_{from\ CM\ to\ rear\ axle} = 0$$

$$-W_{Front}(X_{CM}) + W_{Rear}(X_{Wheel\ Base} - X_{CM}) = 0$$

$$X_{CM}(W_{Front} + W_{Rear}) = W_{Rear}X_{Wheel\ Base}$$

$$X_{CM} = \frac{W_{Rear}X_{Wheel\ Base}}{W_{Front} + W_{Rear}} = \mathbf{1.32\ m}$$

$$\sum M_X = 0 \tag{3.2}$$

$$-W_{Left}Y_{from\ CM\ to\ left\ side} + W_{Right}Y_{from\ CM\ to\ right\ side} = 0$$

$$-W_{Left}(Y_{CM}) + W_{Right}(X_{Wheel\ Track} - Y_{CM}) = 0$$

$$Y_{CM}(W_{Left} + W_{Right}) = W_{Right}X_{Wheel\ Track}$$

$$Y_{CM} = \frac{W_{Right}X_{Wheel\ Track}}{W_{Left} + W_{Right}} = \mathbf{0.791\ m}$$

For the remainder of this thesis let:

$$X_{from\ CM\ to\ front\ axle} = X_{CM} = X_f$$

$$X_{from\ CM\ to\ rear\ axle} = X_{Wheel\ Base} - X_{CM} = X_r$$

$$X_{from\ CM\ to\ left\ side} = Y_{CM} = Y_l$$

$$X_{from\ CM\ to\ right\ side} = X_{Wheel\ Track} - Y_{CM} = Y_r$$

X_{CM} is slightly closer to the front of the car than the rear since the engine and many other heavy components are located in the front of the vehicle. The CM for an unmodified stock vehicle was found to be 1.255m from the front axle. The identified value of 1.32m from the front axle is partially due to the added weight of the autonomous systems computer in the rear of the car. Y_{CM} is along the centerline of the vehicle which is standard practice in vehicle design. Consequentially these CM values seem reasonable.

To determine the height of the center of mass (H_{CM}) the vehicle will have to change orientation. One solution is to raise the front of the vehicle to cause the vehicle to be at a set angle from the ground. Similar to the previous two static tests, the forces on the wheels are measured using the WFS. Figure 3.2 is a duplicate of Figure 2.5, shown here for convenience. It shows the experimental setup of the vehicle for the static test. It is assumed that the displacements of the front and rear suspensions are equal. In

reality this is not the case; however the suspension displacement difference is small enough to cause the error to remain small.

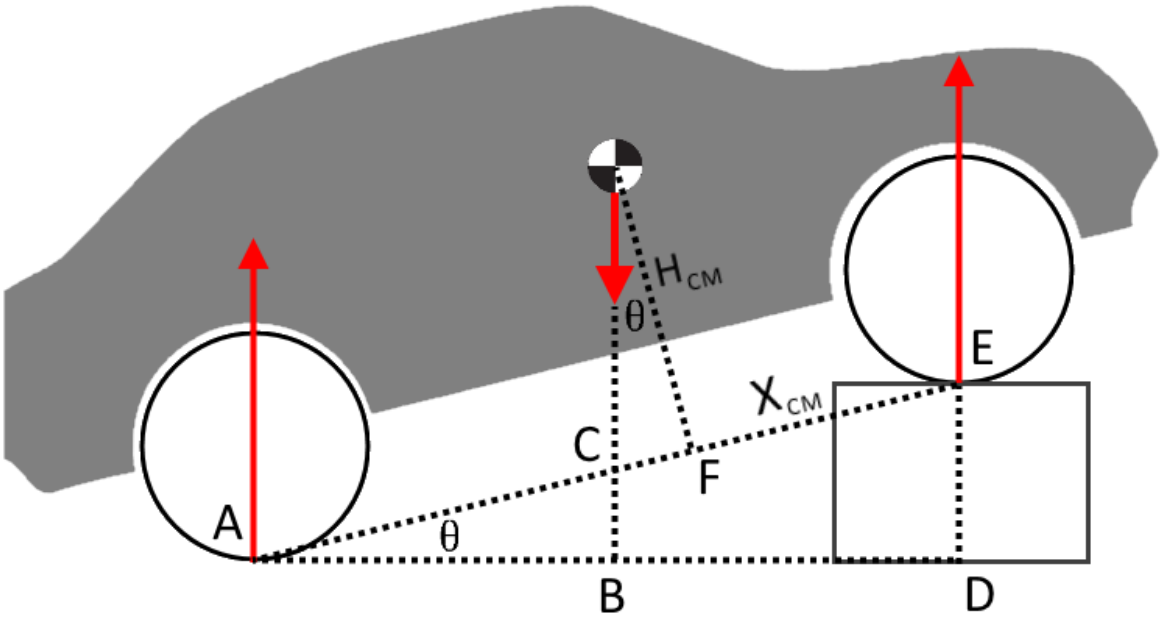

Figure 3.2: Experimental setup for static test to determine the height of the center of mass

Point A is at the contact point between the ground and the rear tire. Likewise point E is the contact point between the front tire and the raised section of ground. The distance AE is the wheelbase of the vehicle and the distance DE is the known height that the vehicle was raised above the ground. The weight at the center of mass is the total weight of the vehicle, calculated by adding all the WFS measurements together. The following equations show how to determine H_{CM} using this setup.

$$\theta = \sin^{-1}\left(\frac{DE}{AE}\right) \tag{3.3}$$

$$AD = AE\cos\theta \tag{3.4}$$

$$\sum M_A = 0 \tag{3.5}$$

$$W_{CM}AB - W_{Front}AD = 0$$

$$AB = \frac{W_{Front}AD}{W_{CM}}$$

$$AC = \frac{AB}{\cos\theta}$$

Using the above information, the small distance CF can be determined and used to find H_{CM}.

$$CF = AE - AC - X_{CM} \tag{3.6}$$

$$H_{CM} = \frac{CF}{\tan\theta} = \mathbf{0.534}\boldsymbol{m}$$

This value for H_{CM} seems reasonable based on known values of other similar vehicles [53]. To minimize error, the vehicle should be lifted to create an angle (θ) of around 45 degrees. This helps minimize the error due to the trigonometric functions; however, it can be more difficult to set up a test rig in this manner. Multiple tests can also be performed at different angles to reduce the error. This is similar to the tests performed on a dynamic test platform as outlined in Section 1.3.1.

In addition to the above tests, the vehicle was tested on a 4-post test rig as detailed in Section 2.2.4. The 4-post test rig can act like a dynamic test platform. By pitching and rolling the vehicle the center of mass can be identified. Shown below, in Table 3.2, is a comparison between the results from the 4-post testing software and the results calculated above using the VMS.

Center of Mass [m]	4-Post Testing	VMS Testing (Static)	% Error
X_{CM}	**1.27**	**1.32**	**3.8 %**
Y_{CM}	**0.759**	**0.791**	**4.0 %**
H_{CM}	**0.556**	**0.534**	**4.1 %**

Table 3.2: CM location comparison between 4-post testing and VMS testing

There are a few reasons for the small differences between the calculated CM from 4-post testing and the calculated CM from the static equilibrium model. First, there was a simulated driver weight during the 4-post testing; however, during the static equilibrium calculations there was both a simulated driver and a simulated passenger weight in the vehicle. This extra weight would increase the Y_{CM} of the vehicle. During the 4-post testing some of the equipment from the rear of the vehicle was also removed to be repaired and upgraded. This is the major reason for the differences seen in Table 3.2. It is common for the equipment on the vehicle to be added, removed, or moved around. Due to this fact, the above procedure is repeated at the beginning of each round of testing to identify the current CM location. The only exception is the test for determining the height of the center of mass. Instead of repeating the above static test, a dynamic test is performed since the inertia of the vehicle known (and reidentified for each maneuver) and the static test can be lengthy.

The dynamic test performed is outlined in Section 2.2.1. Both the accelerating and braking regions can be used to determine H_{CM}; however, the braking region generally has a more consistent acceleration, and consequentially this range of test data is used. The same moment balance equation used for X_{CM} and Y_{CM} cannot be used to determine H_{CM} since the vehicle is not at rest. The vehicle inertia is identified in Section 3.2.2.2 and is used here to calculate H_{CM} as shown in Equation 3.7. It is assumed that the transverse effects are small and therefore ignored. See Section 3.2.2.2 for more details.

$$\sum M_Y = I_Y \dot{\omega}_Y \tag{3.7}$$

$$W_{Rear}X_r - W_{Front}X_f - F_{Longitudinal}H_{CM} = I_Y \dot{\omega}_Y$$

This equation is used to solve for H_{CM}. Generally the braking region provides better results than the accelerating region due to a more constant longitudinal force. An example of the calculated H_{CM} versus time for the dynamic test outlined in Section 2.2.1 can be seen below in Figure 3.3. The results shown are from the most recent set of test data (June 2018). The optimal least square value during the duration of the braking region of the maneuver is used as the height of the center of mass. This value is shown as the constant line in Figure 3.3.

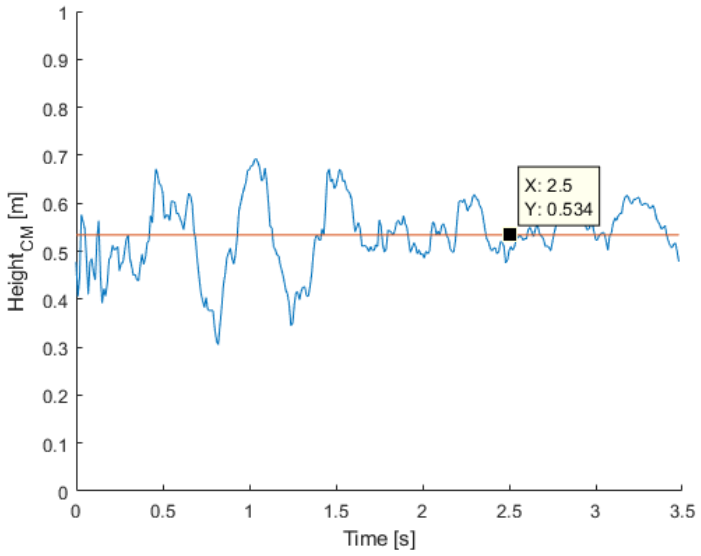

Figure 3.3: H_{CM} versus time for dynamic maneuver

From the same set of data, the X_{CM} and Y_{CM} have also been calculated. A comparison of CM locations by date is shown in Table 3.3. X_{CM} and Y_{CM} were calculated in the same method described, while H_{CM} was calculated using the dynamic test method instead of the static lift calculations.

Center of Mass [m]	VMS Testing (Static) April 2017	VMS Testing (Dynamic) August 2017	VMS Testing (Dynamic) June 2018
X_{CM}	**1.32**	**1.33**	**1.39**
Y_{CM}	**0.791**	**0.811**	**0.865**
H_{CM}	**0.534**	**0.531**	**0.566**

Table 3.3: Comparison of CM locations over time

It can be seen that the CM location changes from test to test. For the remainder of this thesis it is assumed that the CM values used are the values calculated for that set of testing. It should be noted that as equipment (such as LIDAR, cameras, computers, and supporting mechanical framework for the aforementioned equipment) has been added to the vehicle, the Y location of the center of mass has deviated from the center line of the vehicle. This can have negative effects on vehicle handling.

In the future it is assumed that no more major changes will be done on the vehicle. At that point it will be possible to recalculate the CM of the vehicle and assume it will remain constant for all further testing, both for modelling and any controller development.

3.2.2. Inertias

3.2.2.1. Wheel Inertia

The inertia of the wheels of the vehicle are important parameters to determine since they are a major factor in determining how much torque is required to cause a desired acceleration. To determine the principal moment inertia of the front two wheels, the test outlined in Section 2.2.2.1 was performed. The torque through the wheel was captured using the WFS. The WFS also captured the angular velocity of the wheel. The angular velocity was numerically differentiated once with respect to time to determine the angular acceleration of the wheel. These values were then used to solve the moment balance equation below.

$$\sum M_Y = I_{YY}\dot{\omega}_Y \tag{3.8}$$

$$\tau = I\dot{\omega}$$

$$I = \frac{\tau}{\dot{\omega}} = \mathbf{1.40\ kg\ m^2}$$

The average inertia throughout the set of tests was determined to be 1.40 kg m^2 as seen above. Figure 3.4 shows the inertia versus time for the front left wheel. The large spikes seen in Figure 3.4 are the moments when the vehicles brakes were applied. This caused large sudden changes in applied torque and angular acceleration which led to more erroneous data.

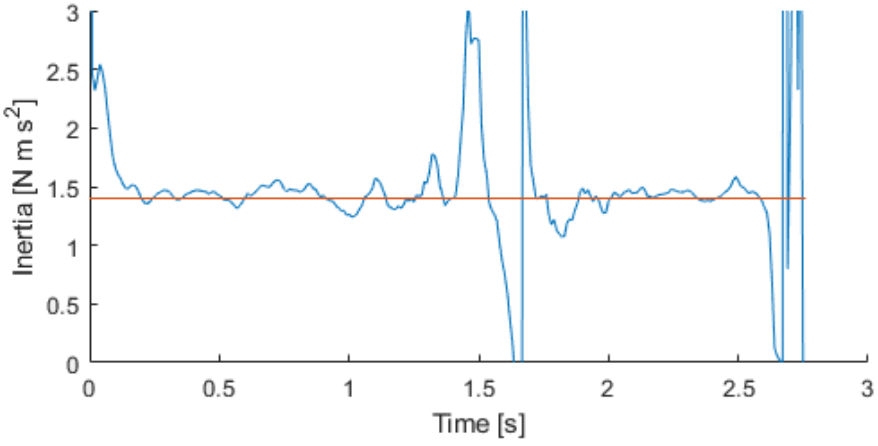

Figure 3.4: Wheel moment of inertia versus time

Similar results were found for the front right wheel. Therefore, it was assumed that all wheels, including both of the rear wheels, have the same principal moment of inertia.

3.2.2.2. Vehicle Inertia

The inertia of the vehicle is an important parameter to identify; however, as noted in Section 3.2.1, since the vehicle is modified constantly, the inertia parameters will change slightly between each testing session. Like the center of mass, the vehicle inertia must be identified at the beginning of each round of testing.

The pitch inertia is isolated since a maneuver can be performed on the vehicle that will excite very small amounts of roll and yaw angles. By keeping these angles small, they can be effectively ignored. A free body diagram of the vehicle is shown in Figure 3.5.

$$\sum M_Y = I_{YY}\dot{\omega}_Y \tag{3.9}$$

$$I_{YY} = \frac{W_{Rear}X_r - W_{Front}X_f - F_{Longitudinal}H_{CM}}{\dot{\omega}_Y} = \mathbf{3705\ kg\ m^2}$$

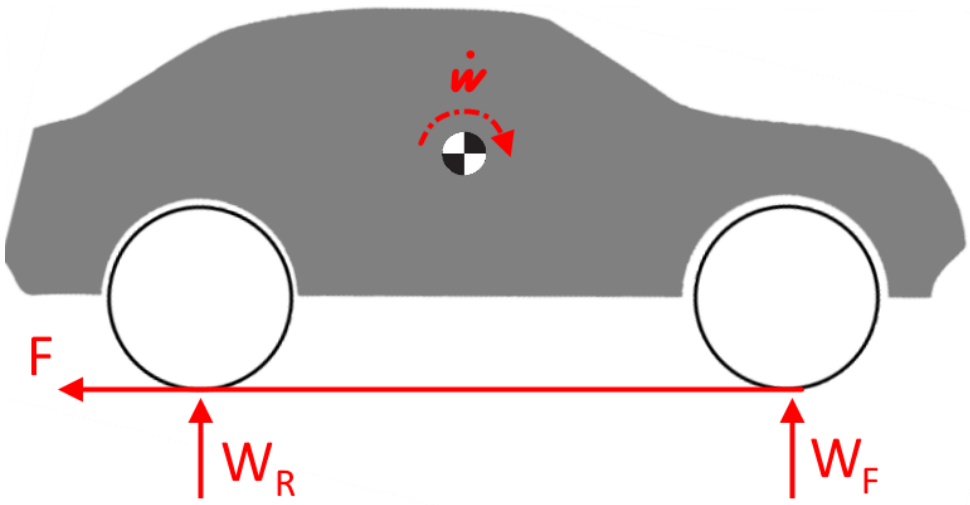

Figure 3.5: Free body diagram of the vehicle during a longitudinal maneuver

To determine the other moments of inertia of the vehicle, a full moment balance equation is needed. This is since both vehicle yaw and roll are related to the lateral movement of the vehicle, and as such they are difficult to isolate.

$$\sum M_X = I_{XX}\dot{\omega}_X - (I_{YY} - I_{ZZ})\omega_Y\omega_Z \tag{3.10}$$

$$\sum M_Z = I_{ZZ}\dot{\omega}_Z - (I_{XX} - I_{YY})\omega_X\omega_Y \tag{3.11}$$

Since small amounts of pitch are also encountered in this maneuver, the pitch inertia can be identified again and compared to the previous results

$$\sum M_Y = I_{YY}\dot{\omega}_Y - (I_{ZZ} - I_{XX})\omega_Z\omega_X \tag{3.12}$$

A non-linear least squares optimization routine was run in order to identify the three principal moments of inertia. The results are as follows:

$$I_{XX} = \mathbf{1786\ kg\ m^2}$$
$$I_{YY} = \mathbf{3712\ kg\ m^2}$$
$$I_{ZZ} = \mathbf{4197\ kg\ m^2}$$

For future testing sessions, Equations 3.10-3.12 are re-optimized to identify the updated moments of inertia for the vehicle. Generally the changes are minor.

During the above calculations all the products of inertia are ignored as they are relatively small. This is because the defined vehicle fixed axis is close to the principal direction due to the symmetry of the vehicle. The vehicle is not perfectly symmetrical, which causes some transverse effects to be seen. Equations 3.13-3.15 show the results including the products of inertia.

$$\sum M_X = I_{XX}\dot{\omega}_X - (I_{YY} - I_{ZZ})\omega_Y\omega_Z - I_{XY}(\dot{\omega}_Y - \omega_Z\omega_X) - I_{YZ}(\omega_Y^2 - \omega_Z^2) - I_{ZX}(\dot{\omega}_Z - \omega_X\omega_Y) \quad (3.13)$$

$$\sum M_Y = I_{YY}\dot{\omega}_Y - (I_{ZZ} - I_{XX})\omega_Z\omega_X - I_{YZ}(\dot{\omega}_Z - \omega_X\omega_Y) - I_{ZX}(\omega_Z^2 - \omega_X^2) - I_{XY}(\dot{\omega}_X - \omega_Y\omega_Z) \quad (3.14)$$

$$\sum M_Z = I_{ZZ}\dot{\omega}_Z - (I_{XX} - I_{YY})\omega_X\omega_Y - I_{ZX}(\dot{\omega}_X - \omega_Y\omega_Z) - I_{XY}(\omega_X^2 - \omega_Y^2) - I_{YZ}(\dot{\omega}_Y - \omega_Z\omega_X) \quad (3.15)$$

Another non-linear least squares optimization routing was run to identify all the inertial parameters. The results are as follows:

$$I_{XX} = \mathbf{1861\ kg\ m^2}$$
$$I_{YY} = \mathbf{3695\ kg\ m^2}$$
$$I_{ZZ} = \mathbf{4281\ kg\ m^2}$$

$$I_{XY} = \mathbf{24\ kg\ m^2}$$
$$I_{YZ} = \mathbf{36\ kg\ m^2}$$
$$I_{ZX} = \mathbf{112\ kg\ m^2}$$

As can be seen the products of Inertias – I_{XY}, I_{YZ}, I_{ZX} – are small and consequentially ignored in order to simplify the model and subsequent equations. If any product of inertia were to be included in the model then it would be I_{ZX}. This value is the largest of the three values and occurs due to the relationship that both the roll and yaw motions have with the lateral movement of the vehicle.

3.2.3. Coefficient of Drag and Rolling Resistance

The largest resistive forces acting on the vehicle are the drag force and rolling resistance force. The rolling resistance force calculated in this section is only used with the linear tire model. This is because the linear tire model used in this thesis does not account for the rolling resistance moment unlike the Pacejka tire model developed in Section 3.2.5. That section also identifies an updated rolling resistance moment for use in the Pacejka tire model. For the linear tire model, it is sufficient to simplify the rolling resistance coefficient by considering it as a constant value. In reality the rolling resistance is not constant; however, for speeds below 70km/h the change in rolling resistance is insignificant [18]. Equation 3.16 shows the equation used for calculating the drag force.

$$F_{Drag} = {}^{1}/_{2}\,\rho C_d A_F (V + V_w)^2 \tag{3.16}$$

where ρ is the density of air (1.2 kg/m^3), C_d is the aerodynamic drag coefficient (to be determined), A_F is the frontal area of the vehicle, V is the longitudinal speed of the CM, and V_w is the headwind speed.

The speed of the wind and the wind heading are provided by the weather station at the airport. These values can be used together to determine the headwind velocity. During testing there was no headwind, only a crosswind. As such, only the measured velocity of the CM was used in Equation 3.16.

An approximation of the frontal area of the vehicle is calculated by processing a picture of the front of the vehicle. Figure 3.6 is the image that was captured. This image was used to generate the binary image seen in Figure 3.7.

Figure 3.6: Front Profile of the Lincoln MKZ

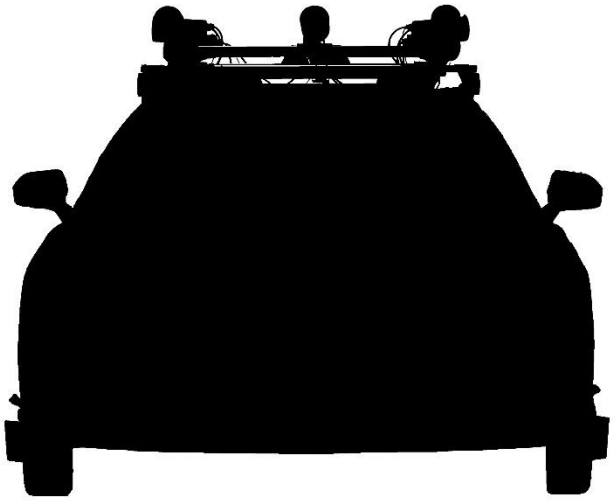

Figure 3.7: Frontal area of the Lincoln MKZ

Figure 3.7 is used to calculate the frontal area of the vehicle. This is accomplished by trimming the image so that the real life height and width of the picture is known. The width of the image is trimmed so that the edges of the image line up with the far edges of the side mirrors of the vehicle since the distance between the side mirrors is a known value. The height of the image is initially trimmed to line up with the bottom of the tires and the top of the roof of the vehicle since the height of the vehicle is also a known value. Unfortunately, due to all the equipment on top of the vehicle, the height of the full image is not known. To set the image height to a known value, the image is first trimmed down to the known height –

from the bottom of the tires to the roof of the car – and then the image height is multiplied by 1.5 to increase the height of the image by a known value.

It is worth noting that there are some slight differences between Figure 3.6 and Figure 3.7. Between the time when Figure 3.6 was taken and the time drag testing occurred there were some modifications done to the equipment on the roof of the vehicle. This can be seen by comparing Figure 3.6 with Figure 2.8. To adjust for this change some additional processing was completed. Even with the changes to the roof equipment, Figure 3.7 is still missing all the frontal area generated by the addition of the VMS. During future testing, the VMS will not be attached, so the frontal area shown Figure 3.7 in will be accurate.

Since the height and width of the image are known, the real world equivalent area can be determined easily by multiplying the width with the height as seen in Equation 3.17.

$$A = wh \tag{3.17}$$
$$A = (1.86\ m)(1.48\ m) = \mathbf{2.75}\boldsymbol{m^2}$$

Once the area of the image is determined, the frontal area can also be determined. Using one of the many artistic editing programs available, the number of pixels in the image is found. The black pixels represent the frontal area whereas the white pixels represent the lack of surface area. The number of black pixels versus white pixels is found and the ratio is then multiplied together with the calculated real life area to find the real life frontal area. This procedure can also be completed using a MATLAB script. Equation 3.18 shows the calculation of the final frontal area of the vehicle, where N is the total number of pixels, B is the total number of black pixels, and R is the ratio of black pixels.

$$R = \frac{B}{N} = 0.756 \tag{3.18}$$
$$A_F = A\,R = \mathbf{2.08}\boldsymbol{m^2}$$

Once the frontal area is known, the only unknown value in Equation 3.16 is the coefficient of drag; however, to solve for the drag force, a full force balance equation is needed. Since the vehicle is in neutral, there are only two more major resistive forces acting on the vehicle. The first of these resistive forces is the rolling resistance force. This force results from a resistive moment on each tire caused by the tire deformation and contact patch dynamics; however, a simplified force can be approximated using Equation 3.19. As stated before, this approximation is only used when linear tire models are used in the model.

$$F_{RR} = \mu_R mg \tag{3.19}$$

where μ_R is the coefficient of rolling resistance (to be determined), m is the mass of the vehicle, and g is the gravitational constant (assumed to be 9.81 $^{m}/_{s^2}$).

The other major resistive force is a gravitational force due to road slope. It is often assumed that the vehicle is driving on a flat road, causing the gravitational force to be zero; however, an autonomous vehicle must be able to drive on a variety of roads, including hills. The gravitational force can be determined by identifying the slope of the road according to Equation 3.20.

$$F_g = mg \sin\theta \tag{3.20}$$

where m is the mass of the vehicle, g is the gravitational constant, and θ is the slope of the road above the horizontal (for an uphill maneuver θ is positive and for a downhill maneuver θ is negative). If the gravitational force is ignored when optimizing for the coefficient of drag and the coefficient of rolling resistance, then the identified values will be erroneous. It was determined that the runway used for testing has a slope of ±0.7 degrees, causing a small gravitational force to be encountered.

The full force balance equation is shown in Equation 3.21, using the resistive forces discussed above.

$$\sum F = ma \tag{3.21}$$
$$F_{Drag} + F_{RR} + F_g = ma$$

The acceleration of the vehicle is measured using the VMS. The other resistive forces are determined using Equations 3.16, 3.19, and 3.20. The drag coefficient and the coefficient of rolling resistance are determined by using a nonlinear least squares optimization routine. Figure 3.8 shows the identified forces added together, along with the calculated resistive force.

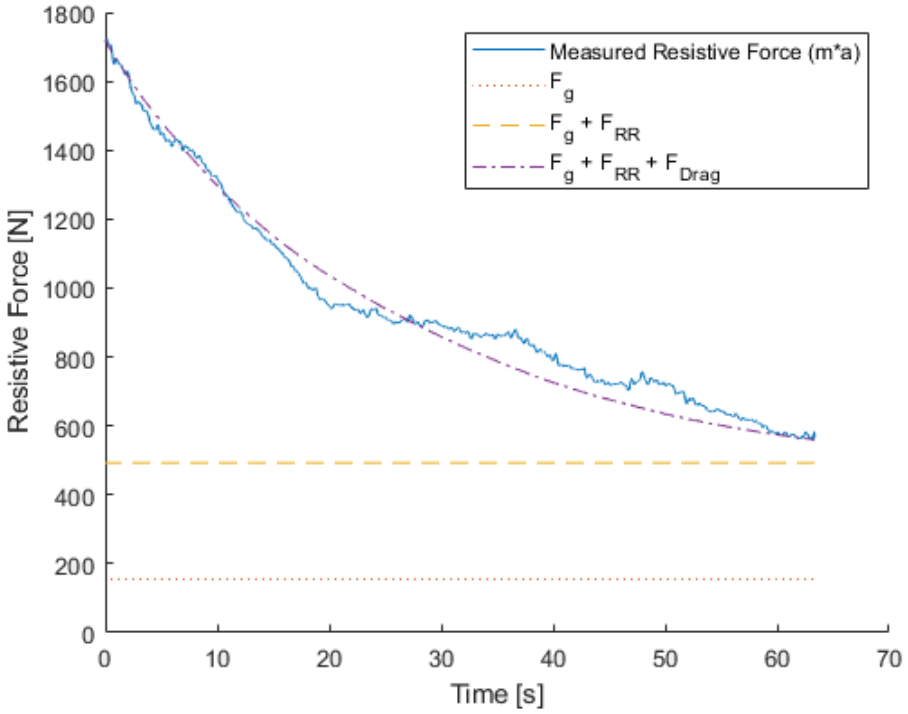

Figure 3.8: Resistive forces for uphill maneuver

In Figure 3.8, the bottom line shows only the effect of the gravitational force, the second line shows the effect of both the gravitational force and the rolling resistance force, and the top curve shows all three resistive forces added together. The sum of resistive forces closely matches the measured resistive force. The results of the optimization lead to the identification of the coefficient of drag and the coefficient of rolling resistance listed below.

$$C_d = \mathbf{0.743}$$
$$\mu_R = \mathbf{0.010}$$

It is worth noting that the identified drag coefficient is higher than expected. Due to all the equipment and wires both on the roof of the vehicle (cameras and LIDAR) and hanging off the side of the vehicle (VMS) the higher value is reasonable. Once the VMS is removed, the drag coefficient will likely drop; however, it is difficult to determine how much it will drop since the VMS is needed to identify the drag coefficient in the first place. Other tests could be performed in addition to the above tests, recording the vehicle acceleration and velocity with the IMU, in order to get an estimate of the drag coefficient once the VMS is removed.

The test was repeated multiple times both up and down the runway. Figure 3.9 shows the results from the downhill test as opposed to the uphill test. The gravitational force for this curve is negative since the gravitational force was pushing the vehicle forward as opposed to resisting the movement. It is also worth noting that on the downhill test the vehicle didn't slow down as much since there was less resistive force acting on the vehicle. Consequentially the variation in the drag force forces are reduced since the change in vehicle speed is reduced.

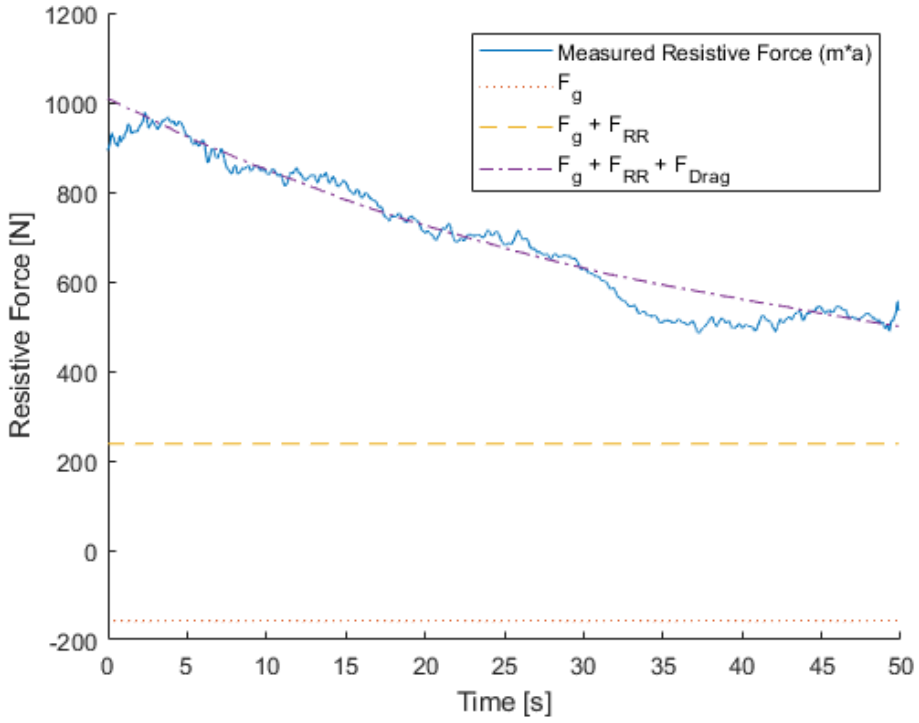

Figure 3.9: Resistive forces for downhill maneuver

In both Figure 3.8 and Figure 3.9 there are sections where the measured resistive force deviates from the calculated resistive force. This can happen for many reasons, such as a change in the wind, a slight change in road slope, or a bump on the road. The road slope was assumed to be constant throughout the runway; however, in reality the road slope is not constant and as such the gravitational force should not be a constant value. This is assumed to be the main contributor to the small errors.

Ultimately the full vehicle dynamic model will be used for simulation and control purposes. As such it is more important that the velocities of the model match up with experimental results as opposed to comparing the resistive forces. Figure 3.10 shows the measured and simulated velocity of the vehicle over

time. The data was normalized in order to compare the data from multiple runs. The velocity of the vehicle was divided by the initial velocity and the time was divided through by the total time of the maneuver.

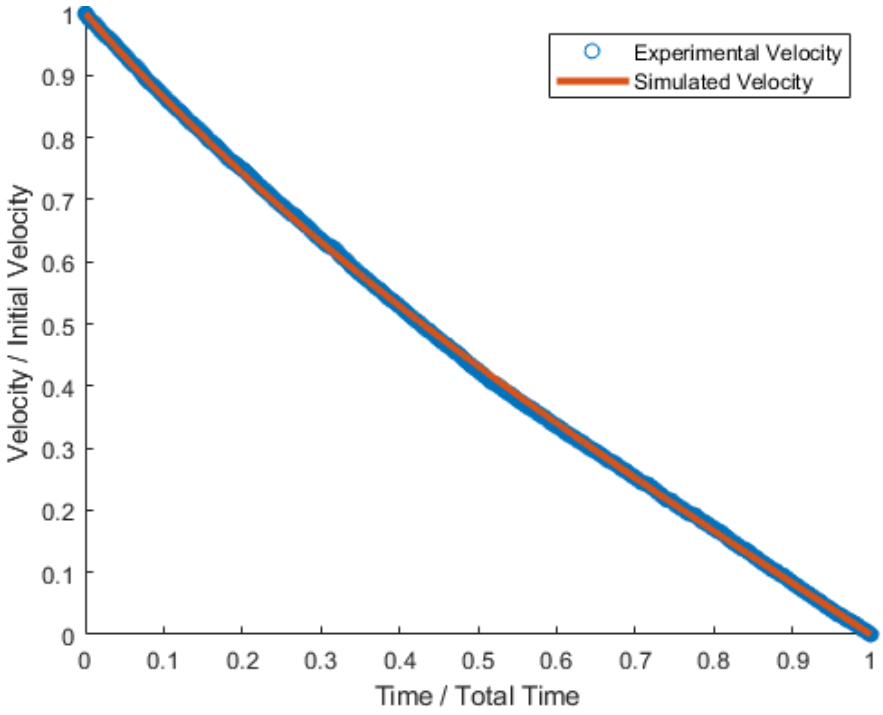

Figure 3.10: Dimensionless velocity versus time comparison between experimental results and simulated model

Even though there are minor deviations in the measured and simulated forces, the measured and simulated velocities match quite closely. As mentioned earlier, the identified coefficient of drag includes all the drag effects of the VMS. Once the VMS is removed the coefficient of drag will need to be modified. Similarly, if additional hardware is added to the roof of the vehicle that will further change the drag characteristics of the vehicle.

3.2.4. Suspension

3.2.4.1. 4-Post Testing

4-Post testing was conducted on the vehicle by Multimatic [54] as detailed in Section 2.2.4. They were able to identify the spring constant and damping coefficient of the car; however, since the vehicle has a semi-active suspension system, the values identified will not always be accurate. Due to the limitations of 4-post testing, the vehicle must remain in park during testing. While the vehicle is in park, the semi-active suspension system is not active. Consequentially the 4-post testing cannot help to identify the semi-active control logic.

It was also mentioned by Multimatic that the observed spring behaviour was highly non-linear. Unfortunately. the standard model they use for identification can only handle a linear spring, so the spring constant for an idealized linear spring was provided. Figure 3.11 shows the model used by Multimatic in order to identify the suspension parameters.

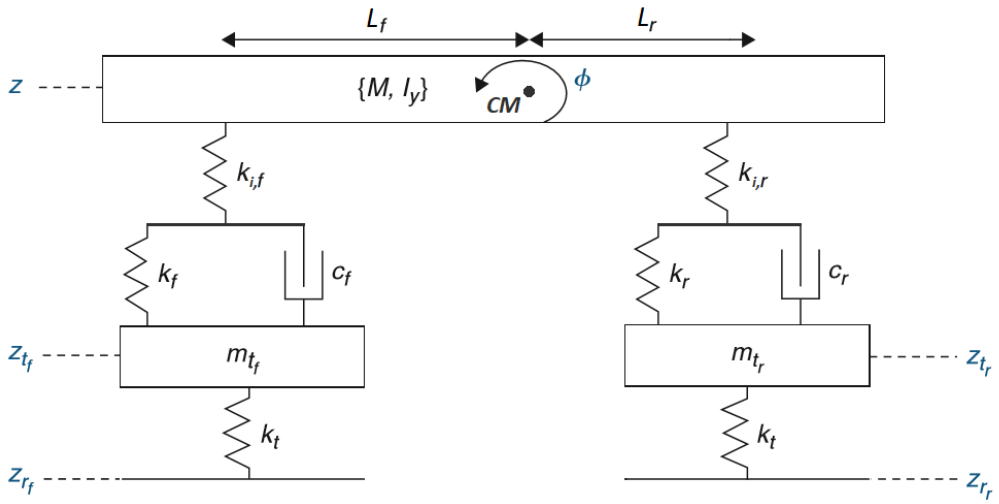

Figure 3.11: Suspension model for 4-post testing

The raw test data was provided in addition to the identified suspension values. A colleague, Marshall Mykietyshyn, processed all the provided data and identified similar values, validating the values received. Table 3.4 shows the values identified by Multimatic and Marshall Mykietyshyn [42]. The estimated values are close to the identified values. Since the parameters from Multimatic have been validated, they are used as the starting values during the next set of suspension testing outlined in Section 3.2.4.2.

		Multimatic Values		Estimated Values	
Parameter	**Units**	**Front**	**Rear**	**Front**	**Rear**
Installation Stiffness	[N/mm]	520.8	754.0	518	740
Tire Stiffness	[N/mm]	388.8	344.9	380	355
Suspension Stiffness	[N/mm]	54.59	56.25	43	40
Suspension Damping	[Ns/mm]	56.16	38.06	61	31

Table 3.4: Suspension parameter identification using data from 4-post testing

3.2.4.2. Road Testing

Starting with the values determined in Table 3.4, further work is needed to determine how the damping coefficient changes based on the vehicle's movement. First, a brief analysis of the suspension stiffness is done to validate the results. Based on the model in Figure 3.11, a simple free body diagram of the tire is developed.

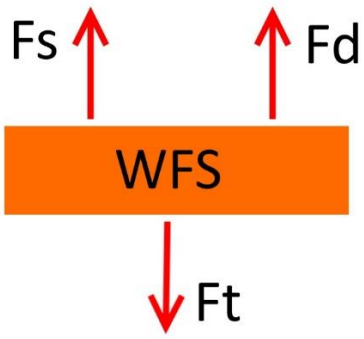

Figure 3.12: Free body diagram of one tire

The free body diagram above is used to formulate the force balance equation in Equation 3.22.

$$F_{Spring} + F_{Damper} - F_{Tire} = m_{Wheel} a_{Wheel} \tag{3.22}$$

The mass of the wheel is known. The acceleration of the wheel is determined by using the LGS readings for wheel height and numerically differentiating twice. This introduces some error, but it was found to be negligible. The tire force is measured through the WFS, leaving only the forces from the spring and damper forces. Using the identified spring constant from the 4-post testing, the damping force can be isolated. Figure 3.13 shows the damping force with respect to the rate of change in spring compression.

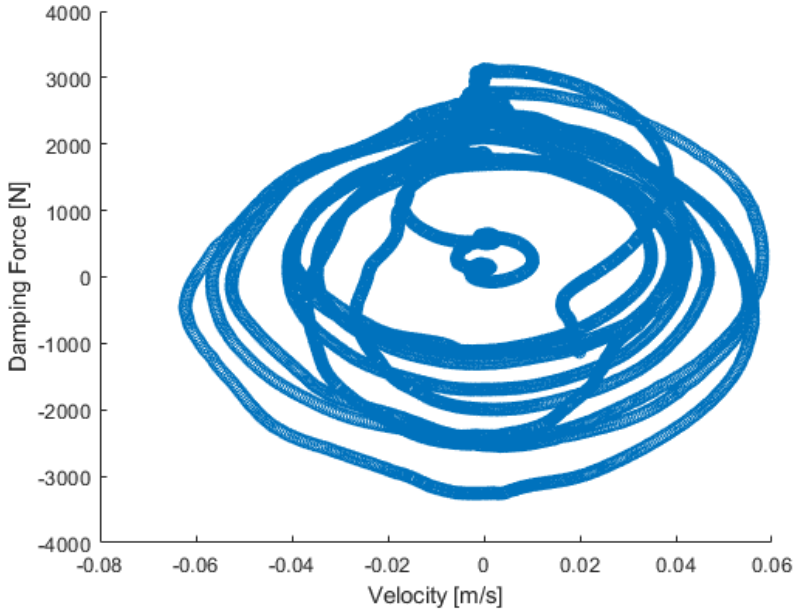

Figure 3.13: Damping force versus rate of change of suspension compression

Based on Figure 3.13 the damping force seems to be highly dependent on position rather than velocity. As the spring compresses (negative velocity) the damping force goes from positive to negative. At some compression point there is zero damping force even though there is still some velocity. This may be because of the damping control law; however, it may also be because of the spring constant identified from the 4-post testing. The later possibility is confirmed by observing the damping force while the velocity is zero. The damper is still only able to produce force when the suspension is compressing/decompressing, just like a normal damper. This means that the damping force is zero when the suspension is not moving, contrary to what is seen in Figure 3.13. Consequentially the spring forces must be re-evaluated.

The moments when the suspension is not moving are found by numerically differentiating the values received from the WPS. All times when the value is near zero are moments when the suspension is not moving. By using data only from these moments, where the damping force is known to be zero, the spring force can be found. Assuming a linear spring, shown in Equation 3.23, the spring constant, k, is solved for as seen in Equation 3.24.

$$F_{Spring} = k(x - l_0) \tag{3.23}$$

$$k(x - l_0) = m_{Wheel}a_{Wheel} + F_{Tire} \tag{3.24}$$

$$k = \frac{m_{Wheel}a_{Wheel} + F_{Tire}}{(x - l_0)}$$

Figure 3.14 shows the spring constant versus spring compression from Equation 3.24. The results show that the spring is highly non-linear, corroborating what Multimatic had observed. In fact the spring can be represented by the exponential function shown in Equation 3.25.

$$k = \mathbf{604,500}e^{(\mathbf{-25.7}x)}\ [\boldsymbol{Nm}] \tag{3.25}$$

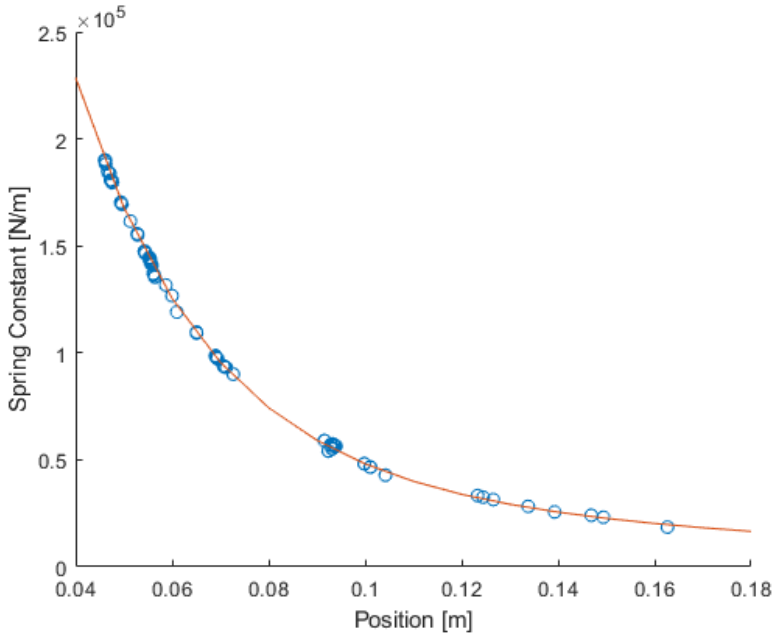

Figure 3.14: Non-linear behaviour of suspension spring

Based on Equation 3.24, the spring force is found for every data point and used to solve for the damping force in Equation 3.22. Figure 3.15 shows the resulting damping force with respect to the rate of change in spring compression.

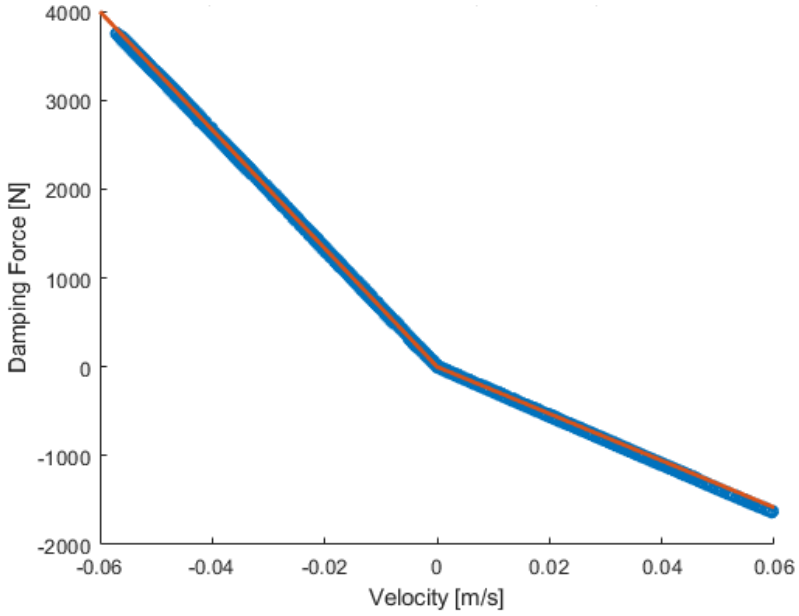

Figure 3.15: Damping force versus rate of change of suspension compression (non-linear spring)

Now the damping control law can be easily seen. The damping coefficient only changes when the velocity of the damper changes from positive to negative, or visa versa, according to Equations 3.26-3.28.

$$F_{Damper} = C\dot{x} \tag{3.26}$$

$$C_{\dot{x}>0} = \mathbf{26.3 \times 10^3} \left[\frac{\boldsymbol{Ns}}{\boldsymbol{m}}\right] \tag{3.27}$$

$$C_{\dot{x}<0} = \mathbf{68.6 \times 10^3} \left[\frac{\boldsymbol{Ns}}{\boldsymbol{m}}\right] \tag{3.28}$$

It is important to note that the damping coefficients above were determined using a simplified quarter-car model with experimental data gathered with the VMS. The data in Figure 3.15 appears smooth due to many of the simplifications in the model. Due to this, the actual semi-active control law may be more complicated than outlined in Equations 3.27 and 3.28.

3.2.4.3. Single/Double Equivalent Kinematic Joints

One important feature of the suspension system is the trajectory of wheel travel. In many models it is assumed that the suspension only allows vertical travel; however, as the suspension compresses and decompresses, the camber and toe angles also change slightly. Normally, to identify the suspension trajectory an in-depth analysis of the kinematic assembly of the suspension is required. With the WPS this can be completed much easier through the use of single and double equivalent kinematic joints (SEK/DEK joints) [55]. These joints express all wheel motion – lateral, longitudinal, camber angle and toe angle – as functions of the vertical movement of the tire.

The vehicle chassis was raised by a single corner in order to measure the change in wheel position. Ideally, the entire chassis would be lifted and suspended above the ground using a full vehicle lift. Then each wheel could be lifted and measured independently. Unfortunately this was not possible with the equipment available. Instead the chassis was raised near each of the wheels in turn. Resultantly, the change in longitudinal and lateral positions is erroneous due to the tires contact with the ground. In general, these values do not vary greatly and can be ignored without introducing significant of error. Figure 3.16 shows the change in height of the wheel over time.

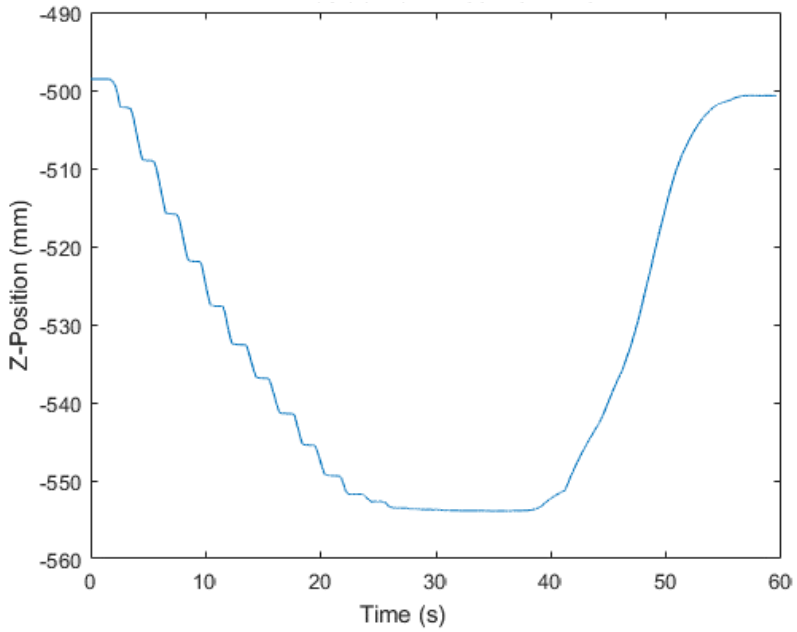

Figure 3.16: Change in wheel height over time

During the beginning of the test the car was raised through the use of a jack. This is the cause of the step-like features. Once the limit of motion was reached, where the wheel and chassis were moving

in tandem, the jack slowly lowered the vehicle back to the ground. Figure 3.17 shows the lateral position vs. height. The point (0,0) in the figure is arbitrary and depends on the installation conditions. Consequentially, only the relative displacements are important. The smallest Z-Position value (-554) represents the spring at full extension. Likewise, a smaller Y-Position value represents the tire being further from the center of the vehicle. Therefore, as the spring extends, the wheel moves inwards, closer to the center of the vehicle as is expected.

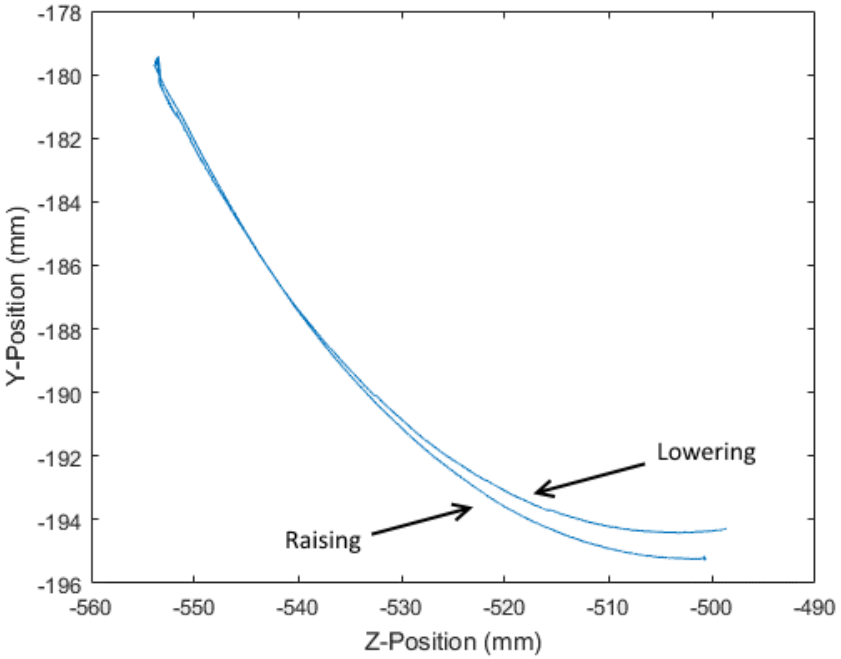

Figure 3.17: Lateral position of the wheel with respect to the vertical position of the wheel

The curve should look like a single line, but two distinct curves can be seen. One represents the raising of the chassis and the second represents the lowering of the chassis. The ends of these curves should be in the same location since the tire should not have moved, but due to the tire contact with the ground, external forces have caused the ending locations to be slightly different. Due to this error, the longitudinal and lateral results have been ignored. For future testing, the vehicle should be lifted off the ground first to avoid erroneous data.

The camber and toe angles are plotted with respect to the height of the wheel in Figure 3.18 and Figure 3.19 respectively.

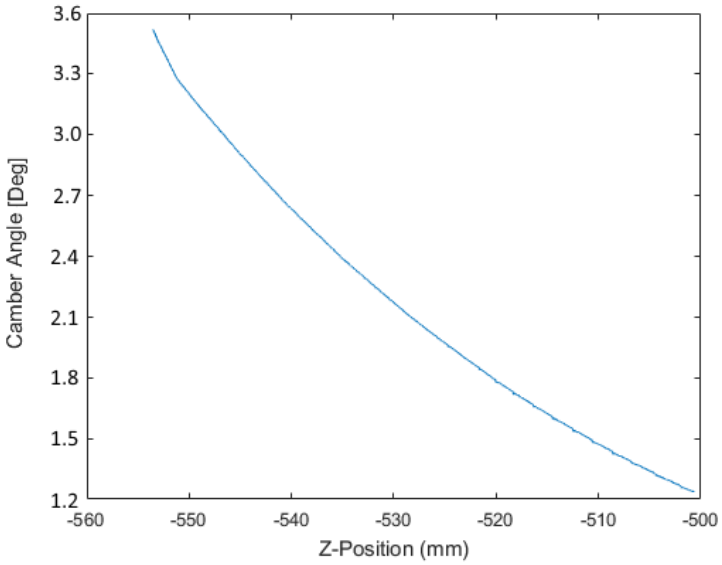

Figure 3.18: Camber angle of the wheel with respect to the vertical position of the wheel

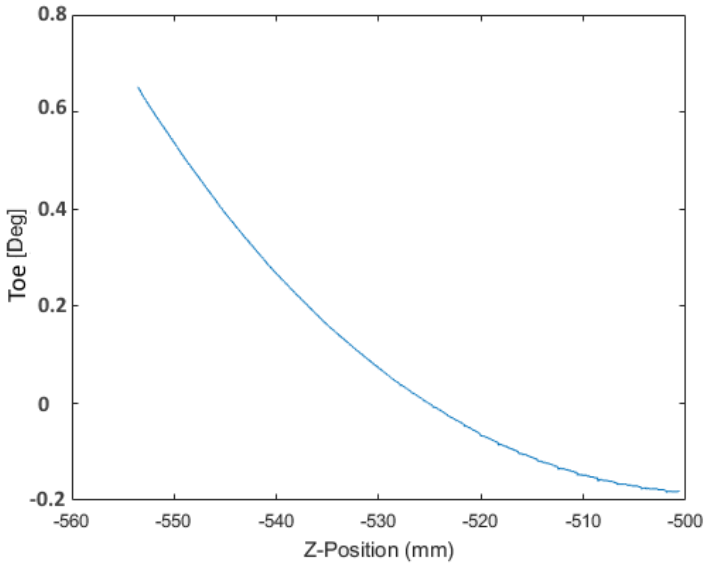

Figure 3.19: Toe angle of the wheel with respect to the vertical position of the wheel

It is worth noting that the change in toe angle is small and was later deemed inconsequential. To simplify the model the change in toe angle is ignored, leaving camber angle as the only remaining variable. The camber angle data is put through a spline-generating program in order to generate equations that relate the camber angle of the tire with the change of height between the tire and the chassis. A custom Matlab code is used in order to convert these splines into kinematic constraint equations which are then implemented in a custom MapleSim joint used for the suspension.

3.2.5. Tire Modelling

To use the data for tire modeling, some processing must be done. Primarily, the sideslip angle and longitudinal slip ratio must be calculated. Longitudinal slip is defined in Equation 1.1. Since longitudinal slip is calculated by dividing through by the vehicle speed, all test points where the vehicle speed is zero will cause a singularity. These data points generally all occur before or after the test maneuvers and must be removed.

The sideslip angle is calculated by observing the longitudinal and lateral speed of the tire, measured by the LGS. If there is no lateral speed, then the tire heading is the same as the tire direction of motion, meaning the sideslip angle is zero. If lateral speeds are observed then the resultant direction of motion is found using the Pythagorean theorem. A simple trigonometric identity gives the sideslip angle of the tire. This is outlined in Equation 3.29. Note that the longitudinal and lateral speeds are in the local tire frame.

$$\alpha = \tan^{-1}\left(\frac{Lateral\ Speed}{Longitudinal\ Speed}\right) \tag{3.29}$$

As described in Section 1.3.2, the tire forces depend upon the normal load experienced by the tire. The normal load on the tire is measured and can be accounted for in the model. This is done by dividing the recorded longitudinal and lateral forces by the normal load. This normalization accounts for all the changes in tire behavior due to normal load. The normalized longitudinal Pacejka tire model is shown in Equation 3.30.

$$\frac{F_x}{F_z}(s) = D\sin\left(C\tan^{-1}\left(Bs - E(Bs - \tan^{-1}(Bs))\right)\right) \tag{3.30}$$

It is assumed that the parameters of the Pacejka tire model do not vary based on normal load. In other words, it is assumed that the longitudinal force is directly proportional to the normal load on the tire, and can be normalized according to Equation 3.30. This assumption is consistent with the 1989 version of the Pacejka tire model.

Some post-processing must also be done using measurements from the WPS. During more extreme testing maneuvers, the camber angle of the tires increase. The reference frame of the WFS is fixed to the wheel. Based on this, as the toe and camber angles increase, part of the normal load is actually measured as a lateral force, and vice versa. The toe and camber angles are measured using the WPS. Based on

experimental data, the toe and camber angles only change a small amount (1-2^{o}) due to the semi-active suspension system on the Lincoln MKZ. The maximum recorded change in camber angle during testing was 2.3 degrees. This data is used to apply a coordinate transformation to the measured forces from the WPS to ensure that the normal loads are normal to the road. Through this process any forces due to the camber angle is accounted for.

Lastly, since the tire forces are measured at the center of the wheel hub, post processing is done to determine the forces at the tire contact patch itself. First, a simple coordinate transformation is necessary to identify the forces at the contact patch itself. In addition, an inertial force is observed due to the WFS, the wheel, and the tire itself. This force can be seen by observing the forces on the rear wheels. Since the rear wheels are not driven, the only applied force seen is due to any braking force and the inertial force. Figure 3.20 shows the observed forces seen on a rear wheel.

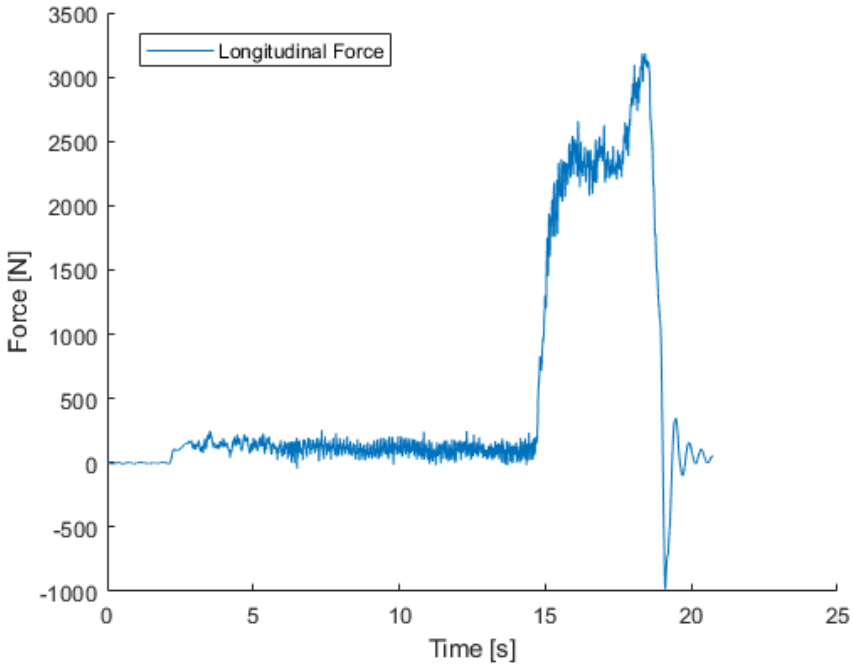

Figure 3.20: Measured longitudinal force for rear wheel

This set of data is for a simple acceleration and braking maneuver similar to the maneuver shown in Figure 2.6. While the vehicle is accelerating there is a small force seen at the wheel due to the inertial force. Later in the maneuver the brakes are applied and a larger force is observed. The small inertial force seen throughout the maneuver is measured and used to adjust the measured forces of the other wheels in order to account for the inertial force of the tire.

3.2.5.1. Pure Longitudinal Slip Pacejka Model

The normalized pure longitudinal slip Pacejka model, detailed in Equation 3.30, depends solely on longitudinal slip. As stated earlier, many other factors also influence the longitudinal force. Many of these factors are taken into account during data processing, such as inertial force; however, many of these factors are also ignored in order to simplify the model, such as wheel temperature and variable road friction. Note that all tire testing was completed on dry pavement during warm summer months. Figure 3.21 shows the processed data for the pure longitudinal slip acceleration/braking test. The x-axis is the longitudinal slip and the y-axis is the dimensionless normalized longitudinal force. It is assumed that the tire pressure remains constant throughout the test. Each tire was inflated to 35 psi before each round of testing to ensure the pressure remained at a known constant value.

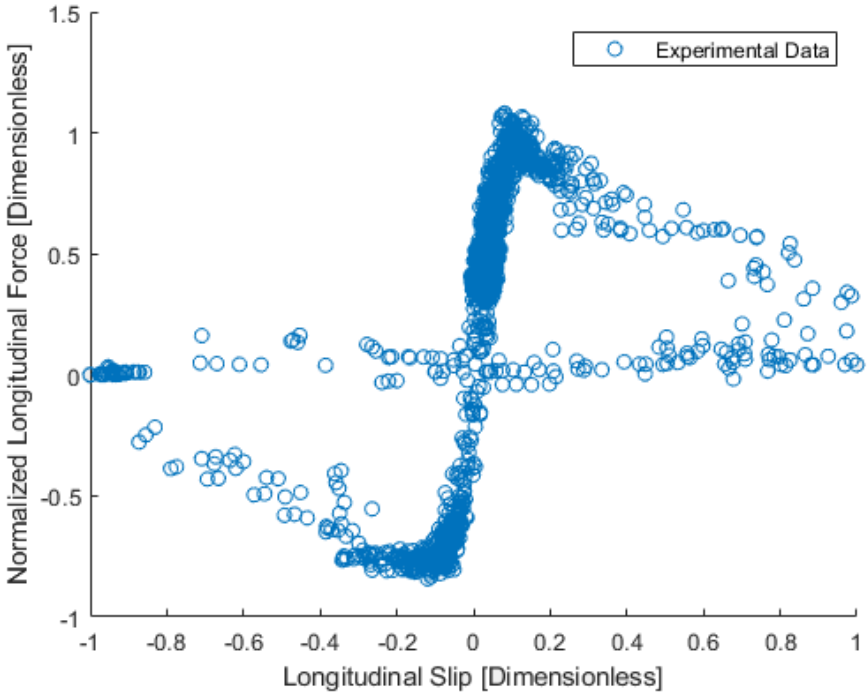

Figure 3.21: Measured data from pure longitudinal slip test

It can be seen that many of these data points are erroneous. There should be no high slip values that provide a near-zero force. These data points are all erroneous values that occur when the vehicle is at a near-zero speed. From the definition of longitudinal slip, it can be seen that when the vehicle speed is near-zero the slip values are more prone to error. Post-processing removes all singularities by removing all data points with a vehicle speed of zero; however, near-zero speeds will also cause erroneous data due to the asymptote. By removing these values, a more representative data set is obtained.

Using this data set, a nonlinear least squares optimizing routine is performed to identify the Pacejka parameters in Equation 3.30. This was done using the Matlab Curve Fitting toolbox. The parameters for this Pacejka tire model are provided in the Appendix. The resulting Pacejka curve is shown with the experimental data set in Figure 3.22. In addition, a linear tire model is also fit to show a comparison between these two models.

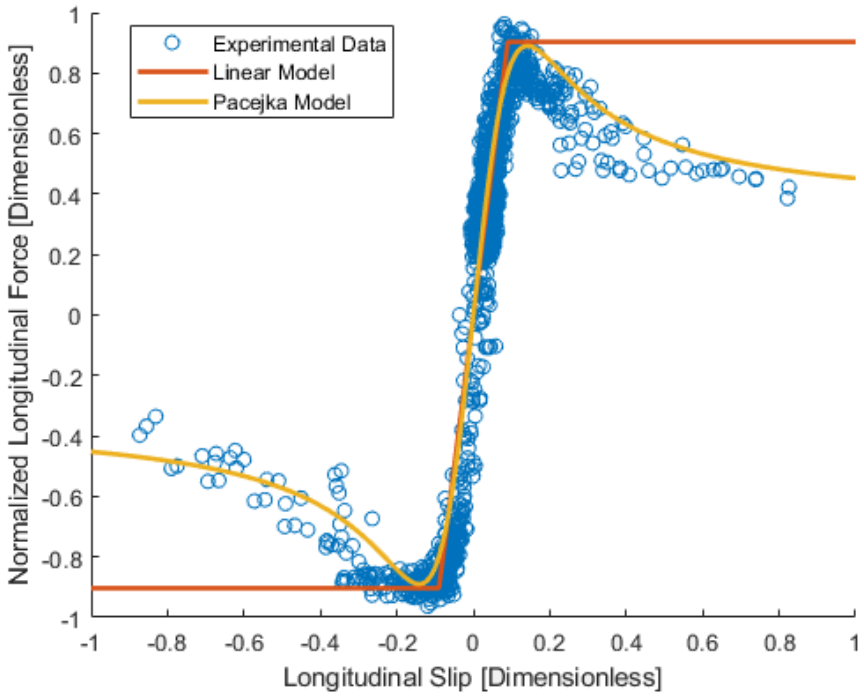

Figure 3.22: Normalized longitudinal force versus pure longitudinal slip

The linear tire model shown in Figure 3.22 is accurate for small values of longitudinal slip. The linear tire model is much simpler than the Pacejka model; however, the use of the linear tire model is limited. Likewise, the pure longitudinal slip 1989 Pacejka tire model is much simpler than other tire models like the 2012 Pacejka or TAME models, so it also has limited use as detailed in Section 1.3.2.

The pure longitudinal slip Pacejka model was developed using data points from every run of the test specified in the Section 2.2.5. It is worth noting that when performing the optimization for only the data points for each individual run, the resulting parameters only differ by a maximum of 1.8%. This helps validate the repeatability of the designed test.

3.2.5.2. Pure Lateral Slip Pacejka Model

The pure lateral slip model is determined in a similar fashion as the pure longitudinal slip; however, instead of longitudinal slip, the sideslip angle is used. Sideslip is defined as the angle between the heading of the wheel and the instantaneous direction of motion of the wheel. Details for calculating the sideslip angle based on experimental data are found near the beginning of Section 3.2.5. Like the longitudinal model, the lateral tire force is divided through by the normal load to calculate the normalized lateral force. By normalizing the lateral force, the change in lateral force due to the normal load is accounted for.

Like the pure longitudinal slip model, there are a number of erroneous data points while the vehicle is near zero speed. This is due to the calculation of the sideslip angle, calculated by dividing by the longitudinal speed of the wheel. After removing the erroneous data while the vehicle was near zero speed and combining the data from each of the three different tests performed, a comprehensive data set is achieved. The data points are plotted in Figure 3.23. An optimization routine is run in order to determine the Pacejka curve parameters necessary for the model to fit the data. The parameters for this curve are shown in the Appendix.

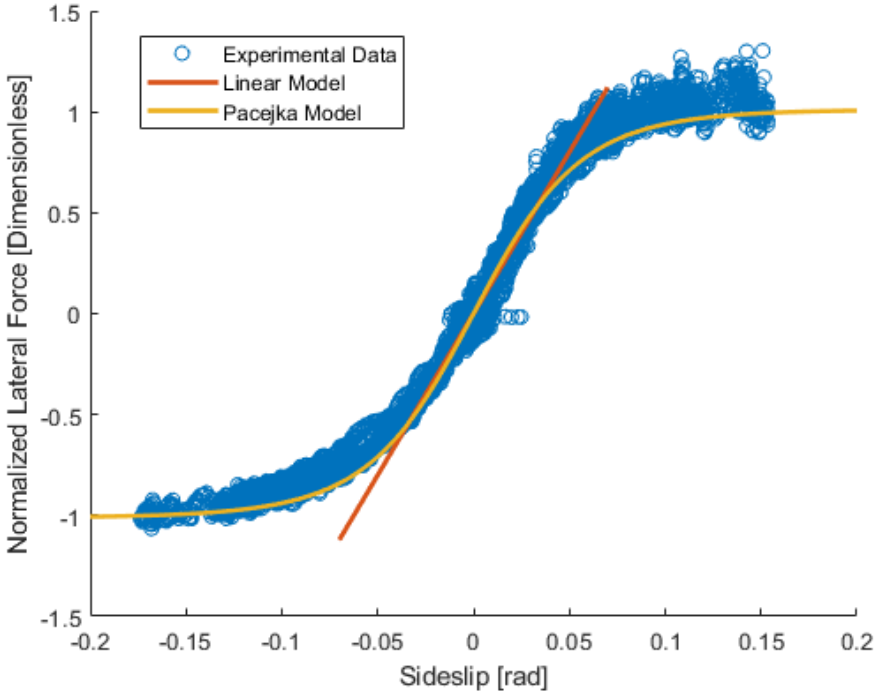

Figure 3.23: Normalized lateral force versus pure sideslip

It is worth noting that the experimental data points shown in Figure 3.23 have a higher standard deviation than the longitudinal results in Figure 3.22. This is seen as the thickness of the experimental curve. The standard deviation is larger due to multiple reasons. Primarily it is due to many of the simplifications that were used for this model, such as neglecting camber thrust and temperature changes. It was observed that the tire temperature varied more during the lateral tests than during the longitudinal test.

The increased standard deviation is also likely due to the normalization process. The normal load observed on the tires vary more during the lateral tests as opposed to the longitudinal tests. These transients increase the standard deviation.

3.2.5.3. Combined Slip Pacejka Model

The combined slip model is more complicated than either of the longitudinal or lateral models due to the effects of the friction ellipse [35-39]. The friction ellipse is based on Equation 3.31:

$$\frac{F_{x\_max}^2}{\mu_x^2} + \frac{F_{y\_max}^2}{\mu_y^2} = {F_z}^2 \tag{3.31}$$

where μ_x is the coefficient of friction in the longitudinal direction and μ_y is the coefficient of friction in the lateral direction. The longitudinal and lateral coefficients of friction are different due to the tire treads. As the tire treads wear, the coefficient of friction decreases. It is assumed that the tire treads will not wear down significantly during the duration of the testing. Since it is also assumed that the surface of the road is dry pavement, the coefficient of friction is assumed to be constant throughout each maneuver. A visual representation of the friction ellipse is shown in Figure 3.24.

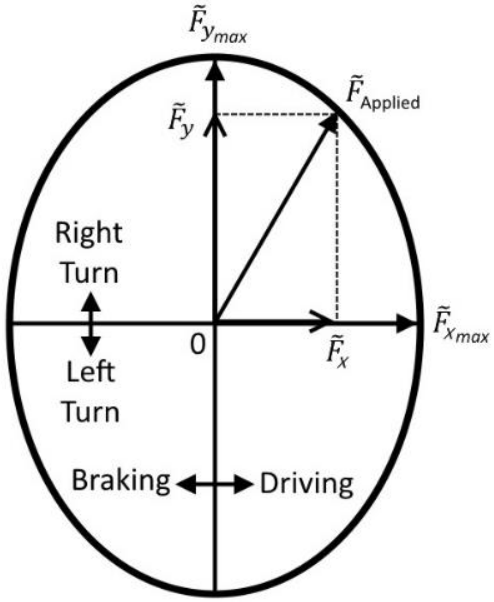

Figure 3.24: Visualization of the friction ellipse

There is a maximum amount of force available to be applied by the tire. If force is only applied in the longitudinal direction, pure longitudinal slip, then the maximum available force is $\tilde{F}_{x_{max}}$. Likewise, if force is only applied in the lateral direction, pure lateral slip, then the maximum available force is $\tilde{F}_{y_{max}}$. When force is applied in both the longitudinal and lateral directions, the maximum available force is shown as $\tilde{F}_{Applied}$; the longitudinal and lateral components of this force are less than $\tilde{F}_{x_{max}}$ and $\tilde{F}_{y_{max}}$.

Under normal driving situations this effect is not prevalent due to the low magnitude of the lateral force. The purpose of developing these models is to implement them on an autonomous vehicle. Most maneuvers the vehicle will perform are normal driving situations where this effect is not substantial; however, in a safety-critical situation where an autonomous vehicle must try to avoid an obstacle, this reduced maximum force is vital information.

Because of this, a combined slip model is developed. The following work is completed for both the longitudinal and lateral combined slip models; however, since the process for both of these models is identical, only the longitudinal work will be presented. The data gathered through the two combined slip tests are compiled together and any erroneous data is removed, just as it was in the pure slip models. To determine if there is actually a large effect on available forces during combined slip conditions, the normalized longitudinal force is plotted against the normalized lateral force. The resulting plot is cluttered due to the large number of data points. Many of the data points were trimmed for visualization, shown in Figure 3.25.

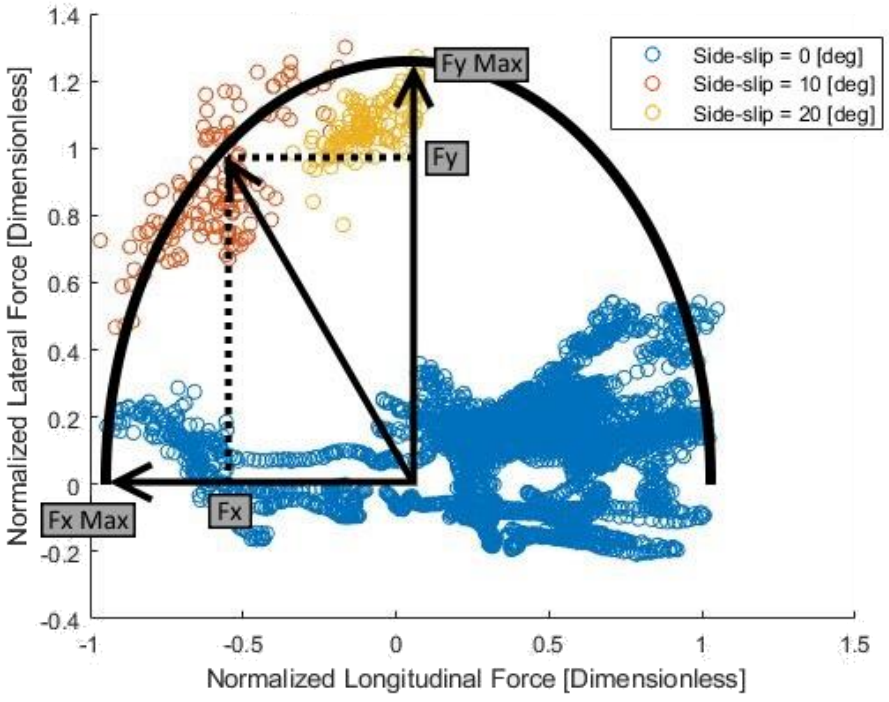

Figure 3.25: Normalized longitudinal force versus normalized lateral force

It is worth noting that every point inside the friction ellipse is a feasible point. The tires do not need to apply the maximum available force, rather they are limited by the maximum force. This is why many of

the data points in Figure 3.25 are arrayed inside the border of the ellipse. As the sideslip values increase, the longitudinal force observed decreases while the lateral force increases. Only a few of the data points for larger sideslip values are shown; however, it is easy to see that as the lateral force increases the available longitudinal force decreases. It is important to note that the high lateral force values only occur during high sideslip values as expected. The low lateral forces shown for near zero sideslip values are necessary for vehicle stability.

From Figure 3.25 it is seen that as the absolute value of the lateral force increases, the longitudinal force decreases. Consequentially, the longitudinal slip was plotted against the normalized longitudinal force to determine the differences in the longitudinal Pacejka model. This can be seen in Figure 3.26. By adding a third dimension for the sideslip (different colors), one can see the impact it has on the available longitudinal force.

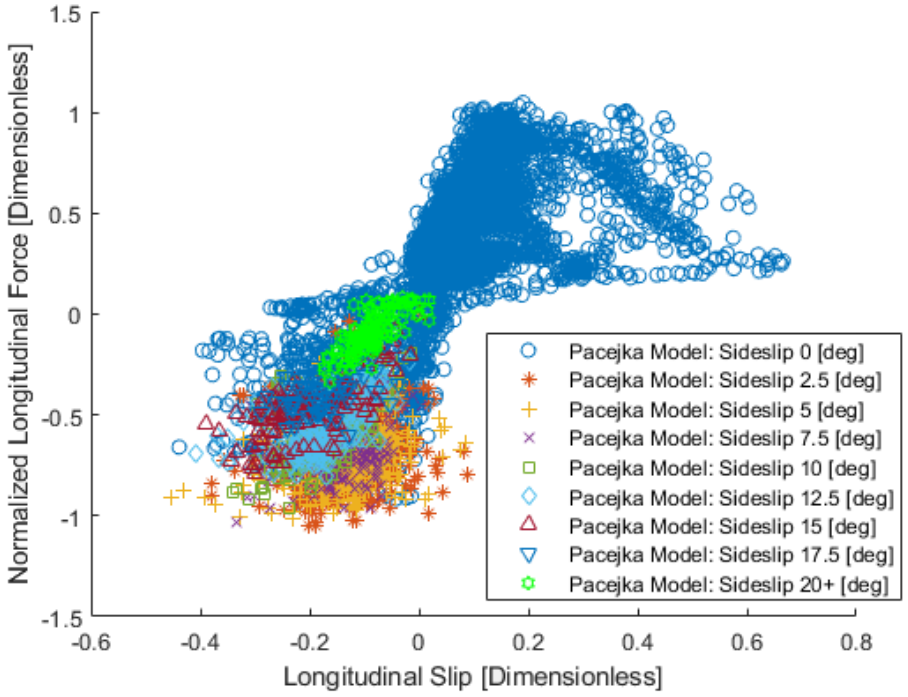

Figure 3.26: Longitudinal slip versus normalized longitudinal force with varying sideslip

The most substantial change is seen when observing the data points with a sideslip angle of twenty degrees. It is clear that if a linear tire model was optimized around these data points, as opposed to the near zero sideslip data points, the slope of the model would be significantly different. This is the main impact that needs to be captured by the combined slip tire model.

It is important to note that large sideslip values are only shown in the negative longitudinal slip (braking) range. The sideslip values observed in the positive longitudinal slip range are ignored only for visualization purposes; they are included in calculations. In addition, it is worth noting that sideslip values exceeding 15 degrees are only seen in the braking region. This is expected, due to mechanical limitations, as outlined in Section 2.2.5. The combined slip models will mainly be used in safety critical situations, when the only objective is avoiding an obstacle. During these types of situations, it is likely that the vehicle will attempt to steer away from the obstacle while braking, not accelerating. Consequentially, the combined slip models are optimized more for the braking region than the accelerating region.

To create a combined slip model, a continuous function is needed to account for the change in longitudinal forces due to lateral forces and vice versa. This is accomplished by creating a piecewise function and then fitting a spline to link the identified data points.

Using specific data points, multiple Pacejka curves are optimized around the different sideslip values. Curves are optimized for sideslip values of 0 (pure longitudinal slip), 2, 5, 10, 15, 20, and 25 degrees. These values were chosen due to the distribution of data points. The optimization process is identical to the process outlined in the pure slip models. More values can be used to increase the fidelity of the model. Assuming symmetry consistent with the Pacejka model, identical curves are used for each corresponding negative sideslip value. To increase the fidelity, new curves could be fitted for this negative region. The identified Pacejka parameters are presented in the Appendix along with the parameters for the lateral combined slip Pacejka curves.

Three of the resulting curves, for 0, 10, and 20 degrees sideslip angle, are shown in Figure 3.27. The experimental data shown in Figure 3.27 is the same as that in Figure 3.26; however the sideslip values were ignored for visualization to highlight the three different curves.

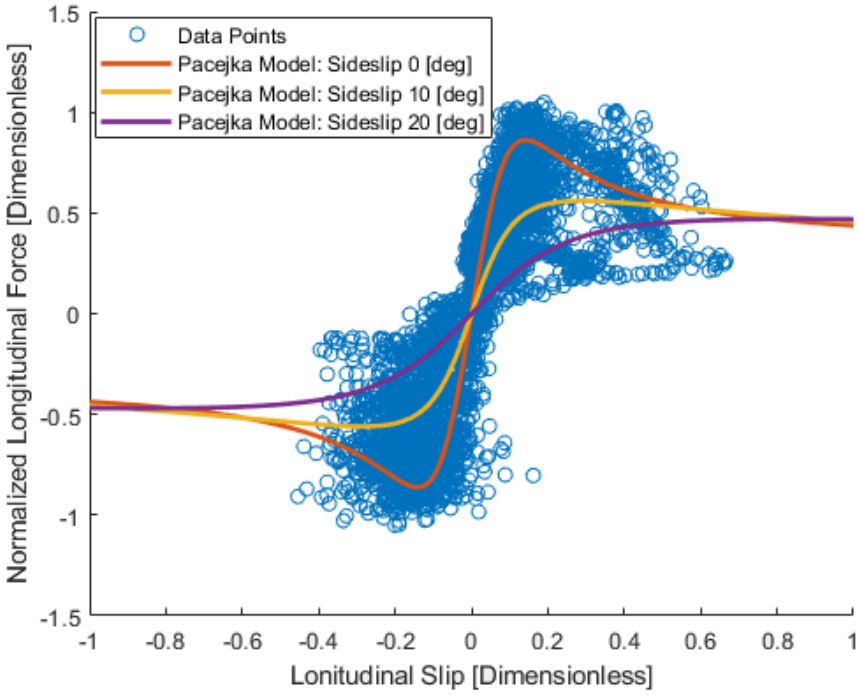

Figure 3.27: Combined slip Pacejka models for sideslip values of 0, 10, and 20 degrees

As sideslip angle increases, the maximum available longitudinal force decreases significantly. This decrease is not linear, which is why the piecewise functions are necessary to obtain an accurate representation of the full combined slip model. This data could be used to determine the parameters of the 2012 Pacejka model. This would eliminate the piecewise nature of the current model; however, it would also require increasing the complexity of the model significantly. There are other methods that will eliminate the piecewise nature of the combined slip Pacejka model without having to identify the large number of parameters needed in the 2012 Pacejka model.

One such method was developed by MSC Software for use in the 1989 and 1994 Pacejka models [47]. This method involves modifying the coefficient of friction values in order to change the available forces due to combined slip behavior. This is best seen by referring back to the equation for the friction ellipse, Equation 3.31. The coefficients of friction in both the longitudinal and lateral directions become functions of longitudinal slip and lateral sideslip. As the coefficients of friction change, the available forces in each of those directions will also change. Referring to Figure 3.25, the indicated force could be achieved by reducing the coefficient of friction in both directions so as to reduce the maximum forces to the indicated available forces. This method works well when only the pure slip Pacejka models are known, but since the combined slip models have also been developed here, it is not necessary.

Another method for eliminating the piecewise nature of the model is to interpolate the determined values with a spline. This relates the change in slip and sideslip with the change in model parameters by interpolating each of the four Pacejka parameters individually. Using this method, the piecewise curves seen in Figure 3.27 reduce to a single function for longitudinal force which depends upon both longitudinal slip and sideslip angle. Likewise, a lateral model is developed which also depends upon both longitudinal slip and sideslip angle. These functions are valid for all scenarios, including both pure slip and combined slip. Figure 3.28 shows many of the interpolated Pacejka models based on the above method.

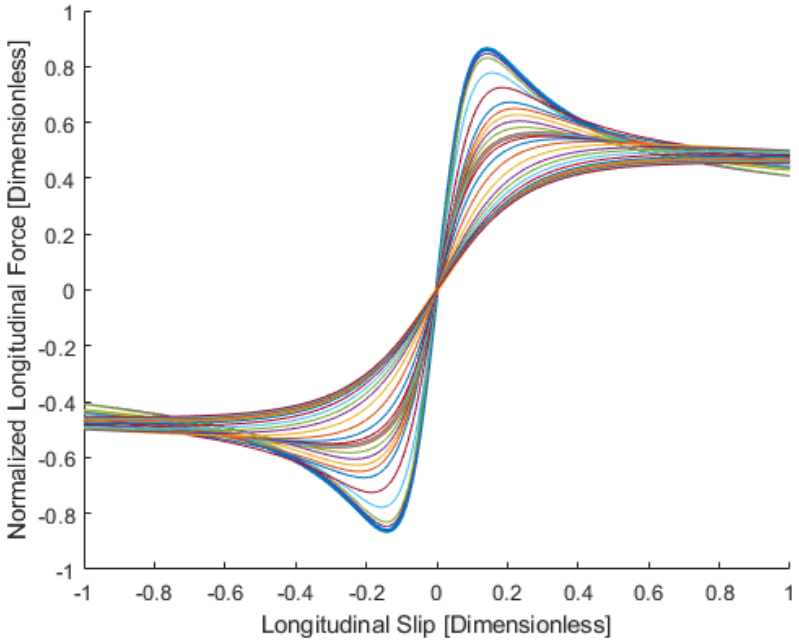

Figure 3.28: Longitudinal Pacejka tire models for sideslip values between 0 and 25 degrees

By interpolating between the identified values, the multiple 2D curves become a 3D surface. This method is used to determine accurate tire models for any combined slip scenario. Each individual tire model presented above has been created using experimental data and validated using a different set of experimental data.

3.3. Parameter Identification Using High Fidelity Vehicle Dynamic Model

After all parameter identification was completed as described in Section 3.2, the parameters were entered into the MapleSim model and a full parameter optimization routine was run. The vehicle model was exported as a Simulink function where a non-linear least squares optimization routine was run to find the parameters that minimized the relative error between the full vehicle model outputs and the experimental results. A series of tests were performed similar to the tests outlined in Section 2.2. Several additional tests were performed at random to ensure that the model was accurate. All parameter values were not allowed to change by more than 25% of the values found from the simpler models found in Section 3.2. This was done to ensure that the optimized values were still feasible. The final parameter values can be found in Appendix B.

4. Full Model Validation

Full model validation is broken down into three sections: longitudinal, lateral, and combined validation. Each validation section contains validation results for a standalone validation test that was performed after the series of tests used for the full model optimization detailed in Section 3.3. Note that all model results are from open loop simulations, meaning that the vehicle states are determined solely based on the inputs of the system. The inputs to the simulated model for all of the following validation maneuvers are the torques at each of the four wheels along with the steering angle.

4.1. Longitudinal Validation

To validate the longitudinal model, an acceleration and braking test was performed. This test was not designed; it was intended to be random. Since the test is for longitudinal validation, there is generally no steer input. The only time the steer input changes is when the vehicle needs to be turned to stay on the test track. Since these tests are meant to validate the full vehicle dynamic model, large variations in acceleration were desired.

The trajectory of the maneuver is shown in Figure 4.1.

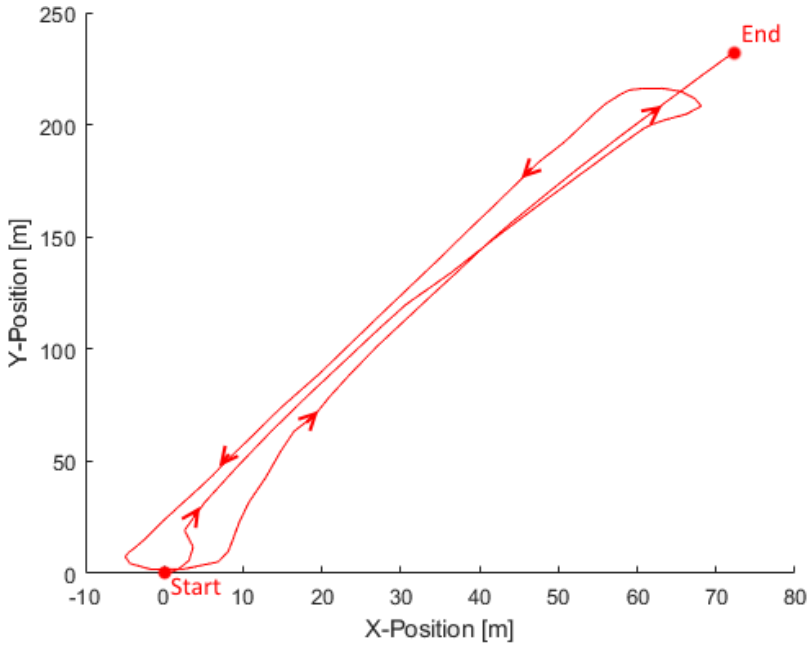

Figure 4.1: Trajectory for longitudinal validation

The maneuver includes three relatively straight-line paths down the length of the test track. The trajectory is generated using the GPS values from the VBox. The longitudinal velocity of the vehicle is found by integrating the acceleration measured with the IMU. The experimental and simulated velocities are shown in Figure 4.2.

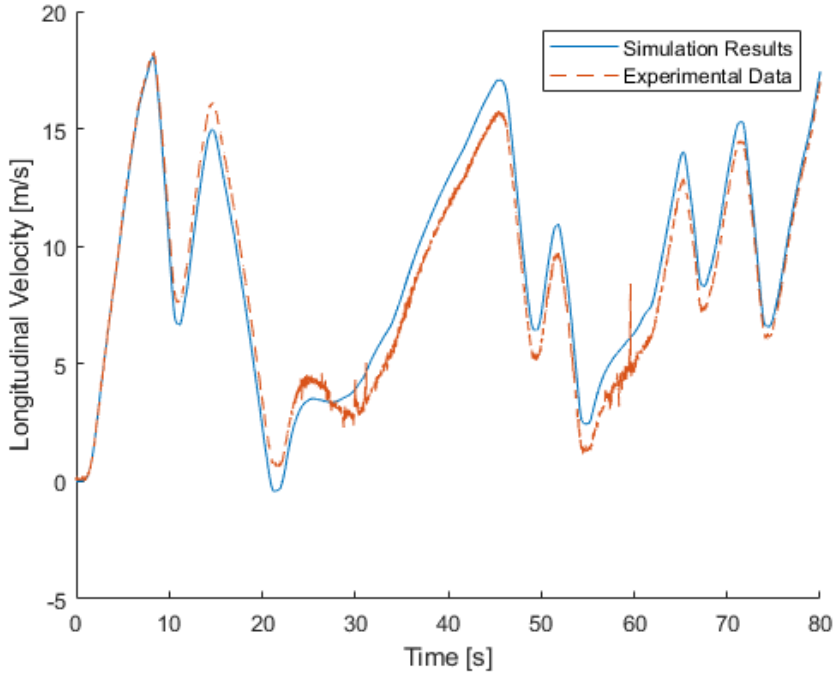

Figure 4.2: Longitudinal velocity versus time for longitudinal validation

It is worth noting that the two sections where the experimental data and simulation results vary significantly are found during 20-30s and 55-65s. These are the two times in the maneuver where the vehicle is turned around. During these sections, the vehicle speed is very small and the experimental data from the IMU is less accurate due to the small changes in vehicle acceleration. This can be seen as an excess level of noise in the experimental values.

Most of the smaller deviations occur after large braking regions. This is common throughout all validation results and is due to the lack of experimental data at the rear right wheel. Since the vehicle is a front wheel drive, the rear wheels only apply torques during braking maneuvers. Due to a sensor malfunction, the rear right wheel of the vehicle was not measured during testing and could not be used as an input to the simulation model. Instead, it was assumed that the same braking torques were applied to both the rear left and rear right wheels. While this is the best approximation that can be determined given the circumstances, it is not entirely accurate and may lead to erroneous data.

To accurately reproduce the vehicle motion in a simulation environment, the accelerations and angular velocities of the vehicle model must match the experimental data. These values are used to validate the model since they are captured directly using the IMU. The experimental data is compared against the simulation data in Figure 4.3 and Figure 4.4.

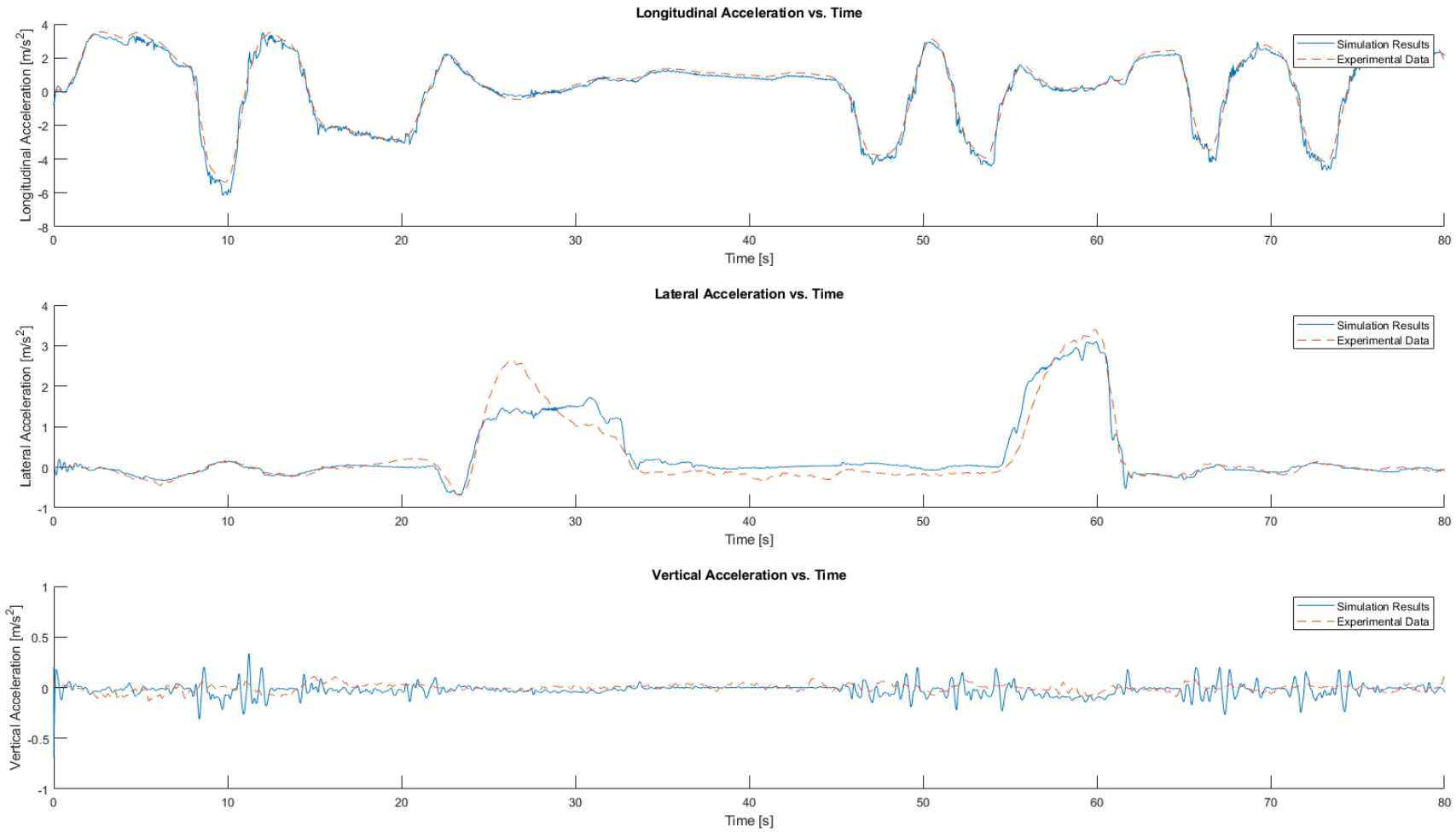

Figure 4.3: Accelerations versus time for longitudinal validation

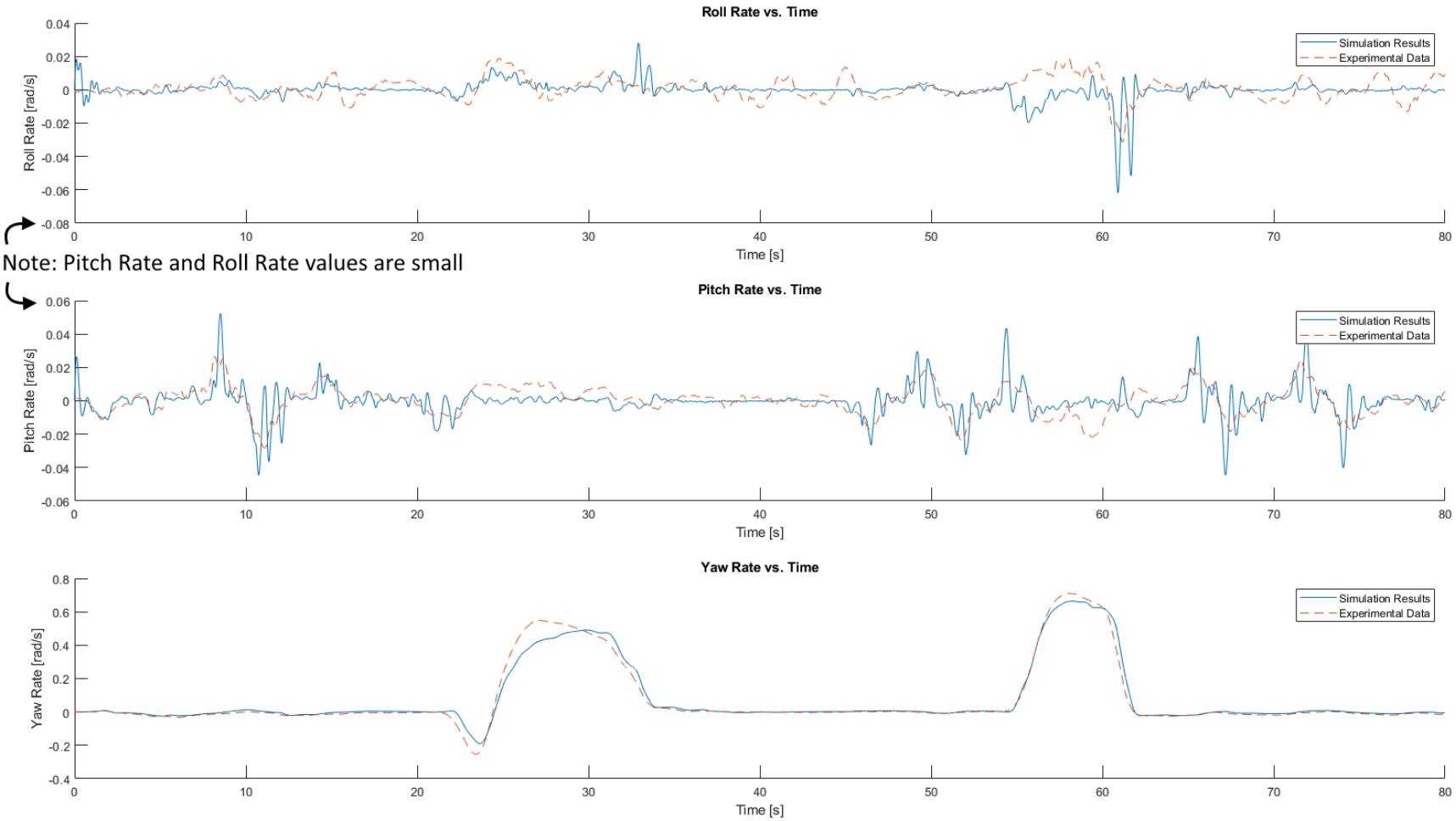

Figure 4.4: Angular velocities versus time for longitudinal validation

Since this test is for longitudinal motion, the most important data to compare is longitudinal acceleration and pitch rate. The longitudinal acceleration of the simulated model lines up well with the experimental data from the IMU. There are only a few points, namely the large braking events at 10s, 53s, 58s, and 72s, where the simulated results are slightly larger than the experimental data; however, the maximum error does not exceed 10% which is well within a reasonable error tolerance. This error is a result of the sensor malfunction described earlier.

It is worth noting that the lateral acceleration results diverge significantly from the experimental results between 25s and 30s. This occurs after the first run down the track, while the vehicle is turning around. The velocity of the vehicle is very small during this maneuver, so even though the error in lateral acceleration is larger, the vehicle does not deviate far from the experimental trajectory.

Both the pitch rate and the yaw rate of the vehicle are very small, as can be seen by the limit on the y-axis of the top two plots in Figure 4.4. The simulated pitch motion follows the basic trend of the experimental data; however, the simulated data shows more high-frequency responses as opposed to the experimental data. This is also seen in the longitudinal data results. The major reason for this difference is the internal filtering of experimental data by the IMU, whereas no filtering or smoothing has been performed on the simulated data results.

Overall it is found that the simulated model follows the general curve of the experimental results, showing that the model is an accurate representation of the vehicle during longitudinal motion.

4.2. Lateral Validation

The lateral validation was performed using a swerving maneuver. Like the test for the longitudinal validation, the lateral validation test was randomized to ensure the accuracy of the model during any situation. Since this test is for validating the lateral motion of the vehicle, the cruise control was turned on during the maneuver to minimize longitudinal acceleration. The trajectory of the vehicle during the test is shown in Figure 4.5.

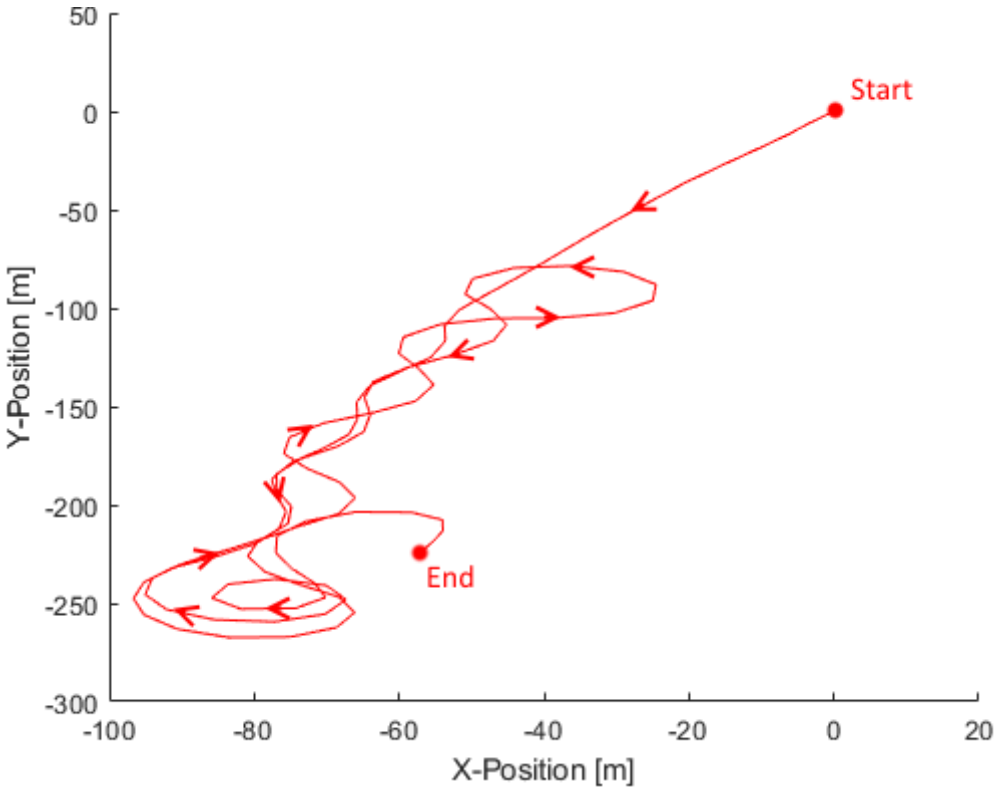

Figure 4.5: Trajectory for lateral validation

The maneuver started with a rapid acceleration segment for the sole purpose of bringing the vehicle up to a constant speed. Once the desired speed was reached, the vehicle was put into cruise control and swerved back and forth randomly. As the vehicle approached the end of the test track, the vehicle was turned around while maintaining cruise control.

The longitudinal velocity of the vehicle is shown in Figure 4.6. The longitudinal velocity of the vehicle is found by integrating the acceleration measured with the IMU.

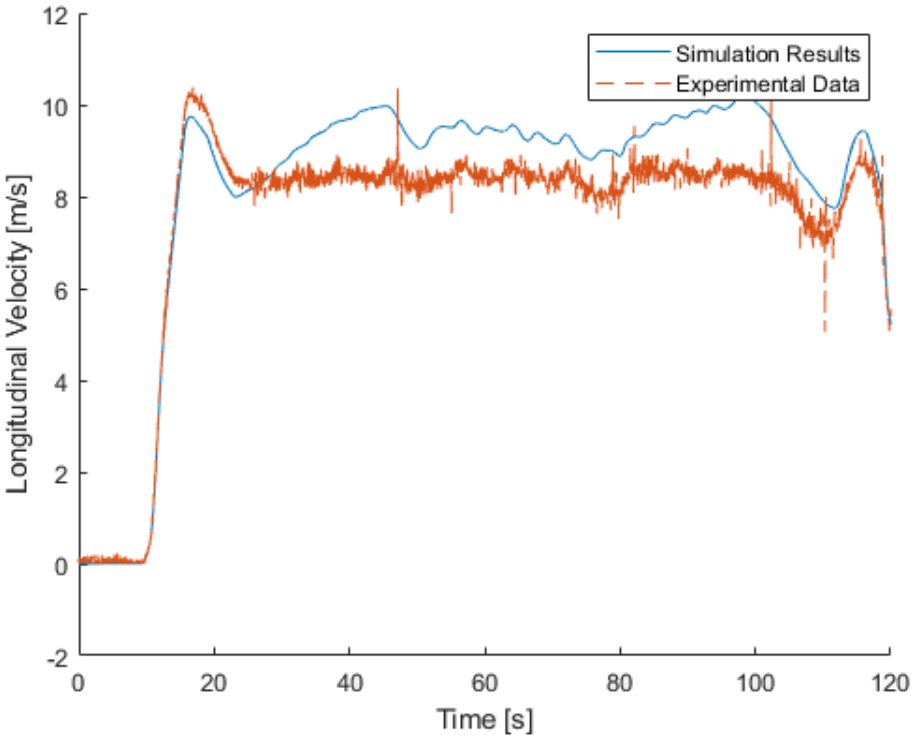

Figure 4.6: Longitudinal velocity versus time for lateral validation

The experimental data for longitudinal speed is noisy during cornering maneuvers due to the cross-coupling with yaw rate. The simulation results seem to track the initial longitudinal acceleration well, but then the results deviate from the experimental data. This deviation is largely due to small differences seen in longitudinal acceleration. This difference is caused by a variety of small factors discussed later.

To accurately reproduce the vehicle motion in a simulation environment, the accelerations and angular velocities of the vehicle model must match the experimental data. These values are used to validate the model since they are captured directly using the IMU. The experimental data is compared against the simulation data in Figure 4.7 and Figure 4.8.

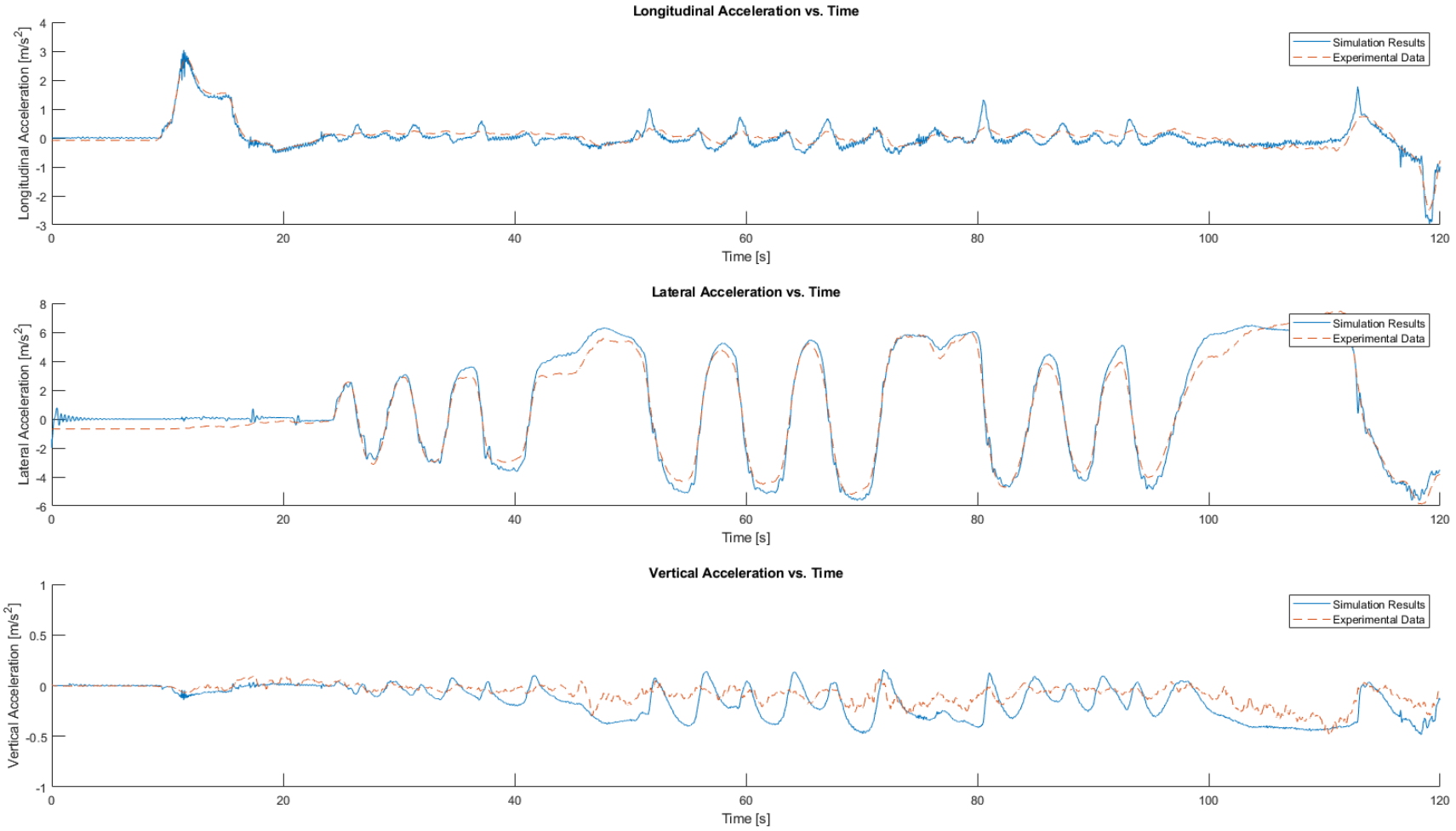

Figure 4.7: Accelerations versus time for lateral validation

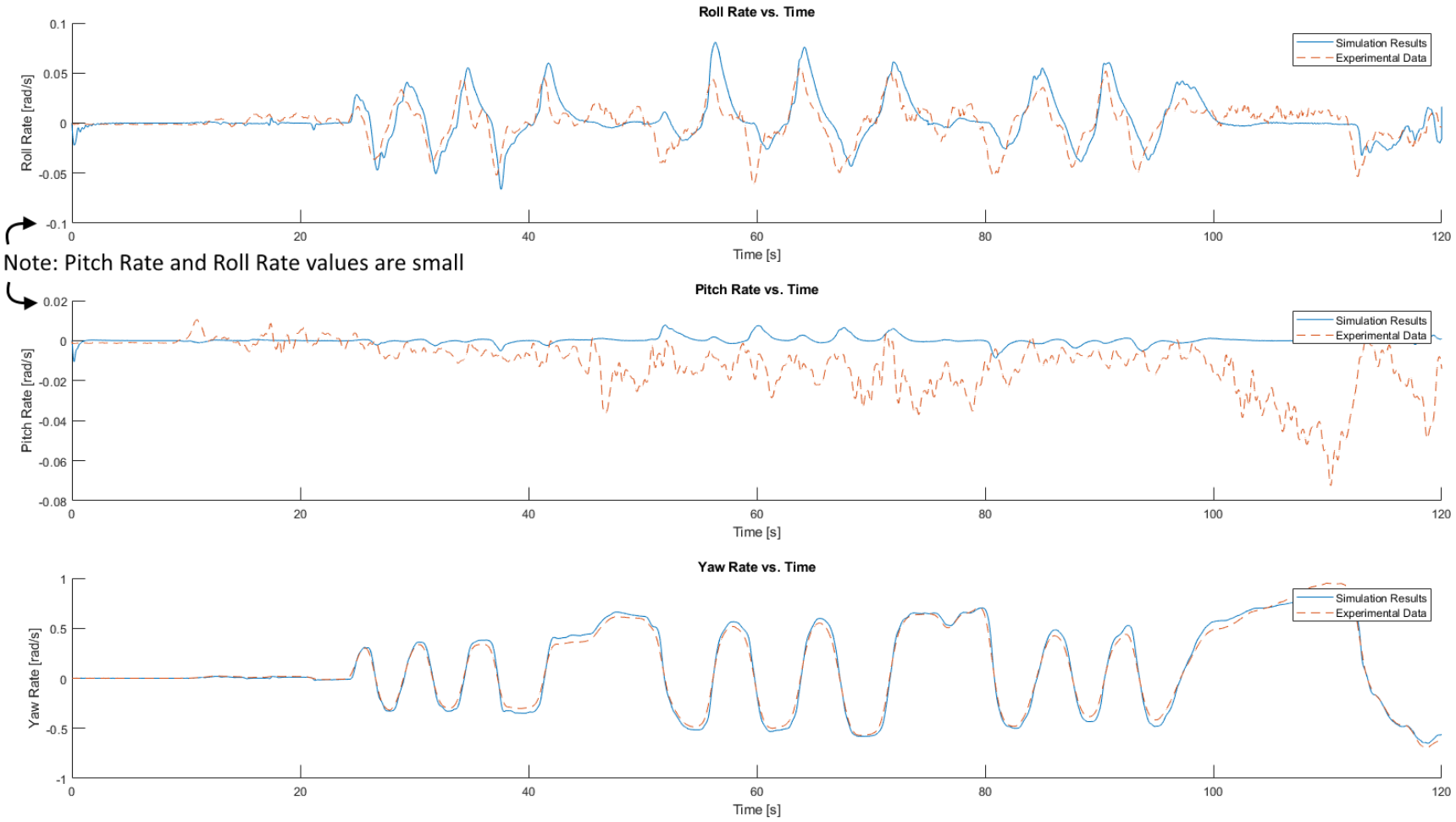

Figure 4.8: Angular velocities versus time for lateral validation

The longitudinal acceleration of the model closely matches that of the experimental data. Small differences can be seen during the cruise control section of the maneuver. Mainly, the simulation results in larger peak values than the experimental results. The primary reason for this error is the rear right wheel torque input value to the simulated mode. Due to the sensor malfunction described in Section 4.1, the rear right wheel of the vehicle was not measured during testing and could not be used as an input to the simulation model, instead the same braking torques were applied to both rear wheels. By looking at the experimental data it can be seen that this approximation is not very accurate during cornering maneuvers.

The lateral acceleration of the model is close to the experimental results from testing. The general trend of the curves are identical, and the peak values are nearly the same. The slight difference in peak values may be due to the slight inaccuracy of the semi-active control law as explained in Section 3.2.4.2. The results diverge slightly between 95s and 110s. This is likely due to cornering at a lower speed just like the results seen in the longitudinal validation results. It is also worth noting that the IMU was not placed at a known location on the vehicle. The approximate location is known but the exact coordinates are not known. Consequentially the exact experimental measurements are not accurate. There is some error introduced by estimating the location where the experimental data was collected.

For lateral validation, the roll rate and yaw rate vary the most. The pitch rate is very small as seen by the y-axis limits. The roll rate of the model lines up very closely with the experimental results, even considering the small magnitude of the values. The small errors seen here are likely due to the location of the IMU, measurement noise, or the semi-active control law of the model.

The yaw rate of the simulated model matches almost exactly with the experimental results. The only major deviation is seen between 95s and 110s for the same reasons as described earlier. Overall it is found that the simulated model follows the general curve of the experimental results, showing that the model is an accurate representation of the vehicle during lateral motion.

4.3. Combined Validation

The vehicle also needs to be validated under combined slip scenarios in order to test and validate how the vehicle will react while undergoing both longitudinal and lateral motion simultaneously. Most desired trajectories will involve the vehicle traveling under combined scenarios. For this test, the vehicle was accelerated and decelerated rapidly while also performing a variety of cornering maneuvers. It was ensured that the maneuver included acceleration, braking, and cornering events, along with various combinations of these events, in order to test the full extent of the model accuracy. The trajectory of the vehicle during this test is shown in Figure 4.9.

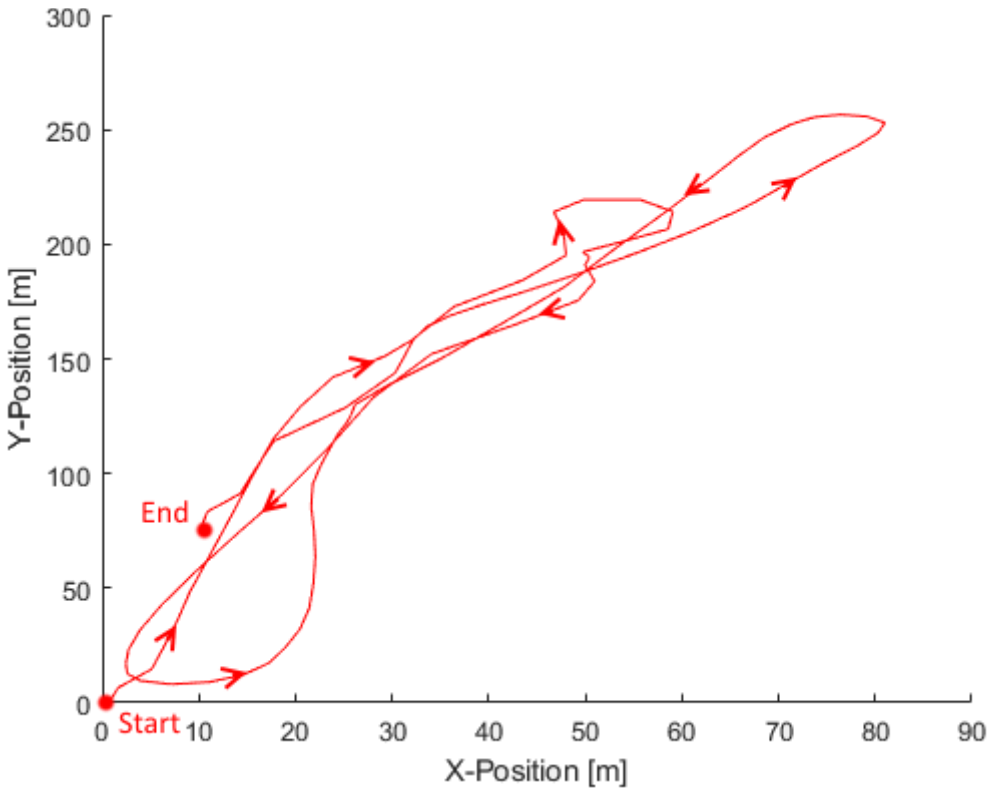

Figure 4.9: Trajectory for combined validation

The longitudinal velocity of the vehicle is shown in Figure 4.10. The longitudinal velocity of the vehicle is found by integrating the acceleration measured with the IMU.

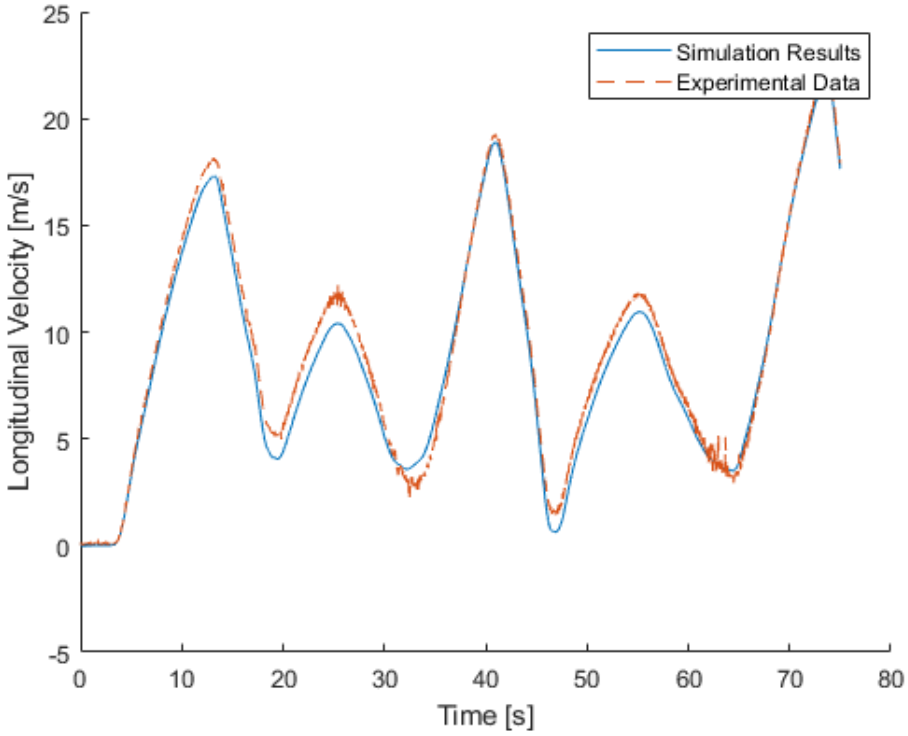

Figure 4.10: Longitudinal velocity versus time for combined validation

The velocity profile of the simulated model lines up closely with the experimental results. Most of the deviations occur after large braking regions. The experimental acceleration and angular velocity data is compared against the simulation data in Figure 4.11 and Figure 4.12.

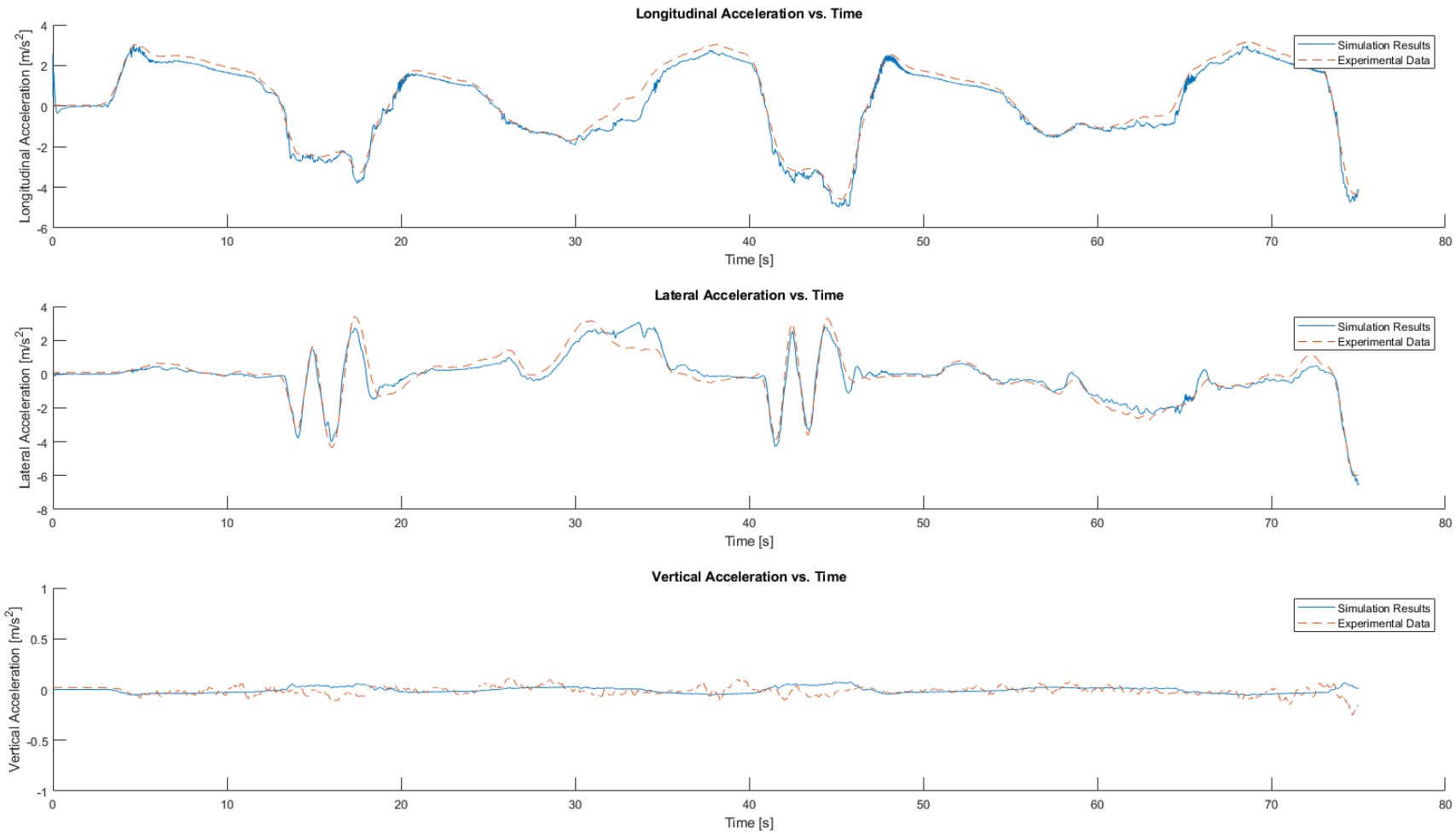

Figure 4.11: Accelerations versus time for combined validation

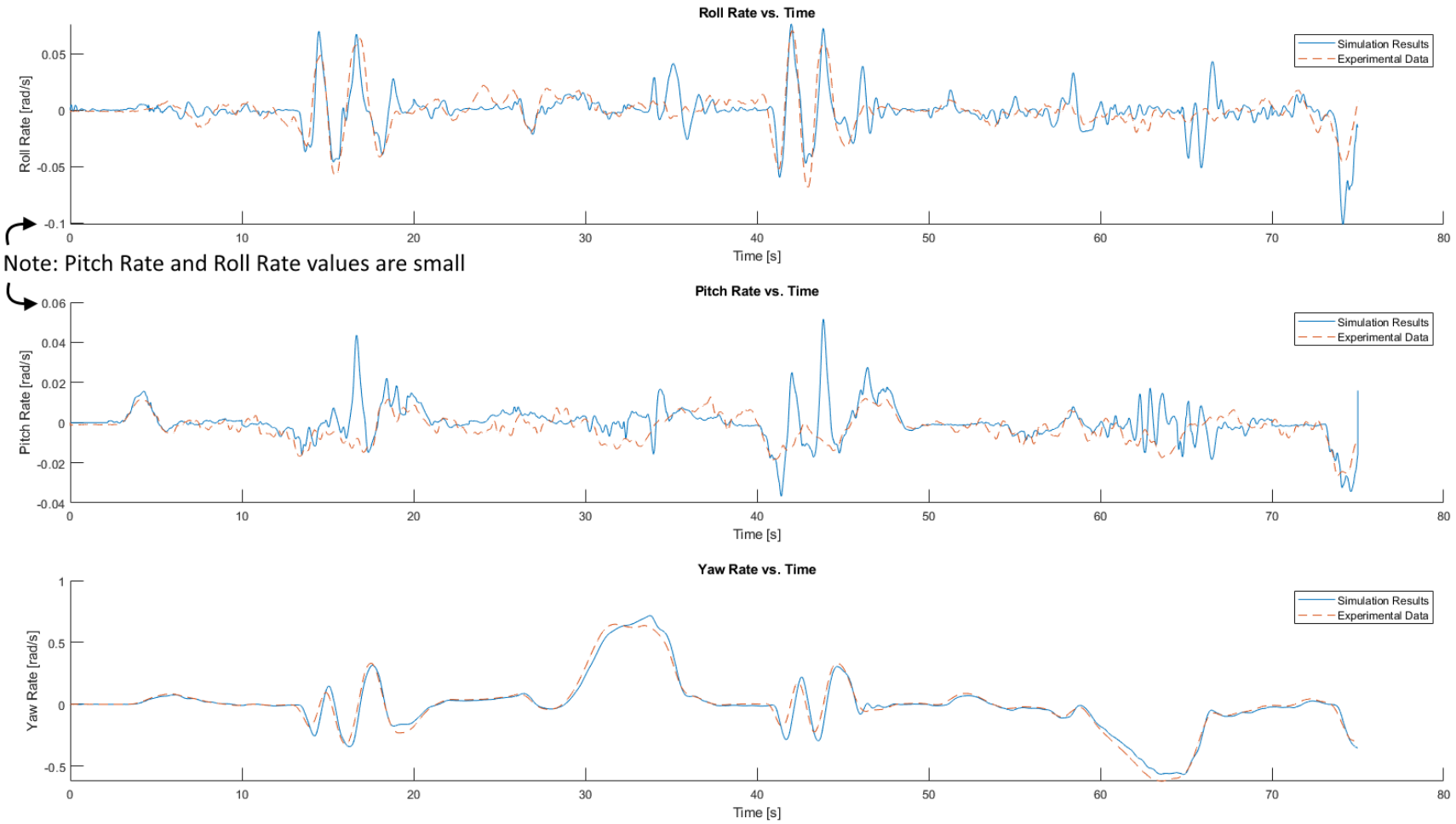

Figure 4.12: Angular velocities versus time for combined validation

The model results for the longitudinal, lateral, and vertical accelerations all match up very closely with the experimental data. The only major deviation occurs between 30s and 35s. During this time the vehicle was doing a 180^{o} turn in order to go back down the track. The only other time the vehicle fully turns around is between 60s and 65s, where another minor deviation can be seen. Beyond these two points, the simulation results line up very well with the experimental data, with the largest percent error being under 5%.

The model results for the roll, pitch, and yaw rates also all line up closely with the experimental data. The roll rate is fairly small, but the model results are practically identical to the experimental data when larger roll rates are observed, such as those seen during the quick swerving maneuvers at 15s and 42s. The pitch rate is very small but the model results follow the general trend observed in the experimental data. Lastly the yaw rate is observed. Like the lateral acceleration, the yaw rate lines up closely with the experimental data, only deviating during the large turnaround moments during the maneuver.

Overall, the combined validation shows that the full vehicle dynamic model is a reasonably accurate representation of the physical vehicle.

5. Conclusions

5.1. Summary

In this thesis, a full car model was created with MapleSim 2017.3 using experimental data from on-road testing alone. Specific road tests were designed to isolate desired parameter values in order to make parameter identification easier. These tests were designed to be repeatable, both on the same test vehicle and on other future test vehicles. Parameter identification was performed using a two-step process. First, all the necessary model parameters including the center of mass location, the inertia values of the chassis and wheels, the coefficient of drag, the suspension parameters, and the parameters for the combined slip 1989 Pacejka tire model were identified using simple models. Then a separate round of testing was completed and used to further optimize all of the identified parameters simultaneously through the high fidelity vehicle dynamic model. Lastly several different validation tests were performed in order to observe the accuracy of the model. In longitudinal, lateral, and combined testing, the simulated model results closely matched the experimental data. In conclusion, the identified model is a reasonably accurate representation of the Moose which can support controller development and virtual reality simulation for autonomous vehicle testing.

5.2. Future Work

There are many steps that can be taken to improve the full vehicle dynamic model. The primary areas for improvement are the tire models and the suspension model. While the combined slip tire models described in Section 3.2.5 are accurate, they are still based on a model from 1989; multiple improvements to the Pacejka model have been made since then. These improvements account for many of the transients, such as the rate of change of normal load, camber thrust, temperature changes, and road friction. These additional details would increase the accuracy of the tire forces; however, extensive testing would be needed to identify the 117 parameters needed for this model. The suspension model incorporated in the vehicle dynamic model includes the non-linear spring and the piecewise linear damper. In reality, the semi-active damping law is likely more complicated than a simple piecewise function. Further testing is needed to determine the actual semi-active damping law, which can then

replace the piecewise function. This would increase the accuracy of the model during sharp turns, which is currently where the model tends to deviate from the experimental data the most.

Once the full vehicle dynamic model, including the powertrain model [52] and models for all available vehicle sensors, is implemented in the simulation software (Unreal Engine 4 [55]), then full autonomous vehicle testing can be accomplished. Different scenarios can be generated in the simulation. The autonomous vehicle planning and navigation software, using data from the associated array of simulated sensors, can apply the necessary accelerator pedal position, brake pedal position, and steering wheel angle needed to follow the desired trajectory. These inputs can then feed into the full vehicle dynamic model that will dictate how the vehicle will actually travel.

Once this has been accomplished, then a specific scenario can be designed to test the accuracy of the simulated system. The specific scenario can be re-enacted in the real world, with the real vehicle, in order to compare the accuracy of the simulated outcome with the realistic outcome. Ideally the results are the same, validating future testing in the simulation environment, but potentially some modification may have to be made to increase the model fidelity.

Lastly, the full vehicle dynamic model can be incorporated as a control-oriented model used inside controllers, such as a model predictive controller (MPC). Due to the quick computation time granted by Maple's symbolic architecture, the high-fidelity model may run fast enough to be included directly inside an MPC. This would increase the accuracy of the controller significantly. It may be found that even with the quick computation time the model is still too complicated to run fast enough. In this case the model could be reduced and then implemented as a control-oriented model.

References

1. Li, K., Hang, Y., Jiang, Y., He, C., and Yue, W., "A Path Planning Method Based on Large Amount of Artificial Driving Trajectories," *SAE Technical Paper* 2018-01-1588, 2018, https://doi.org/10.4271/2018-01-1588.
2. Zhong, Y., Wang, S., Xie, S., Cao, Z., Jiang, K., and Yang, D., "3D Scene Reconstruction with Sparse LiDAR Data and Monocular Image in Single Frame," *SAE Int. J. Passeng. Cars- Electron. Electr. Syst.* 11(1):48-56, 2018, https://doi.org/10.4271/07-11-01-0005.
3. Hu, C., Wang, Y., Yu, G., Wang, Z., Lei, A., and Hu, Z., "Embedding CNN-Based Fast Obstacles Detection for Autonomous Vehicles," *SAE Technical Paper* 2018-01-1622, 2018, https://doi.org/10.4271/2018-01-1622.
4. Hu, Y. and Furukawa, T., "A High-Resolution Surface Image Capture and Mapping System for Public Roads," *SAE Int. J. Passeng. Cars – Electron. Electr. Syst.* 10(2):301-309, 2017, https://doi.org/10.4271/2017-01-0082.
5. Bacha, S., Ayad, M., Saadi, R., Aboubou, A., Bahri, M., and Becherif, M., "Modeling and control technics for autonomous electric and hybrid vehicles path following," *2017 5th International Conference on Electrical Engineering - Boumerdes (ICEE-B)*, Boumerdes, pp. 1-12, 2017, https://doi.org/10.1109/ICEE-B.2017.8191998.
6. Sabry, Y., Aly, M., Oraby, W., and El-demerdash, S., "Fuzzy Control of Autonomous Intelligent Vehicles for Collision Avoidance Using Integrated Dynamics," *SAE Int. J. Passeng. Cars - Mech. Syst.* 11(1):5-21, 2018, https://doi.org/10.4271/06-11-01-0001.
7. Zhu, B., Liu, S., and Zhao, J., "A Lane-Changing Decision-Making Method for Intelligent Vehicle Based on Acceleration Field," SAE Technical Paper 2018-01-0599, 2018, https://doi.org/10.4271/2018-01-0599.
8. Wang, Y., Feng, R., Pan, D., Liu, Z., Wu, N., Li, W., "The Trajectory Planning of the Lane Change Assist Based on the Model Predictive Control with Multi-Objective," SAE Technical Paper 2017-01-2004, 2017, https://doi.org/10.4271/2017-01-2004.
9. Hejtmanek, P., Blat'ak, O., Vancura, J., "New Approach to Measure the Vehicle Centre of Gravity Height," 2015, http://pernerscontacts.upce.cz/41_2015/Hejtmanek.pdf.
10. Price, D., "Estimation of Uncertain Vehicle Center of Gravity using Polynomial Chaos Expansions," Virginia Polytechnic Institute and State University, June 3, 2008.

11. Huang, X., Wang, J., “Center of Gravity Height Real-Time Estimation for Lightweight Vehicles using Tire Instant Effective Radius,” Control Engineering Practice, Volume 21, Issue 4, pp. 370-380, 2013, https://doi.org/10.1016/j.conengprac.2012.12.003.
12. Schedlinski, C., Link, M., “A survey of current inertia parameter identification methods”, Mechanical Systems and Signal Processing, Volume 15, Issue 1, pp. 189-211, 2001, https://doi.org/10.1006/mssp.2000.1345.
13. Heydinger, G., Durisek, N., Coovert, D., Guenther, D., and Novak, J., “The Design of a Vehicle Inertia Measurement Facility,” *SAE Transactions*, Volume 104, pp. 465–473, 1995.
14. Chrstos, J., Heydinger, G., and Guenther, D., “Error Analysis Techniques Applied to Vehicle Inertial Parameter Measurement,” ASME Transportation Systems DSC, Volume 44, 1992.
15. Heydinger, G., Bixel, R., Garrott, W., Pyne, M., Howe, J., Guenther, D., “Measured Vehicle Inertial Parameters – NHTSA’s Data Through November 1998”, Society of Automotive Engineers, 1999-01-1336, 1999
16. University of Ontario Institute of Technology: Climatic Wind Tunnel, http://ace.uoit.ca/testing-chambers/climatic-wind-tunnel.php, September 2018.
17. Thite, A., Banvidi, S., Ibicek, T., Bennett L., “Suspension parameter estimation in the frequency domain using a matrix inversion approach”, Vehicle System Dynamics, Volume 49, Issue 12, pp 1803-1822, 2011, https://doi.org/10.1080/00423114.2010.544319.
18. White, R., and Korst, H., “The determination of vehicle drag contributions from coast-down tests,” SAE Technical Paper (720099), 1972.
19. Kim, C., Ludwig, C., Park, S., and IM, C., "Improvement of Tire Development Process Through Study of Tire Test Procedure and Vehicle Correlation," *SAE Technical Paper* 2018-01-1337, 2018, https://doi.org/10.4271/2018-01-1337.
20. Wu, Y., Wang, L., and Li, F., "A Robust Path Tracking Control Method for Intelligent Vehicle," *SAE Technical Paper* 2018-01-1582, 2018, https://doi.org/10.4271/2018-01-1582.
21. Rajamani, R., “Vehicle Dynamics and Control,” Springer, 2006
22. Svendenius, J. and Wittenmark, B., "Brush tire model with increased flexibility," *2003 European Control Conference (ECC)*, Cambridge, UK, pp. 1863-1868, 2003, https://doi.org/10.23919/ECC.2003.7085237.
23. Yamashita, H., Matsutani, Y., and Sugiyama, H., “Longitudinal Tire Dynamics Model for Transient Braking Analysis: ANCF-LuGre Tire Model,” *ASME. J. Comput. Nonlinear Dynam.*, Volume 10, Issue 3, 2015, https://doi.org/10.1115/1.4028335.

24. Ding, N. and Taheri, S., “A Modified Dugoff Tire Model for Combined-slip Forces,” *Tire Science and Technology,* Volume 38, Issue 3, pp. 228-244, 2010, https://doi.org/10.2346/1.3481696.
25. Chen, L., Bian, M., Luo, Y., and Li, K., "Maximum Tire Road Friction Estimation Based on Modified Dugoff Tire Model," *2013 International Conference on Mechanical and Automation Engineering*, Jiujang, pp. 56-61, 2013, https://doi.org/10.1109/MAEE.2013.24.
26. Guarneri, P., Rocca, G., and Gobbi, M., "A Neural-Network-Based Model for the Dynamic Simulation of the Tire/Suspension System While Traversing Road Irregularities," *IEEE Transactions on Neural Networks*, Volume 19, Issue 9, pp. 1549-1563, 2008, https://doi.org/10.1109/TNN.2008.2000806.
27. Acosta, M., Kanarachos, S., and Fitzpatrick, M., "Optimized tire force estimation using extended Kalman filter and fruit fly optimization," *IECON 2017 - 43rd Annual Conference of the IEEE Industrial Electronics Society*, Beijing, pp. 4074-4079, 2017, https://doi.org/10.1109/IECON.2017.8216698.
28. Yang, X., Olatunbosun, O., and Bolarinwa, E., "Materials Testing for Finite Element Tire Model," *SAE Int. J. Mater. Manuf.*, Volume 3, Issue 1, pp. 211-220, 2010, https://doi.org/10.4271/2010-01-0418.
29. McBride, S., Sandu, C., Alatorre, A., and Victorino, A., "Estimation of Vehicle Tire-Road Contact Forces: A Comparison between Artificial Neural Network and Observed Theory Approaches," *SAE Technical Paper* 2018-01-0562, 2018, https://doi.org/10.4271/2018-01-0562.
30. Radhakrishnan, A., Rampal, H., and Ramarathnam, K., "Reduced Order Model for Tire Dynamics," *SAE Technical Paper* 2017-26-0342, 2017, https://doi.org/10.4271/2017-26-0342.
31. Pacejka, HB. “Tyre and Vehicle Dynamics. 3nd edition,” Oxford: Butterworth–Heinemann, 2012.
32. Zhang, R., "Path Following of Skid Steering Vehicles Based on Line-of-Sight Navigation," *SAE Technical Paper* 2016-01-1871, 2016, https://doi.org/10.4271/2016-01-1871.
33. Vehicle Dynamics Standards Committee, “Vehicle Dynamics Terminology*”, SAE International*, Standard J670_200801, January 2008.
34. Kageyama, I., Kuwahara, S., “A study on tire modeling for camber thrust and camber torque,” *JSAE Review, Volume 23, Issue* 3, pp. 325-331, 2002.
35. Li, S., “Camber effect study on combined tire forces,” Department of Aeronautical and Vehicle Engineering KTH Royal Institute of Technology, 2013.
36. Hackl, A., Scherndl, C., Hirschberg, W., Lex, C., “Experimental Validation of Various Temperature Modells for Semi-Physical Tyre Model Approaches”, IOP Conf. Ser.: Mater. Sci. Eng., 252 012009, 2017.
37. Pearson, M., Blanco-Hague, O., and Pawlowski, R., “TameTire: Introduction to the Model. Tire Science and Technology,” Volume 44, Issue 2, pp. 102-119, 2016.

38. Fevrier, P. and Fandard, G., “A new Thermal and Mechanical Tire Model for Handling Simulation,” 2007.
39. Durand-Gasselin, B., Dailliez, T., Mössner-Beigel, M., Knorr, S., and Rauh, J., “Assessing the thermo-mechanical TaMeTirE model in offline vehicle simulation and driving simulator tests,” *Vehicle System Dynamics*, Volume 48, pp 211-229, 2010, https://doi.org/10.1080/00423111003706730.
40. A&D Technology. https://www.aanddtech.com/, September 2018.
41. Racelogic. http://www.racelogic.co.uk/index.php/en/, September 2018.
42. Mykietyshyn, M., “Design and Validation of a Passive Suspension MapleSim Model for a Lincoln MKZ Hybrid.” Term Report, University of Waterloo, 2017.
43. ISO 4138:2012(en) Passenger cars — Steady-state circular driving behaviour — Open-loop test methods.
44. ISO 3888-1:1999(en) Passenger cars — Test track for a severe lane-change manoeuvre — Part 1: Double lane-change.
45. ISO 3888-2:2011(en) Passenger cars — Test track for a severe lane-change manoeuvre — Part 2: Obstacle avoidance.
46. ISO 7401:2012(en) Road vehicles — Lateral transient response test methods — Open-loop test methods.
47. MSC Software, “Using Adams/Tire,” Adams (MD R3) – Adams Docs, 2009.
48. Autonomous Stuff. https://autonomoustuff.com/, September 2018.
49. Batra M., McPhee J., and Azad NL., “Anti-Jerk Dynamic Modeling and Parameter Identification of an Electric Vehicle Based on Road Tests.” ASME. *J. Comput. Nonlinear Dynam*., Volume 13, Issue 10, 2018, https://doi.org/10.1115/1.4040870.
50. Buggaveeti, S., Batra, M., McPhee, J., and Azad, N., "Longitudinal Vehicle Dynamics Modeling and Parameter Estimation for Plug-in Hybrid Electric Vehicle," *SAE Int. J. Veh. Dyn., Stab., and NVH, Volume* 1, Issue 2, pp. 289-297, 2017, https://doi.org/10.4271/2017-01-1574.
51. MapleSoft. https://www.maplesoft.com/, September 2018.
52. Hosking, B., “Modelling and Model Predictive Control of Power-Split Hybrid Powertrains for Self Driving Vehicles.” Master of Applied Science, University of Waterloo, September 2018.
53. Winkler, C., Campbel, K., and Mink, C., “Center of Gravity Height: A Round-Robin Measurement Program.” Technical Report, University of Michigan Transportation Research Institute, 1991.
54. Multimatic. https://www.multimatic.com/, September 2018.

55. Hall, A., Schmitke, C., and McPhee, J., Formulation of Path- and Surface-Following Joints for Multibody Dynamics, *ASME Int. Design Eng. Tech. Conf.*, Boston, USA, DETC2015-47314, August 2015.
56. Unreal Engine 4. https://www.unrealengine.com/en-US/what-is-unreal-engine-4, September 2018.

Appendix A – MapleSim Model Picture

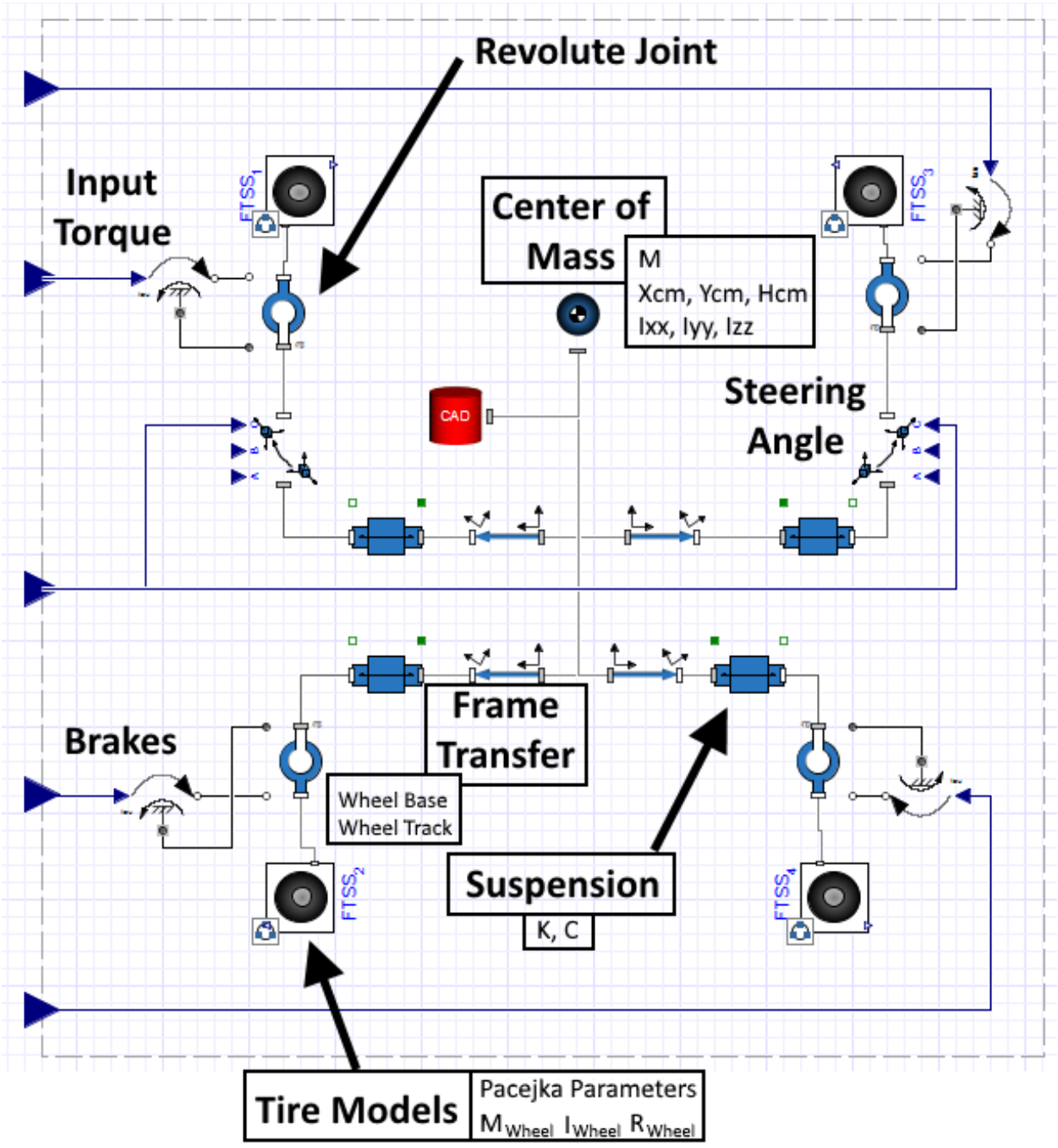

Figure A.1: Visual Representation of Full Vehicle Dynamic Model

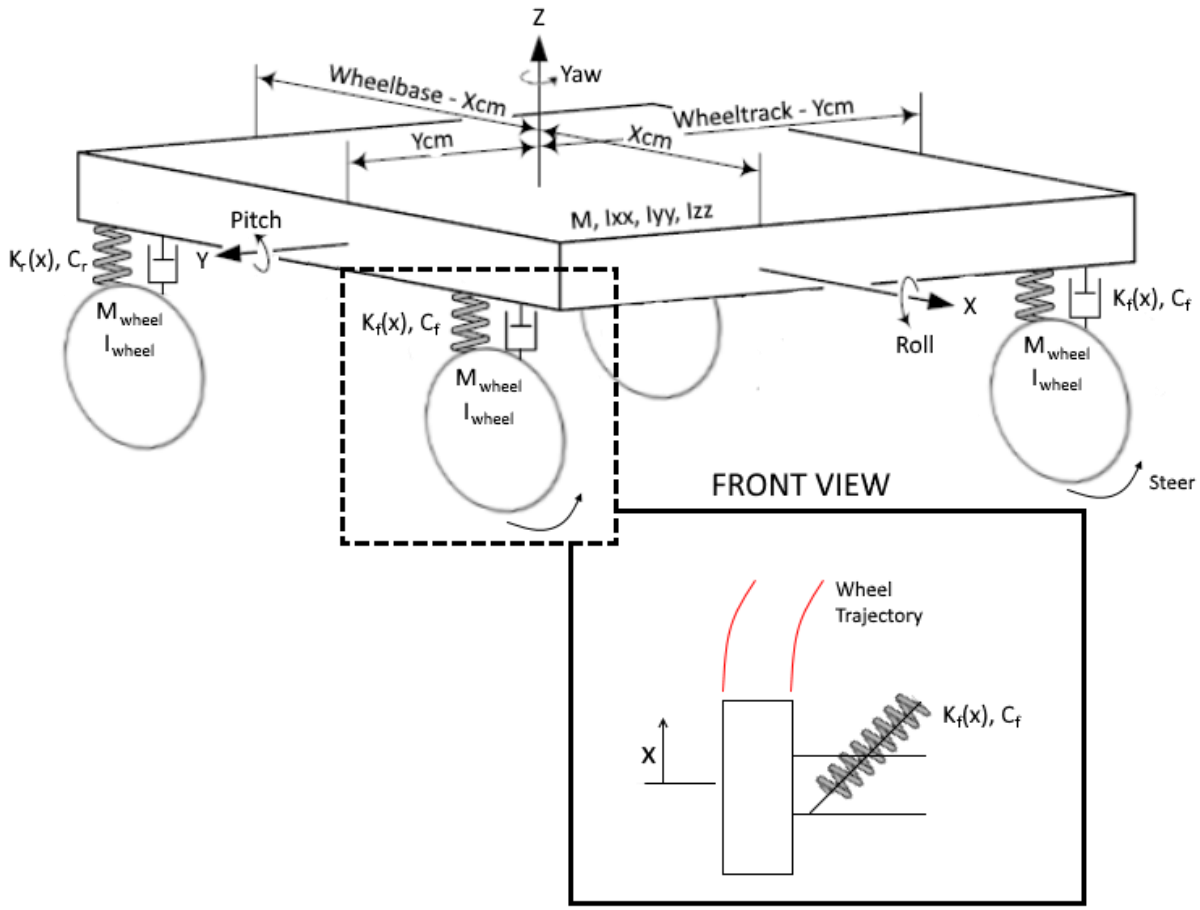

Figure A.2: Schematic of the Full Vehicle Dynamic Model

Note that the suspension trajectory is not purely vertical, it is represented by the spline outlined in Section 3.2.4.3. In summary, as the suspension compresses and extends, the camber angle changes slightly.

Appendix B – Final Parameter Values

PARAMETER	INITIAL VALUE	FINAL VALUE	DESCRIPTION
M	2202 [kg]	2202 [kg]	Mass of the vehicle with VMS attached
X_{CM}	1.39 [m]	1.35 [m]	Perpendicular distance from the center of mass to the front axle
Y_{CM}	0.865 [m]	0.833 [m]	Perpendicular distance from the center of mass to the center of the front left wheel
H_{CM}	0.566 [m]	0.542 [m]	Distance from the center of mass to the ground
WHEEL BASE	2.85 [m]	2.85 [m]	Distance from the front axle to the rear axle
FRONT TRACK	1.582 [m]	1.582 [m]	Distance from the center line of the front left wheel to the center line of the front right wheel
REAR TRACK	1.575 [m]	1.575 [m]	Distance from the center line of the rear left wheel to the center line of the rear right wheel
M_{Wheel}	14.7 [kg]	14.7 [kg]	Mass of the wheel with WFS rims
$I_{YY_{Wheel}}$	1.40 [kg m^2]	1.38 [kg m^2]	Principle moment of inertia about the spin axis of the wheel
R_{Wheel}	0.34 [m]	0.34 [m]	Unloaded radius of the tires
I_{XX}	1786 [kg m^2]	1840 [kg m^2]	Principle moment of inertia about the x-axis (Roll Inertia)
I_{YY}	3712 [kg m^2]	3700 [kg m^2]	Principle moment of inertia about the y-axis (Pitch Inertia)
I_{ZZ}	4197 [kg m^2]	4220 [kg m^2]	Principle moment of inertia about the z-axis (Yaw Inertia)
A_F	2.08 [m^2]	2.23 [m^2]	Frontal area of the vehicle
ρ	1.2 [kg m^3]	1.2 [kg m^3]	Density of air
C_D	0.743	0.59	Coefficient of drag
μ_R	0.0101	0.012	Coefficient of rolling resistance
$C_{\dot{x}>0}$	26300 [Ns/m]	26300 [Ns/m]	Damping coefficient while suspension velocity > 0
$C_{\dot{x}<0}$	68600 [Ns/m]	68600 [Ns/m]	Damping coefficient while suspension velocity < 0

Table B.1: Final parameter values for the Moose

Note that the spring stiffness is represented by Equation 3.25, where x is the compression of the spring.

Combined Slip Longitudinal Pacejka Model Parameters

Sideslip: 0	B = 7.553	C = 1.754	D = 0.862	E = 0.721
Sideslip: 2	B = 7.551	C = 1.75	D = 0.831	E = 0.68
Sideslip: 5	B = 6.012	C = 1.613	D = 0.672	E = 0.638
Sideslip: 10	B = 5.42	C = 1.827	D = 0.56	E = 0.711
Sideslip: 15	B = 2.98	C = 1.711	D = 0.512	E = 0.719
Sideslip: 20	B = 2.48	C = 1.648	D = 0.47	E = 0.72
Sideslip: 25	B = 2.473	C = 1.642	D = 0.454	E = 0.72

Table B.2: Combined slip longitudinal Pacejka model parameters

Combined Slip Lateral Pacejka Model Parameters

Slip: 0	B = 9.488	C = 1.865	D = 1.02	E = 1.181
Slip: 0.1	B = 9.02	C = 1.67	D = 0.98	E = 0.952
Slip: 0.2	B = 8.764	C = 1.521	D = 0.93	E = 0.912
Slip: 0.3	B = 6.128	C = 1.381	D = 0.854	E = 0.256
Slip: 0.4	B = 5.213	C = 1.32	D = 0.836	E = 0.124

Table B.3: Combined slip lateral Pacejka model parameters